University of Glasgow | School of Engineering

Novel Dual Wavelength and Multi-wavelength DFB/DBR Lasers for MMW/THz Generation

Yizhe Fan

2025

A thesis submitted for the degree of

Doctor of Philosophy (Ph.D.)

Electronics and Nanoscale Engineering,

James watt school of engineering

Declaration of Authorship

I, **Yizhe Fan**, declare that this thesis titled **"Novel Dual Wavelength and Multi-wavelength DFB Lasers for MMW/THz Generation"** and the contributions presented in it are my own. I confirm that:

This work was done wholly or mainly while in candidature for a research degree at this University.

Where any part of this thesis has previously been submitted for a degree or any other qualification at this University or any other institution, this has been clearly stated.

Where I have consulted the published work of others, this is always clearly attributed.

Where I have quoted from the work of others, the source is always given. With the exception of such quotations, this thesis is entirely my own work. I have acknowledged all main sources of help.

Where the thesis is based on work done by myself jointly with others, I have made clear exactly what was done by others and what I have contributed myself.

Signed: Yizhe Fan

Date: March 27, 2025

Contents

List of Figures

List of Tables

Acronyms

Acronyms	Description
2PS-SBG	Two-phase-shift SBG
4PS-SBG	Four phase-shifted SBG
4PS-SMG	four phase-shifted sampled Moiré grating
AC	Autocorrelation
Ar	Argon
AR	Anti-reflection
ASE	Amplified spontaneous emission
CCM	Compound-cavity mode-locking
CCP	Capacitive coupled plasma
CH_3COCH_3	Acetone
CH_4	Methane
CHF_3	Fluoroform
Cl_2	Chlorine
CMOS	Complementary metal–oxide–semiconductor
CMP	Chemical mechanical polishing
CMT	Coupled mode theory
CPM	Colliding pulse mode-locking
C-SBG	conventional SBG
C-SMG	Conventional sampled Moiré grating
Cu	Copper
CW	Continuous wave
DBR	Distributed Bragg reflector
DFB	Distributed feedback
DFG	Difference frequency generation
DWL	Dual-wavelength laser

EAM	Electro-absorption modulator
EBL	Electron beam lithography
EDFA	Erbium-doped fiber amplifier
EPS	Equivalent π-phase shift
ESA	Electrical spectrum analyzer
FBG	Fiber Bragg grating
FDE	Finite difference eigenmode
FFT	Fast Fourier Transform
FM	Frequency modulation
FP	Fabry-Pérot
FWHM	Full width at half maximum
FWM	Four-wave mixing
GPIB	General-purpose interface bus
GRINSCH	Graded-index separate confinement heterostructure
H_2	Hydrogen
HML	Harmonic mode-locking
HSQ	Hydrogen silsesquioxane
ICL	Interband cascade lasers
ICP	Inductively coupled plasma
ICR	intracavity reflector
In	Indium
IoT	Internet of Things
IPA	Isopropyl alcohol
JWNC	James Watt Nanofabrication Center
LiDAR	Light detection and ranging
MG	Moiré grating
MI	Michelson interferometer
MIBK	Methyl isobutyl ketone

MIBK	Methyl isobutyl ketone
MIMO	Multiple-input multiple-output
MIR	Mid-infrared
ML-DBR	Mode-locked DBR
ML-DFB	Mode-locked DFB
MLLD	Mode-locked laser diode
MMW	Millimeter-wave
MOCVD	Metal organic chemical vapor deposition
MOVPE	Metalorganic vapor phase epitaxy
MPSG	Multiple phase-shift grating
MQW	Multiple quantum well
NMR	Nuclear magnetic resonance
OPLL	Optical phase-locked loop
PCA	Photoconductive antenna
PD	Photodetector
PDM	Power difference between two modes
PEC	Proximity effect correction
PECVD	Plasma-enhanced chemical vapour deposition
PMMA	Polymethyl methacrylate
PPS-SGDBR	π-phase shifted SGDBR
QB	Quantum barrier
QCL	Quantum cascade laser
QW	Quantum well
RBW	Resolution bandwidth
RF	Radiofrequency
RIE	Reactive ion etching
RO	Reverse osmosis
RTA	Rapid thermal annealing

SA	Saturable absorber
SBG	Sampled Bragg grating
SGDBR	Sampled grating distributed Bragg reflector
SH	Second harmonic
SHG	Second harmonic generation
SiO_2	Silicon dioxide
SLM	Single longitudinal mode
SMG	Sampled Moiré grating
SMSR	Side mode suppression ratio
SOA	Semiconductor optical amplifier
SPM	Self-phase modulation
SSG	Super-structure grating
TBP	Time-bandwidth product
Tbps	Terabit-per-second
TE	Transverse electric
TEC	Thermoelectric cooler
THz	Terahertz
THz-TDS	Terahertz time-domain spectroscopy
TM	Transverse magnetic
TMAH	Tetramethylammonium hydroxide
TMM	Transfer matrix method
TW-PD	Traveling-wave photodiode
UBG	Uniform Bragg grating
UTC-PD	Uni-traveling carrier photodiode

Abstracts

Millimeter-wave (MMW) and terahertz (THz) and sources have gained significant attention due to their wide-ranging applications in high-speed wireless communications, high-resolution imaging, and advanced sensing technologies. In this thesis, I propose and experimentally demonstrate a series of innovative DFB and DBR semiconductor lasers based on multiple quantum well (MQW) structures operating at 1550 nm for MMW/THz generation.

Three novel findings are reported in the work. Firstly, I demonstrate a dual-wavelength DFB laser array employing a four-phase-shifted sampled Bragg grating (4PS-SBG), which enhances coupling efficiency by approximately 2.83 times compared to conventional designs. The device exhibits stable dual-mode operation with frequency spacings ranging from 320 GHz to 1 THz, achieving an output power of 23.6 mW when integrated with semiconductor optical amplifiers (SOAs). Photomixing in a photoconductive antenna (PCA) result in THz signal generation with a measured power of 12.8 μW. Secondly, I introduce a dual-wavelength DFB laser using a four-phase-shifted sampled Moiré grating (4PS-SMG) with distinct sampling periods on each ridge waveguide side, equivalently introducing two π-phase shifts within the cavity. The device exhibits high stability across a broad injection current range, maintaining a power difference below 2 dB between primary modes. This laser generates a high-purity RF signal at 39.4 GHz with a linewidth of approximately 5.0 MHz. Lastly, I propose mode-locked DBR and DFB lasers employing multiple phase-shift gratings (MPSGs) for high-frequency THz generation. The mode-locked DBR laser achieves stable operation at 150 GHz, 400 GHz, 800 GHz, and 1.2 THz, validated through second harmonic generation measurements. A 200 GHz mode-locked DFB laser, amplified via an erbium-doped fiber amplifier (EDFA) and injected into a PCA, delivers a THz output power of 19.6 μW. Design, fabrication and characterization of these semiconductor lasers are introduced in detail in this thesis.

Acknowledgements

At the end of my PhD journey, I would like to express my heartfelt gratitude to all those who have accompanied and supported me along the way. This journey has been filled with moments—both challenging and joyful—that I will always cherish. These years have added a vivid and unforgettable chapter to my life.

First and foremost, I would like to express my sincere gratitude to my first supervisor, Dr. Lianping Hou, for giving me the opportunity to pursue my PhD at the University of Glasgow. Throughout my academic journey, he has provided invaluable guidance in the design, fabrication, and characterization of laser devices as well as writing scientific papers. His patience, encouragement, and expertise have been instrumental in shaping my development as a researcher. I would also like to thank my second supervisor, Prof. John Marsh, for his insightful academic advice and continuous support throughout my PhD. His suggestions and feedback have helped me refine my work and broaden my perspective.

I sincerely appreciate the support and contributions from all the staff at the James Watt Nanofabrication Centre. Without their dedication to maintaining and operating the cleanroom facilities, the completion of my research would not have been possible. I would like to thank Rachel Love and Archie Mclver for their patient assistance during the optimization of the ICP dry etching process.

Among the colleagues I had the pleasure of working with, I would like to express my sincere thanks to Dr. Shengwei Ye for his guidance and support during the fabrication processes. I am especially grateful to Dr. Bocheng Yuan for his valuable insights into device design and characterization, as well as for his constant patience in discussing technical details with me. Their help guided me step by step into the field, allowing me to gain a comprehensive understanding of laser design, fabrication, and testing. I would also like to thank Simeng Zhu for the academic discussions we shared. His input helped me identify many subtle yet important issues worth further reflection.

Acknowledgements

During my time studying abroad, the spiritual support from friends has been an essential part of my journey. I would like to thank Bocheng Yuan, Simeng Zhu, Yiming Sun, and all the friends around me for their companionship. Your presence made my days in Glasgow truly heartwarming. I sincerely wish each of you a bright and fulfilling future.

Finally, I would like to express my deepest gratitude to my parents and family. Throughout my academic journey, they have provided unwavering financial and emotional support. Their constant encouragement has been a source of strength and a driving force that kept me moving forward, even during the most difficult times. I hope that my efforts will live up to their expectations and make them proud.

List of Publications

Journal Papers

1. S. Zhu, B. Yuan, **Y. Fan**, M. Al-Rubaiee, X. Sun, Z. Li, A. S. Hezarfen, A. E. Kelly, J. H. Marsh, and L. Hou, "A reconfigurable multi-channel on-chip photonic filter for programmable optical frequency division", *Nanophotonics* (Early Online Publication).

2. **Y. Fan**, M. Al-Rubaiee, S. Zhu, B. Yuan, X. Sun, Y. Sun, A. E. Kelly, J. H. Marsh, and L. Hou, "Mode-locked DBR and DFB lasers with multiple phase-shifted gratings for THz generation", *J. Lightwave Technol.*, (Early Online Publication).

3. M. Al-Rubaiee, X. Sun, B. Yuan, **Y. Fan**, S. Zhu, Y. Sun, J. H. Marsh, S. J. Sweeney, and L. Hou "Simultaneous multi-wavelength mode-locked DFB laser based on waveguide Bragg grating microcavities", *Opt. Express*, vol. 33, no. 11, pp. 22222-22234, June, 2025.

4. S. Zhu, B. Yuan, M. Al-Rubaiee, Y. Sun, **Y. Fan**, A. S. Hezarfen, S. J. Sweeney, J. H. Marsh, and L. Hou, "Widely tunable photonic filter based on equivalent chirped four-phase-shifted sampled Bragg gratings", *ACS Photonics*, vol. 12, no. 2, pp. 899-907, Feb. 2025.

5. X. Sun, Z. Li, **Y. Fan**, M. Jamal Al-Rubaiee, J. H. Marsh, A. E. Kelly, S. J. Sweeney, and L. Hou, "Multi-wavelength DFB laser based on a sidewall third-order four phase-shifted sampled Bragg grating with uniform wavelength spacing", *Opt. Lett.*, vol. 50, no. 3, p. 714, Feb. 2025.

6. Y. Sun, S. Zhu, B. Yuan, **Y. Fan**, M. Al-Rubaiee, X. Sun, J. H. Marsh, S. J. Sweeney, and L. Hou, "Continuous phase modulation technology based on grating period interval for high grating coupling coefficient and precise wavelength control", *Opt. Lett.*, vol. 50, no. 3, p. 750, Feb. 2025.

7. S. Zhu, B. Yuan, W. Cheng, **Y. Fan**, Y. Sun, M. Al-Rubaiee, J. Akbar, J. H. Marsh, and L. Hou, "Dual-Band Photonic Filters with Wide Tunable Range Using Chirped Sampled Gratings", *IEEE Photon. Technol. Lett.*, vol. 37, no. 3, pp. 169–172, Feb. 2025.

8. S. Zhu, B. Yuan, M. Al-Rubaiee, Y. Sun, **Y. Fan**, A. S. Hezarfen, S. J. Sweeney, J. H. Marsh, and L. Hou, "Widely Tunable Photonic Filter Based on Equivalent Chirped Four-Phase-Shifted Sampled Bragg Gratings", *ACS Photonics*, vol. 12, no. 2, pp. 899–907, Feb. 2025.

9. Y. Sun, B. Yuan, X. Sun, S. Zhu, **Y. Fan**, M. Al-Rubaiee, J. H. Marsh, S. J. Sweeney, and L. Hou, "Narrow linewidth distributed feedback lasers utilizing distributed phase shift", *Opt. Lett.*, vol. 50, no. 2, p. 471, Jan. 2025.

10. M. Al-Rubaiee, B. Yuan, **Y. Fan**, S. Zhu, J. Marsh, and L. Hou, "Ultrastable 10 GHz Mode-Locked Laser on Semi-Insulating Substrate Through RF Injection Locking", *IEEE Photon. Technol. Lett.*, vol. 36, no. 19, pp. 1189–1192, Oct. 2024.

11. L. Hou, B. Yuan, **Y. Fan**, X. Sun, Y. Sun, S. Zhu, S. J. Sweeney, J. H. Marsh, "Monolithic Dual Wavelength DFB Lasers Based on Sidewall Gratings for THz/MMW Signal Generation," *IEEE J. Select. Topics Quantum Electron.*, pp. 1–14, 2024.

12. **Y. Fan**, B. Yuan, M. Al-Rubaiee, Y. Sun, S. Zhu, J. H. Marsh, L. Hou,'Dual-Wavelength DFB Laser Array Based on Four Phase-Shifted Sampled Bragg Grating for THz Generation', *Opt. Lett.*, vol. 49, no. 12, pp. 3472-3475, 2024.

13. **Y. Fan**, B. Yuan, M. Al-Rubaiee, Y. Sun, S. Zhu, J. Akbar, J. H. Marsh, L.Hou, 'Millimeter-Wave Generation Based on Four Phase-Shifted Sampled Moiré Grating Dual-Wavelength DFB Laser', *IEEE Photon. Technol. Lett.*, vol. 36, no. 4, pp. 282–285, Feb. 2024.

14. B. Yuan, **Y. Fan**, S. Ye, Y. Zhang, Y. Sun, X. Sun, W. Cheng, S. Liang, Y. Huang, R. Zhang, J. Wang, J. H. Marsh, L. Hou, 'Dual-wavelength DFB Laser Array Based on Sidewall Grating and Lateral Modulation of the Grating Coupling Coefficient', *J. Lightwave Technol.*, pp. 1–11, 2023.

15. Y. Sun, B. Yuan, X. sun, S. Liang, Y. Huang, R. Zhang, S. Ye, **Y. Fan**, W. Cheng, J. H. Marsh, L. Hou, "DFB laser array based on four phase-shifted sampled Bragg grating with precise wavelength control," *Opt. Lett.*, vol.47, no.23 pp.6237-6240, 2022.

Conference Papers

1. M. Al-Rubaiee, X. Sun, **Y. Fan**, S. Zhu, Y. Sun, A. Seckin, J. H. Marsh, S. J. Sweeney, and L. Hou, "Monolithic Multi-Wavelength Mode-Locked DFB Laser Based on Waveguide Bragg Grating Microcavities". In: *51st European Conference on Optical Communication (ECOC 2025)*, 2025. (Accepted for Publication)

2. S. Zhu, M. Al Rubaiee, **Y. Fan**, X. Sun, Y. Sun, J. H. Marsh, and L. Hou, "A Programmable and Reconfigurable On-Chip Photonic Filter for Next-Generation Multi-Channel DWDM". In: *51st European Conference on Optical Communication (ECOC 2025)*, 2025. (Accepted for Publication)

3. S. Zhu, T. Wu, **Y. Fan**, X. Sun, B. Liu, J. H. Marsh, and L. Hou "Integrated Multi-Band Photonic Filter Based on MRR–SSG for Tunable Frequency Hopping". In: *51st European Conference on Optical Communication (ECOC 2025)*, 2025. (Accepted for Publication)

4. Y. Sun, M. Al-Rubaiee, B. Yuan, A. S. Hezarfen, X. Sun, S. Zhu, **Y. Fan**, J. H. Marsh, and L. Hou, "DWDM Source Utilizing a 4PS-SBG DFB Laser Array with Monolithic ATG Technology," In *2025 CLEO*, 2025. (Accepted for Publication)

5. M. Al-Rubaiee, **Y. Fan**, B. Yuan, S. Zhu, Y. Sun, A. S. Hezarfen, J. H. Marsh, S. J. Sweeney, and L. Hou, "Four-Wavelength Mode-Locked DFB Laser with Four Phase-Shifted Chirped Sampled Bragg Grating," In: *2025 CLEO*, 2025. (Accepted for Publication)

6. Z. Wang, **Y. Fan**, X. Sun, B. Yuan, Y. Sun, M. Al-Rubaiee, A. S. Hezarfen, S. Zhu, J. H. Marsh, A. Kelly, and L. Hou, "Linewidth-Reduced Optical Injection-Locked Laser Utilizing Four-Phase-Shifted Sampled Bragg Gratings," In *2025 CLEO*, 2025. (Accepted for Publication)

7. S. Zhu, M. Al-Rubaiee, B. Yuan, **Y. Fan**, Y. Sun, J. H. Marsh, and L. Hou, "Broadband Tunable Photonic Filter Utilizing Equivalent Chirped Sampled Bragg Gratings for Optical Frequency Division," In *2025 OFC*, 2025. (Accepted for Publication)

8. S. Zhu, M. Al-Rubaiee, B. Yuan, **Y. Fan**, Y. Sun, J. H. Marsh, and L. Hou, "Dual-Band Microwave Photonic Filter Utilizing Equivalent Chirped Four-Phase-Shifted Sampled Bragg Grating for 52.1 GHz – 439.5 GHz Range," In: *SPIE Photonics West*, 2025. (Accepted for Publication)

9. S. Zhu, B. Yuan, **Y. Fan**, Y. Sun, J. H. Marsh, and L. Hou. "Tunable Dual-band Microwave Photonic Filters Covering 37.2 GHz to 186.1 GHz Utilizing Chirped Sampled Gratings," In *2024 ECOC*, 2024.

10. S. Zhu, W. Cheng, B. Yuan, **Y. Fan**, Y. Sun, A. S. Hezarfen, J. H. Marsh, and L. Hou. "High Sensitivity Biochemical Sensors Based on a Mach-Zehnder Interferometer with a Slot Bus Waveguide and Double Slot Hybrid Plasmonic Waveguide, " In *2024 ECOC*, 2024.

11. **Y. Fan**, B. Yuan, M.Al-Rubaiee, J. H. Marsh, and L. Hou, 'Dual-wavelength DFB Laser Based on Four Phase-shifted Sampled Moiré Grating for MMW Generation', in *2024 CLEO*, 2024.

12. M. Al-Rubaiee, S. Ye, B. Yuan, **Y. Fan**, J. H. Marsh, L. Hou, '10 GHz Low Divergence

Angle Mode-Locked Lasers with Ultralow Timing Jitter through Injection-Locking', in *2024 CLEO*, 2024.

13. **Y. Fan**, Y. Zhang, Y. Sun, B. Yuan, J. H. Marsh, L. Hou, "Monolithic Optical Injection Locking DFB Lasers Based on Four Phase-Shifts Sampling Sections", in *2023 CLEO/Europe-EQEC*, 2023.

14. B. Yuan, **Y. Fan**, S. Zhu, Y. Zhang, J. H. Marsh, L. Hou, "Dual-wavelength DFB Laser Based on Four Phase-shifts Sections and Equivalent Chirp Technology for Millimeter-wave Generation" in *2023 CLEO/Europe-EQEC*, 2023.

15. **Y. Fan**, B. Yuan, S. Ye, Y. Sun, J. Marsh, L. Hou, "Dual Wavelength DFB Laser Array Based on Four Phase Shifted Sampled Bragg Gratings for THz Generation," in *2023 CLEO,* 2023.

16. **Y. Fan**, B. Yuan, S. Ye, J. H. Marsh, Y. Huang, L. Hou, "Dual-Wavelength DFB Laser with 1.28 THz Frequency Spacing Based on Four Phase Shifted Sampling Gratings," in *2022 IEEE Photonics Conference (IPC)*, 2022.

17. Y. Sun, X. Sun, B. Yuan, **Y. Fan**, J. H. Marsh, L. Hou, "DFB Laser Array Based on Four Phase-Shifted Sampled Bragg Gratings," in *2022 IEEE Photonics Conference (IPC)*, 2022.

Chapter 1 Introduction

1.1 MMW/THz Opportunities in Future Technologies

The MMW and THz frequency bands, spanning from 30 GHz to 3 THz, present groundbreaking opportunities for next-generation wireless communication, sensing, and imaging systems. These frequency ranges, characterized by their vast unutilized bandwidth and distinct propagation properties, serve as key enablers for applications requiring ultra-high data rates [1], [2], [3], precise localization [4], [5], and advanced material characterization [6], [7].

1.1.1 Millimeter Waves in Communications

With the explosive growth in mobile data traffic and the proliferation of connected devices, future wireless networks are expected to face unprecedented capacity and performance demands [1], [8]. Meeting the stringent requirements of 5G and 6G systems has thus motivated the exploration of new spectrum resources and advanced device architectures. To address these challenges, there has been growing interest in leveraging the MMW spectrum, spanning 30 to 300 GHz, where significantly broader bandwidths are available compared to today's cellular allocations [9], [10], [11]. This high-frequency spectrum offers up to 200 times more bandwidth than the heavily congested sub-3 GHz radiofrequency (RF) bands.

Additionally, the small wavelengths of MMW signals, combined with advances in low-power complementary metal–oxide–semiconductor (CMOS) RF technologies, enable the integration of compact antenna arrays (typically >32 elements) into small form factors. These antenna arrays can provide high-gain, electronically steerable beams, and may be implemented in base stations, mobile devices, or even on-chip [12], [13], [14]. The integration of multi-channel phased-array beamforming chips using low-cost CMOS technology has paved the way for the widespread adoption of MMW communication

systems. Beyond 5G, the next-generation WiFi is expanding into the Ka-band (26.5–40 GHz), V-band (50–60 GHz), Q-band (33–50 GHz), and E-band (60–90 GHz), which collectively offer wide spectral bandwidths for multi-gigabit communication.

MMW radar technology also plays a pivotal role in advanced driver assistance systems and autonomous driving [15], [16], [17]. Automotive MMW radar typically operates in the 76–81 GHz band, employing frequency-modulated continuous wave technology, enabling detection distances of up to 250 meters. Compared to light detection and ranging (LiDAR), MMW radar provides superior all-weather performance and lower sensitivity to adverse environmental conditions such as fog or rain. While it offers coarser spatial resolution, it is essential for adaptive cruise control and complements LiDAR in autonomous driving perception systems.

1.1.2 THz Waves and Applications

THz waves generally refer to electromagnetic waves with frequencies ranging from 100 GHz to 10 THz, corresponding to wavelengths from 30 μm to 3 mm. Historically, THz waves have been referred to by different names in electronics and optics. In the field of electronics, they are categorized within the MMW and submillimeter-wave regions, while in optics, they are commonly known as the far-infrared spectrum [18], [19]. This classification highlights that the THz band lies in the transition region between millimeter waves and infrared waves, serving as a bridge between macroscopic classical theories and microscopic quantum theories, as illustrated in Fig. 1.1. For a long time, although both infrared technology and microwave/MMW technology—on either side of the THz spectrum—have been relatively mature, the development of THz sources and detection technologies has been limited. As a result, the understanding and practical utilization of THz waves remain incomplete. Due to these technological gaps, the THz frequency range is often referred to as the "THz gap."

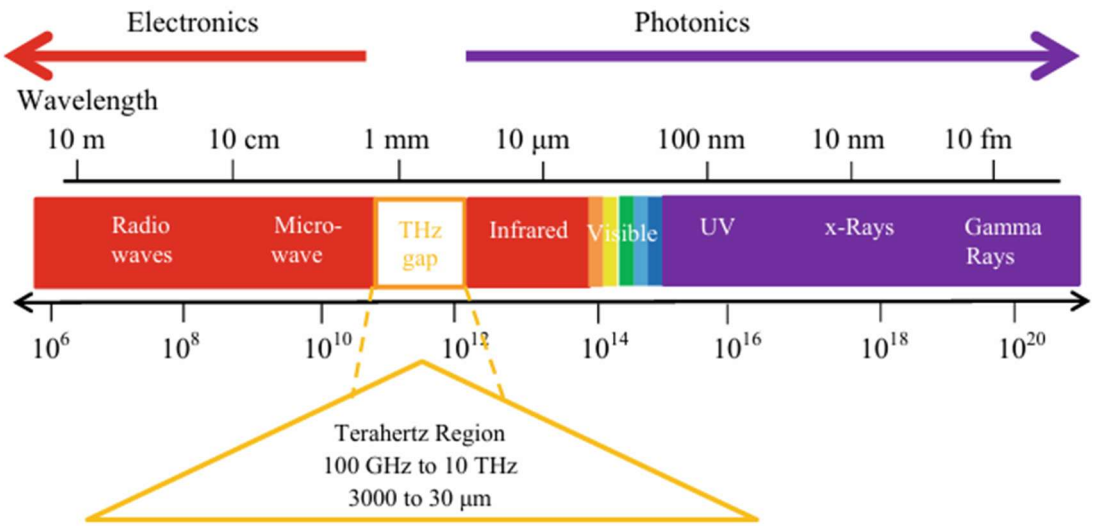

Fig. 1.1 Electromagnetic spectrum showing the THz gap [20].

THz radiation has attracted significant attention due to its unique interaction with various materials, enabling a broad range of applications spanning spectroscopy, security screening, imaging, astronomy, and high-speed communications [21], [22], [23], [24]. Below, I summarize the key application areas of THz technology.

1. **Spectroscopic Sensing**

   Many biochemical molecules exhibit vibrational and rotational resonances within the THz frequency range, resulting in strong absorption peaks. This spectral characteristic allows THz waves to be effectively utilized for distinguishing biomolecules and analyzing conformational changes. Furthermore, THz waves are highly absorbed by water, making them well-suited for probing water content in biological systems [25], [26]. This feature enables THz spectroscopy to complement existing medical diagnostic techniques, such as X-ray imaging and nuclear magnetic resonance (NMR), in non-invasive medical diagnostics.

2. **Security Screening and Imaging**

   THz waves possess the ability to penetrate non-polar materials, such as plastics, paper, and ceramics, which are typically opaque to visible and mid-infrared (MIR)

light. Certain molecules exhibit strong coupling between their vibrational or rotational energy states and THz radiation, leading to unique spectral fingerprints that facilitate material identification. Compared to microwave imaging, THz waves offer higher spatial resolution due to their shorter wavelengths. Moreover, unlike high-energy X-rays, THz radiation is non-ionizing and poses no harm to biological tissues, making it ideal for safe and effective security screening applications. These properties enable THz imaging to differentiate objects based on their shape and composition, facilitating applications such as pharmaceutical quality control, concealed object detection, and chemical substance identification [27], [28], [29], [30].

3. **Astronomy and Space Exploration**

   THz radiation is well-suited for passive emission spectroscopy due to the low energy required for optical transitions in this spectral range. A significant portion of cold matter in space exists at temperatures between 10 K and 100 K, with their radiation predominantly concentrated in the THz spectrum. Notably, approximately 50% of Milky Way's radiation is within the THz frequency range. Consequently, THz astronomy plays a crucial role in studying the evolution of stars, analyzing the chemical composition of interstellar clouds, and investigating the physical conditions of cosmic dust and gas [31].

4. **High-Speed Wireless Communications**

   The increasing demand for ultra-high-speed data transmission, particularly in the terabit-per-second (Tbps) regime, has driven the exploration of THz frequencies for next-generation communication systems. The scarcity of available bandwidth in lower-frequency ranges limits the feasibility of achieving Tbps links, while frequencies above 10 THz suffer from significant atmospheric attenuation and high scattering losses, making them impractical for long-range transmission. THz waves provide an optimal balance by offering a broader bandwidth ranging from tens of

GHz to several THz, depending on the transmission distance [32], [33], [34]. Fig. 1.2 presents the atmospheric attenuation calculated for rain rates of 25 mm/h and 5 mm/h, with the red lines indicating the baseline attenuation caused by rainfall [3]. It is evident that as the frequency increases, attenuation rises sharply, significantly limiting the transmission distance in the THz frequency range. This poses a major challenge for the practical deployment of THz wireless communication systems. However, certain transmission windows within the THz spectrum exhibit relatively lower attenuation and may be leveraged to mitigate this limitation.

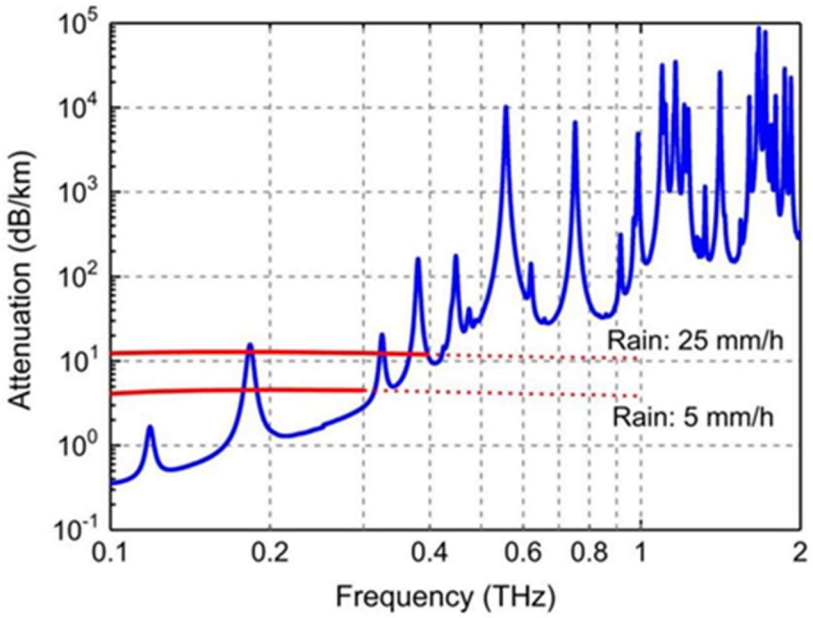

Fig. 1.2 Atmospheric attenuation calculated due to rain rates of 25 and 5 mm/h, with water content of 7.5 g/m^3 and atmospheric temperature of 20 °C [3].

In this study, to validate the broadband applicability of the proposed sampled grating structure in this paper, several representative frequencies were selected in this paper. These frequencies span the MMW/THz boundary and were chosen to demonstrate the ability of the design to target discrete THz channels across a wide spectral range. Importantly, several of these frequencies (notably 300–400 GHz and 800 GHz) lie within high atmospheric transmission windows, making them especially relevant for THz wireless communications

and passive sensing applications. Typically, THz communication systems operating at ~300 GHz have a 55-km exclusion radius for 7 dBm transmitters operating in that band [3], [19].

1.2 MMW Signal Generation

A low-phase-noise, frequency-tunable MMW source is crucial for applications like radar, wireless communications, and modern instrumentation. Conventional electronic methods rely on frequency multiplication, which is complex, expensive, and inefficient for long-distance transmission due to high losses in coaxial cables. Optical techniques, leveraging the wide bandwidth and low-loss properties of optical fibers, provide a more effective solution, enabling centralized signal generation and seamless distribution to remote sites. The following sections discuss key optical approaches for MMW generation, highlighting their advantages and challenges [35]. The following sections summarize the primary optical methods used for MMW generation.

1.2.1 Optical Injection Locking

One approach to generating high-quality MMW signals involves optical injection locking, which ensures strong phase coherence between the two optical waves used for heterodyning. This technique employs a master laser whose frequency is modulated by a RF reference, generating optical sidebands. These sidebands are then used to injection-lock two slave lasers, whose free-running wavelengths are close to the desired sideband frequencies. As a result, the two slave lasers produce phase-correlated optical signals that, when heterodyned at a PD, generate a beat note with low phase noise [36].

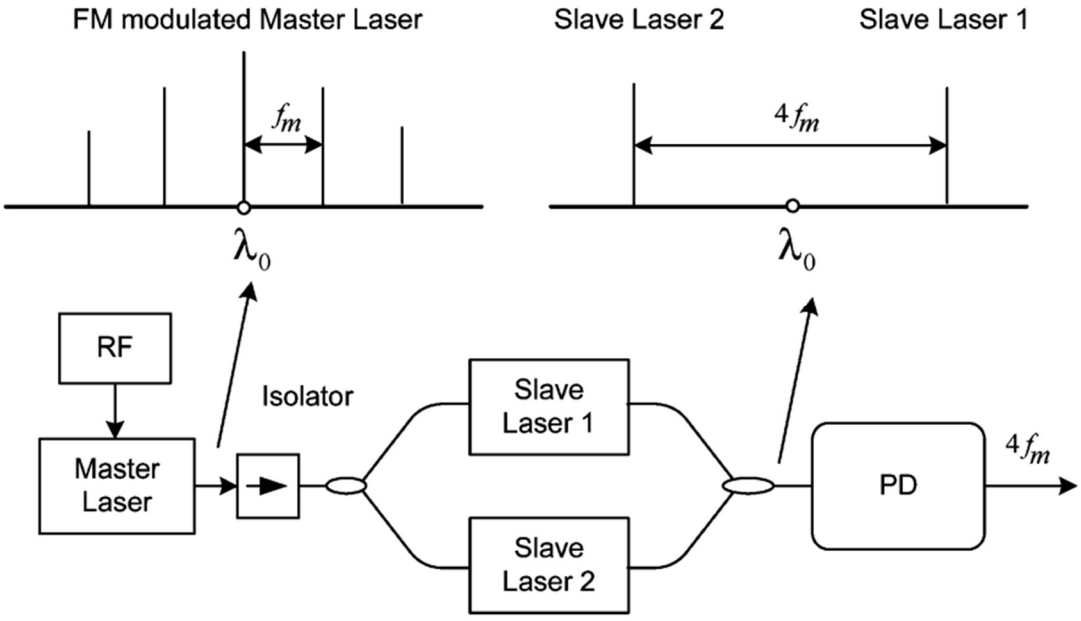

Fig. 1.3 Schematic of optical injection locking of two slave lasers [35].

Fig. 1.3 illustrates an optical injection locking system comprising a master laser and two slave lasers. An RF reference is applied to the master laser, inducing frequency modulation (FM) and generating an optical carrier along with multiple orders of optical sidebands. The output of the master laser is then injected into the two slave lasers, which are carefully selected such that their free-running wavelengths align with two specific sidebands—typically the +2nd-order and -2nd-order sidebands in the figure. As a result, the wavelengths of the slave lasers become locked to these sidebands, achieving optical injection locking.

Optical injection locking enables phase coherent signals for MMW generation while this approach requires careful design to maintain mode selection and injection-locking conditions, making system complexity a potential challenge.

1.2.2 Optical Phase-Locked Loop

Another method for achieving phase coherence between two optical waves is the optical phase-locked loop (OPLL), where the phase of one laser is actively locked to that of another, as illustrated in Fig. 1.4. This technique has been extensively studied in recent years [37],

[38]. For effective phase locking, the lasers must possess narrow linewidths, ensuring that phase fluctuations occur only at low frequencies, which in turn relaxes the requirement for an ultra-fast feedback loop.

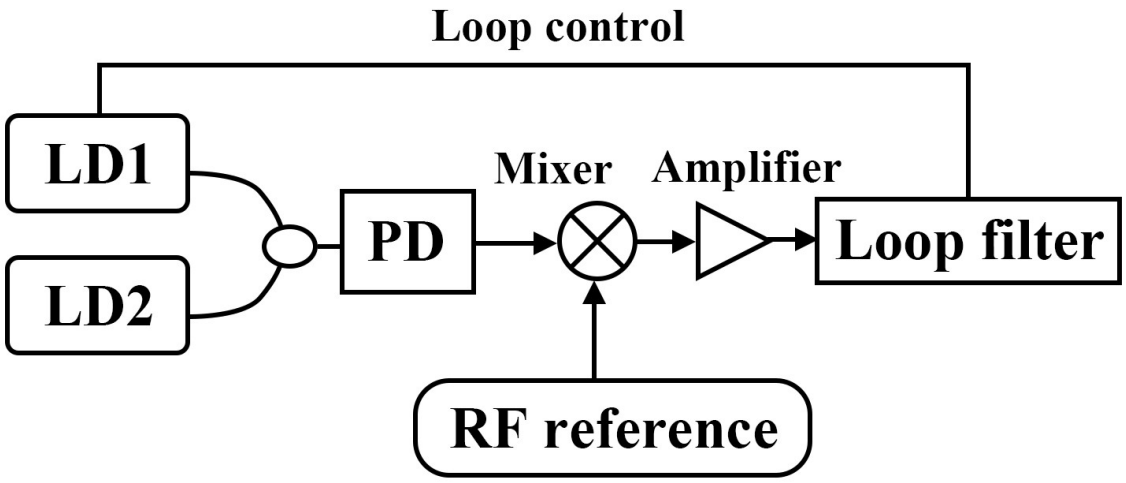

Fig. 1.4 Schematic of an optical phase lock loop.

As shown in Fig. 1.4, the heterodyne beat note is generated at the output of the PD and compared with an RF reference from a microwave generator. This comparison is performed by a mixer, followed by a low-pass loop filter. The phase detection module produces an error voltage proportional to the phase difference between the beat note and the RF reference. This error signal is then fed back to adjust the laser cavity length or injection current, thereby controlling the phase of one laser. With a properly designed feedback loop gain and response time, the relative phase fluctuations between the two lasers are significantly minimized, resulting in a beat note phase-locked to the RF reference, ensuring stable and precise MMW generation [39]. Using OPLL, Nd:YAG lasers have successfully generated tunable microwave signals from 6 to 34 GHz with linewidths below 1 MHz [40].

The OPLL system provides high-frequency stability and low phase noise, making it ideal for precision MMW generation, while the technique requires narrow-linewidth lasers and an optimized feedback loop, adding system complexity and cost.

1.2.3 MMW Generation based on Dual-Wavelength Lasers

MMW signals can also be generated using dual-wavelength lasers, where two optical modes are produced within the same cavity, separated by a fixed frequency [41]. Since they originate from the same laser cavity, their phase correlation is inherently better than that of two independent free-running lasers. One implementation utilizes a dual-wavelength fiber ring laser incorporating a sampled fiber Bragg grating (FBG) with two embedded equivalent phase shifts. This design enables dual-mode operation by precisely selecting two transmission peaks within the grating spectrum [42]. This method has demonstrated stable MMW signals at 18.68 GHz, 40.95 GHz, and 6.95 GHz, with spectral widths as narrow as 80 kHz and frequency stability better than 1 MHz in free-running mode. The dual-wavelength laser approach offers a simple, cost-effective solution without the need for external RF references or complex feedback systems. Although the phase correlation between the two wavelengths is better than in separate free-running lasers, it remains inferior to actively locked systems, potentially leading to higher phase noise.

Table 1.1 Comparison of Photonic MMW Generation Techniques

Method	**Advantages**	**Limitations**	**Typical Performance**
Optical Injection Locking	Strong phase coherence, low phase noise, no feedback loop needed	Sensitive to detuning, requires careful slave/master design	Linewidth ~kHz
OPLL	High frequency stability, ultra-low phase noise, precise tuning	Requires narrow-linewidth lasers- Complex feedback electronics	<1 MHz linewidth, tunable 6–34 GHz [40]

DWL	Compact and low-cost, no external reference, easier integration	Moderate phase noise, limited tuning accuracy	~80 kHz linewidth, up to ~40 GHz [42]

In summary, a comparative table of these photonic MMW generation techniques, highlighting their respective advantages, limitations, and typical performance, is provided in Table 1.1. The RF signal demonstrated in this work using a monolithically integrated dual-wavelength laser (DWL) offers a compact and promising solution, combining frequency stability with system simplicity.

1.3 THz Signal Generation

Photonic-based methods for THz generation, leveraging optical and optoelectronic techniques, offer promising solutions due to their high efficiency and broadband capabilities [43]. Several key strategies have been developed for THz generation, including quantum cascade lasers (QCLs), PCA, difference frequency generation (DFG), and optical rectification [44], [45], [46], [47], [48], [49].

1.3.1 Quantum Cascade Lasers

QCL is a type of semiconductor-based THz sources initially proposed by Kazarinov and Suris, were first realized by Faist et al. in the MIR regime and later extended to the THz range by Köhler et al [50], [51], [52]. Conventional semiconductor lasers operate as bipolar devices, where optical emission occurs through interband transitions. Under sufficient excitation, population inversion is achieved between the conduction and valence bands, leading to stimulated emission, as illustrated in Fig. 1.5(a). In contrast, QCLs are unipolar

semiconductor lasers, where photon emission is generated through intersubband transitions within a series of coupled QWs or superlattices. Driven by an applied electric field, electrons undergo a cascading process, sequentially transitioning between subbands and emitting photons at each stage, as shown in Fig. 1.5(b). A key advantage of QCLs lies in their wavelength tunability, which is not constrained by the intrinsic bandgap of the material but is instead engineered through precise control of the QW and barrier thicknesses in the active region. This enables flexible and wide-range spectral tailoring, making QCLs highly versatile for THz emission applications.

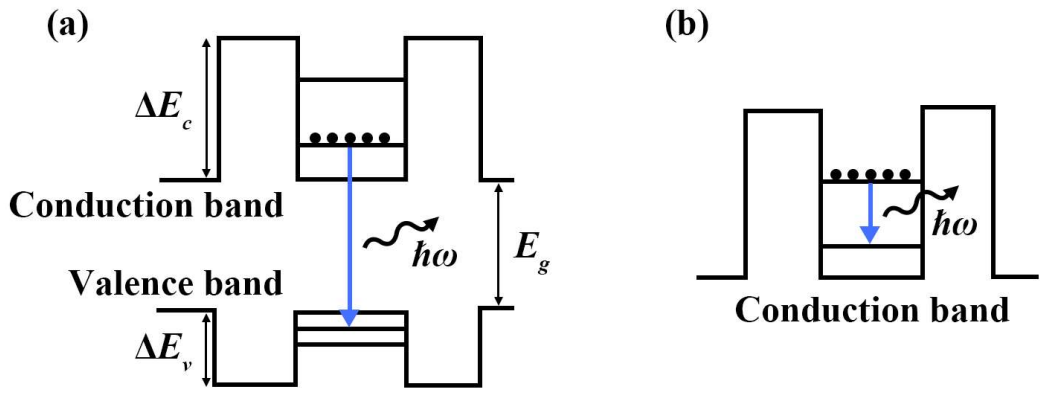

Fig. 1.5 Schematic diagram of electron transitions in (a) conventional semiconductor lasers and (b) QCLs.

Notably, Interband Cascade Lasers (ICLs) have also emerged as a complementary solution to QCLs in the field of semiconductor laser technologies [53], [54], [55]. While QCLs exploit intraband transitions within the conduction band and are predominantly used for high-power and high-frequency applications, ICLs rely on interband transitions between the conduction and valence bands. This fundamental difference in carrier dynamics enables ICLs to operate at much lower threshold currents and power consumption, making them especially suitable for continuous-wave (CW) applications at room temperature [56], [57]. ICLs are typically based on type-II InAs/GaSb/AlSb heterostructures, which offer favorable band alignment and lattice matching for efficient photon generation in the MIR spectrum. Their emission wavelengths range from 2.7 to 11.2 μm, corresponding to frequencies between

approximately 27 and 111 THz. Although primarily used in MIR applications such as gas sensing, free-space communication, and medical diagnostics [58], ICLs can also contribute to THz systems through nonlinear processes like DFG. Their cascaded structure enables high quantum efficiency with compact device footprints, positioning ICLs as a promising low-power alternative for potential THz photonic platforms.

1.3.2 THz Time-Domain Spectroscopy

THz radiation was initially characterized using terahertz time-domain spectroscopy (THz-TDS). In this technique, broadband THz pulses are generated and detected using nonlinear optical methods or PCAs, enabling the measurement of both the amplitude and phase of the THz electric field in the time domain [59], [60].

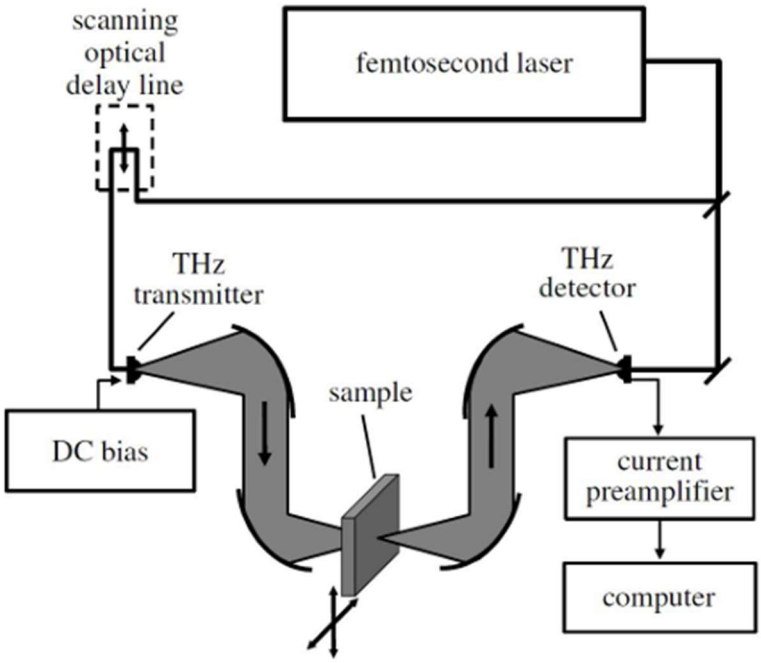

Fig. 1.6 Schematic of a THz-TDS imaging system [28].

Fig. 1.6 shows a typical THz-TDS imaging system, which uses a femtosecond laser to generate ultrashort pulses (~100 fs). The beam is split into two paths: one excites the THz transmitter to generate THz pulses, while the other gates the detector. A scanning delay line

introduces temporal offset for time-resolved sampling. THz pulses, generated via mechanisms like PCAs or optical rectification [22], [60], [61], are collimated, focused onto the sample, and detected after transmission. While widely used in spectroscopy and imaging, conventional THz-TDS systems are often bulky and expensive, highlighting the need for compact, low-cost alternatives.

1.3.3 Dual Wavelength Photomixing

For applications requiring stable and narrow-linewidth THz radiation, continuous wave (CW) THz generation is a highly suitable approach, offering enhanced spectral resolution within a predefined linewidth. A widely adopted method for CW THz generation is photomixing, which involves the interference of two CW lasers with a precisely controlled frequency difference in the THz range. These optical signals are combined via a beam splitter and subsequently focused onto a PCA, where the optical beating induces a periodic photocurrent that excites THz emission coupled into free space. The pioneering demonstration of CW THz generation through photomixing was reported by Verghese et al., utilizing two CW Ti:sapphire lasers [62]. Furthermore, PCA-based receivers, bolometers, and Golay cells serve as viable detection mechanisms for THz signals, with ongoing research focusing on the integration of transmitters and detectors into compact transceiver modules [63], [64], [65].

To illustrate the principles of photomixing, two optical fields with angular frequencies ω_1 and ω_2 can be expressed as:

$$\begin{aligned} \tilde{E}_1(t) &= E_1(z)\exp(i\omega_1 t + \phi) + c.c \\ \tilde{E}_2(t) &= E_2(z)\exp(i\omega_1 t) + c.c \end{aligned} \tag{1.1}$$

where *c.c.* is the complex conjugate and ϕ is the relative phase between two optical fields. The intensity I of the total field can then be defined as the square of the sum of the two optical waves:

$$\begin{aligned}\tilde{I}(t) &= {E_1}^2\cos^2(\omega_1 t+\phi)+{E_2}^2\cos^2(\omega_2 t)+2E_1E_2\cos(\omega_1 t+\phi)\cos(\omega_2 t)\\ &= \frac{{E_1}^2}{2}+\frac{{E_2}^2}{2}+{E_1}^2\frac{\cos(2\omega_1 t+2\phi)}{2}+{E_2}^2\frac{\cos(2\omega_2 t)}{2}\\ &\quad +E_1E_2\cos[(\omega_1+\omega_2)t+\phi]+E_1E_2\cos[(\omega_1-\omega_2)t+\phi]\end{aligned} \tag{1.2}$$

where the final difference frequency term is of interest. When the frequency difference of the two wavelengths (ω_1 - ω_2) is in the THz frequency range, THz signals can be generated by photomixing in a high-speed detector. Because of the limited bandwidth of the detector, the sum frequencies of other frequency harmonics are ignored and only THz frequencies are detected and generated.

A typical THz PCA consists of two metallic electrodes, often made of gold, patterned onto a photoconductive substrate. Common photoconductive materials include high-resistivity GaAs, InP, InGaAs, and radiation-damaged silicon wafers [66]. The metallic electrodes serve to provide a bias voltage while also forming the antenna structure, which must be carefully designed to achieve resonance at the target THz frequency corresponding to the difference between the two optical wavelengths. The antenna geometry and dimensions play a critical role in determining its operational efficiency and spectral response.

In addition, ultrafast photodetectors (PDs) with high-frequency responses have also been explored for THz generation. These detectors are typically designed with modified p-i-n structures to achieve reduced carrier transit times, lower load resistance, and minimized intrinsic and parasitic capacitances. Two well-established architectures include the traveling-wave photodiode (TW-PD) [67] and the uni-traveling carrier photodiode (UTC-PD) [68], [69], [70]. The UTC-PD has demonstrated significant potential for high-power CW THz generation, where the UTC-PD is illuminated by two CW lasers with a fixed frequency spacing. The optical beat generates a photocurrent oscillating at the THz frequency, effectively creating an electrical THz signal. While this electrical signal is not inherently a propagating electromagnetic wave, it can be converted into radiated THz waves by attaching a high-speed antenna or through suitable packaging. It is important to clarify that UTC-PDs

are not used for detecting incoming THz waves; their function is purely in signal generation. In contrast, PCAs are versatile components that can operate both as emitters and detectors of broadband THz waves, especially in THz time-domain spectroscopy setups.

1.4 Mode-locked Semiconductor Lasers

1.4.1 Mode-locking Technique

Mode-locking constitutes a pivotal methodology in ultrafast photonics for generating coherent optical pulses with durations ranging from picosecond to femtosecond regimes. This technique fundamentally relies on establishing fixed phase relationships between longitudinal cavity modes, as mathematically described by:

$$E(t) = \sum_{q=-N}^{N} E_q \exp[i(\omega_0 + q\Delta\omega)t + i\phi_q] \tag{1.3}$$

Where ϕ_q denotes the phase of the q^{th} mode. When phase locking condition $\phi_q = \phi_0$ is satisfied, the temporal intensity evolves into a pulse train with repetition rate $f = c/(2n_gL)$, where n_g represents the group refractive index. The pulse duration $\Delta\tau$ is intrinsically governed by the spectral bandwidth $\Delta\lambda$ through the time-bandwidth product relation:

$$\Delta\tau \cdot \Delta v \geq K \tag{1.4}$$

Where K characterizes the Fourier-transform limit. Gain bandwidth limitations vary significantly across different laser architectures. In a typical helium-neon (He-Ne) laser, the gain bandwidth is approximately 1.5 GHz, corresponding to a narrow wavelength range of about 0.002 nm at a central wavelength of 633 nm. In contrast, titanium-doped sapphire (Ti:sapphire) lasers exhibit much broader gain bandwidths, reaching up to 300 nm around 800 nm, enabling sub-10 fs pulses. Semiconductor lasers typically have gain bandwidths in the order of tens of nanometers, which is sufficient for generating femtosecond mode-locked

pulses. For instance, a semiconductor laser operating at 1550 nm with a 20 nm spectral bandwidth can achieve a transform-limited pulse duration of 259 fs. In practical implementations of semiconductor mode-locked lasers (MLLDs), the actual pulse duration often exceeds theoretical limits due to chirp accumulation from nonlinear refractive index, group delay dispersion in waveguide structures, and self-phase modulation [71], [72], [73], [74], [75].

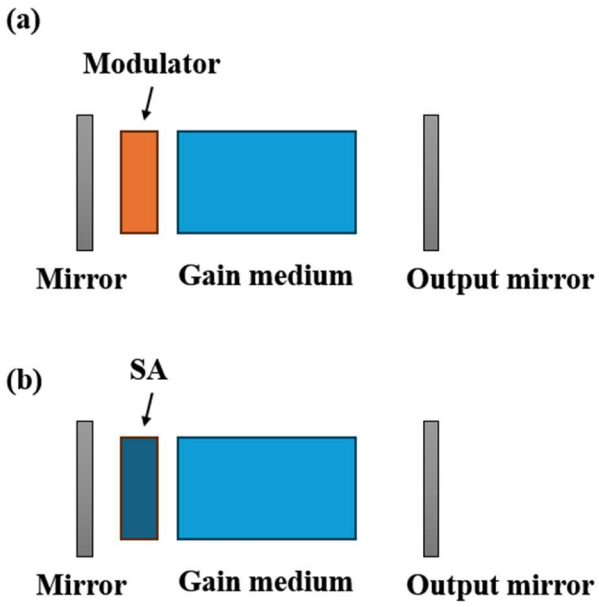

Fig. 1.7 schematic of **(a)** active mode-locking, and **(b)** passive mode-locking.

There are two fundamental approaches to achieving mode-locking in a laser: active mode-locking and passive mode-locking. In active mode-locking, a modulator is incorporated into the laser cavity to regulate either resonator losses or cavity phase variations, as illustrated in Fig. 1.7(a). The modulator can take the form of an acousto-optic modulator, an electro-optic modulator, or an electro-absorption modulator. When the modulation frequency is synchronized with the resonator round-trip time, ultrashort pulses can be generated [72].

Unlike active mode-locking, passive mode-locking does not require external signal modulation as shown in Fig. 1.7(b). This approach enables the generation of significantly

shorter pulses, typically on the femtosecond scale. Passive mode-locking is commonly achieved using a saturable absorber (SA), which facilitates pulse formation by selectively absorbing lower-intensity light while allowing higher-intensity pulses to propagate [76], [77]. Crucially, the SA's recovery time τ_{SA} must satisfy $\tau_{SA}<T$ (round-trip time) to ensure effective pulse shortening per cavity round-trip. In semiconductor quantum-well SAs, this process is further governed by carrier dynamics: photoexcited carriers rapidly thermalize (sub-picosecond timescale) through carrier-carrier scattering, followed by slower recombination processes (~100 ps). Such time-scale separation enables the formation of sub-ps pulses through dynamic balance between spectral filtering (SA nonlinearity) and dispersion compensation (e.g., chirped Bragg reflectors) [78], [79], [80].

1.4.2 Mode-locked Lasers in Sub-THz Regime

MLLDs have become an essential tool for generating sub-THz pulsed signals in the 200 GHz to 1 THz frequency range, enabling applications in wireless communication, high-resolution spectroscopy, and ultrafast imaging. By leveraging phase-coherent interference of longitudinal cavity modes, MLLDs produce periodic ultrashort optical pulses that can be converted into stable, high-purity sub-THz radiation via photomixing techniques or direct optical-to-THz conversion in semiconductor-based active structures [81], [82].

There are various approaches to design mode-locked lasers in sub-THz regime. Among various mode-locking schemes, colliding pulse mode-locking (CPM) has been widely adopted for achieving high-repetition-rate pulse trains by strategically placing multiple SA sections within the laser cavity [83], [84], [85], [86]. Unlike fundamental mode-locking, where a single SA is positioned at one facet, CPM utilizes the constructive interference of multiple circulating pulses that collide at the SA sections, enabling harmonic mode-locking (HML) at significantly higher frequencies [85], [86]. Recent advancements in CPM-based MLLDs have demonstrated repetition rates exceeding 240 GHz using optimized AlGaInAs/InP quantum-well structures, offering reduced internal losses and improved

output power [86]. The shorter absorption recovery time of AlGaInAs QWs, typically below 5 ps, plays a critical role in achieving stable HML [87]. Moreover, the reduced optical confinement factor and increased saturation energy in optimized 3 QW structures have expanded the stable mode-locking range, reduced RF linewidth, and minimized timing jitter [88].

Coupled-cavity mode-locking (CCM) is also an effective approach by integrating a short cavity within a longer gain cavity, with their lengths precisely controlled to maintain an integer ratio [89]. This configuration enables HML with strong linear modal selectivity, improving the stability of mode-locking compared to CPM [90]. Theoretical and experimental studies have demonstrated that CCM lasers operating at telecom-relevant wavelengths (1.55 μm) can achieve repetition frequencies up to 160 GHz, utilizing deeply etched intracavity reflectors (ICRs) to enhance mode discrimination and stability [91]. Experimental results confirm that single-slot ICR designs yield the most stable harmonic mode-locking at the fourth harmonic, with pulse widths below 1.52 ps and time-bandwidth products (TBP) close to transform-limited values [90]. However, precise cleaving is essential for achieving optimal performance, as minor deviations in cavity length can shift the selected harmonic mode. While CCM lasers have demonstrated strong performance, their scalability to higher harmonic numbers is constrained by fabrication tolerances.

While CPM and CCM have demonstrated the capability of generating high-repetition-rate optical pulses, these approaches face limitations such as higher harmonic limitation and stringent fabrication tolerances, which restrict their scalability to higher THz frequencies [92]. To address these challenges, sampled grating distributed Bragg reflector (SGDBR) lasers have emerged as an effective alternative, offering precise mode selection and stable mode-locking at ultra-high repetition rates [93]. By exploiting the periodic reflection properties of sampled gratings, mode-locked operation at 640 GHz and even 1.28 THz has been achieved, exceeding the frequency limits of CPM and CCM methods [94]. A significant advantage of SGDBR-based mode-locking is its ability to mitigate the dependency on

cleaving precision while maintaining broad tunability through injection current control. Additionally, the introduction of π-phase shifted SGDBRs (PPS-SGDBR) has enhanced the effective coupling coefficient, leading to a sharper and more defined reflection spectrum, further improving harmonic mode-locking stability [94]. However, despite these advantages, achieving optimal spectral alignment between the gain section and the SGDBR remains crucial, and dispersion management is necessary to maintain pulse quality. Overall, the implementation of SGDBR structures represents a significant advancement in semiconductor-based THz pulse generation, providing a promising pathway for compact and integrable ultrafast laser sources.

1.4.3 Autocorrelator

Among the MLLD mentioned before, due to their femtosecond-scale durations, ultrashort optical pulses cannot be directly measured using conventional optoelectronic devices. To overcome this limitation, the second harmonic generation (SHG) autocorrelation technique is well-known to measure the temporal characteristics of ultrafast laser pulses [95], [96], [97]. In this study, an intensity autocorrelator was used to characterize ultrashort pulse durations, enabling the measurement of autocorrelation (AC) traces. This method eliminates the need for a high-speed PD, requiring only a slow PD to capture the signal. The nonlinear process within the autocorrelator generates a second harmonic (SH) signal, which, once detected, allows for the calculation of the pulse duration.

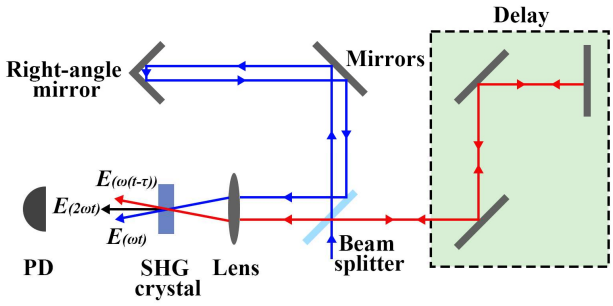

Fig. 1.8 schematic of the intensity autocorrelator with MI.

Fig. 1.8 illustrates the schematic of the intensity autocorrelator with the Michelson interferometer (MI). The optical pulse input is split into two copies by the beam splitter. One of these copies is directed through a delay line to introduce a controlled time delay before both copies are focused onto an SHG crystal using an optical lens. When the pulses temporally overlap in the nonlinear medium, a second-harmonic signal is generated due to nonlinear interaction. The SH signal then passes through an aperture to be detected by a slow PD, while the original pulses are blocked to minimize noise. By analyzing the detected signal, autocorrelation traces are obtained, from which the pulse duration is calculated.

The decay rate of the autocorrelation signal with increasing time delay (τ) is inversely related to pulse duration: shorter pulses result in faster decay. For a known pulse shape, the pulse duration can be estimated as a scaling factor of the autocorrelation signal duration. Specifically, for a Gaussian shaped pulse, this factor is approximately 0.707, while for a Hyperbolic Secant ($sech^2$) shaped pulse, it is around 0.648. However, autocorrelation traces alone do not provide exact pulse shape information, as they depend on multiple factors such as mode number and group velocity dispersion.

In this study, the AC traces resemble sinusoidal signals, as only two or three lasing modes contribute to pulse formation. Consequently, the pulses were assumed to have a sinusoidal shape, in which case the pulse duration corresponds to half of the oscillation period.

1.5 Thesis Overview

This thesis is organized into seven chapters, addressing the basic theory, fabrication process and three specific aspects of the research of semiconductor distributed feedback (DFB) and distributed Bragg reflector (DBR) lasers for MMW and THz generation. The thesis is arranged in detail as follows:

Chapter 2 presents the theory for DFB/DBR laser design, covering Bragg gratings, MQWs, and waveguide modes. The Bragg grating section introduces the Bragg condition and coupled-mode theory, alongside the transfer matrix method for optical simulation. sampled Bragg gratings (SBGs) are analyzed with various sampling schemes compared in terms of reflection spectra and mode selectivity, supported by simulation results. The MQW analysis focuses on strained quaternary III-V materials, including InGaAsP and InGaAlAs. Under strain, key parameters such as band offsets, energy levels, and gain spectra are calculated. The material gain spectrum of the designed MQW is simulated to evaluate optical performance. Finally, waveguide and optical mode simulations are performed to optimize the ridge geometry. The effective index and optical confinement factors are analyzed to ensure single-mode propagation.

Chapter 3 focuses on the material systems and fabrication processes used in realizing semiconductor diode lasers. It details the epitaxial wafer structures based on QWs, for DFB/DBR lasers. The key fabrication steps, including lithography, etching, and metallization, are described to illustrate how these processes contribute to the implementation of laser devices. The etching process of the sidewall grating uses a single-step electron beam lithography and dry etching process, eliminating grating-ridge misalignment.

Chapter 4 presents the design and characterization of a dual-wavelength DFB laser array utilizing a novel four phase-shifted SBG (4PS-SBG) for THz generation. The device integrates two 4PS-SBGs with different sampling periods on each side of the ridge waveguide, enabling efficient dual-wavelength lasing via $\pm 1^{st}$ order reflections while suppressing the undesired 0^{th} channel. Compared to conventional SBGs (C-SBGs), the 4PS-SBG structure exhibits a threefold enhancement in coupling efficiency and enables precise wavelength spacing control. The laser demonstrates stable dual-mode operation over a 40-mA current range, with a power difference below 3 dB and side mode suppression ratio (SMSR) exceeding 30 dB. Dual-mode frequency spacings ranging from 320 GHz to 1 THz

are realized, and photomixing-based THz generation is experimentally verified with up to 12.8 μW output power.

Chapter 5 introduces a novel dual-wavelength DFB laser employing a four phase-shifted sampled Moiré grating (4PS-SMG) for MMW generation. The grating integrates two distinct sampling periods to form dual equivalent π phase shifts, enabling stable dual-mode lasing. The fabricated device demonstrates robust dual-mode operation across a wide DFB current range (130–210 mA), maintaining <2 dB power difference and >25 dB SMSR. Under dual-mode conditions, a high-quality RF signal is generated with a −3 dB linewidth of ~5 MHz. The emission frequency is thermally tunable from 39.8 to 39.0 GHz between 10 °C and 30 °C.

Chapter 6 presents mode-locked DBR (ML-DBR) and DFB (ML-DFB) lasers employing multiple phase-shifted gratings (MPSGs) for THz generation. The optimized MPSG design enables uniform reflectivity across multiple channels and precise control of coupling coefficients, facilitating efficient mode-locking and dense channel spacing. ML-DBR lasers operating at 150 GHz, 400 GHz, 800 GHz, and 1.2 THz are experimentally demonstrated with consistent repetition rates, validated by autocorrelator. A 200 GHz ML-DFB laser incorporating an equivalent π-phase shift (EPS) achieves stable multi-channel lasing. When amplified and injected into a PCA, the ML-DFB laser generates a 19.6 μW THz signal.

Chapter 7 concludes the thesis by summarizing the main contributions and innovations achieved in this work. It highlights the significance of the developed devices in the context of integrated MMW/THz sources and outlines potential directions for future research.

Chapter 2 Theory

2.1 Bragg Grating Analysis

2.1.1 Bragg Condition

Bragg gratings are formed by introducing a periodic perturbation along the propagation direction of an optical waveguide. In a simplified model of a Bragg grating, as shown in Fig. 2.1, the refractive indices of the waveguide core and cladding are denoted as n_1 and n_2, respectively.

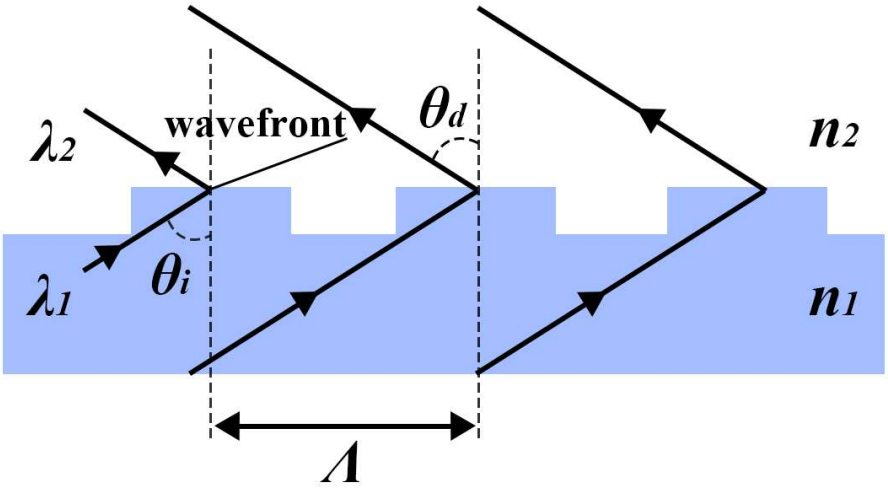

Fig. 2.1 Schematic of diffraction grating.

Since light with a frequency experiences different wavelengths in materials with different refractive indices, the wavelengths in the core and cladding are represented as λ_1 and λ_2, respectively. The grating has a period of Λ, and when a plane wave is incident at an angle θ_i, the diffracted light exits at an angle θ_d. According to Huygens' principle, constructive interference occurs when the total optical path difference equals an integer multiple of 2π.

$$\frac{\Lambda \sin\theta_i}{\lambda_1} \pm \frac{\Lambda \sin\theta_d}{\lambda_2} = m \tag{2.1}$$

Where m is an integer indicating the diffraction order. The incident and diffracted light in Eq. (2.1) have a positive sign when they are on the same side of the normal line. For waveguides, the incident angle must satisfy the total internal reflection condition, meaning it must be greater than the critical angle θ_c which is:

$$\sin\theta_i \geqslant \sin\theta_c = \frac{n_2}{n_1} = \frac{\lambda_1}{\lambda_2} \tag{2.2}$$

Combine Eq. (2.1) and Eq. (2.2), we can get:

$$\sin\theta_d \geqslant \left(\frac{m\lambda_2}{\Lambda} - 1\right) = \left(\frac{2m}{q} - 1\right) \tag{2.3}$$

The order of the grating q is given by $q = 2\Lambda/\lambda_2$. Since the refractive index difference between the core and cladding is typically small, we approximate $\lambda_1 \approx \lambda_2 \approx \lambda_m$, where λ_m represents the effective wavelength in the waveguide. For laser structures with feedback along the waveguide direction, the angles θ_i and θ_d are typically close to π/2, which leads to a grating order q equal to the diffraction order m. Given the grating period Λ, the free-space wavelength λ_b at which strong reflection occurs is called the Bragg wavelength and satisfies the Bragg condition:

$$\lambda_b = 2n_{eff}\Lambda \tag{2.4}$$

where n_{eff} is the effective refractive index of the guided mode. The Bragg wavelength λ_b and the wavelength λ_m propagating in the waveguide are related by $\lambda_m = \lambda_b/n_{eff}$. For DFB and DBR semiconductor lasers, the first-order grating ($q = 1$) for wavelength resonance is often adopted, because it has the largest coupling efficiency.

2.1.2 Coupled Mode Theory

The coupled mode theory (CMT) is a powerful analytical framework used to study periodically structured waveguides and photonic devices, particularly DFB and DBR lasers [98]. Originally developed to describe energy exchange in coupled waveguides and resonators, CMT has been widely applied to explain the behavior of optical modes in periodic structures such as Bragg gratings. This theory provides a precise mathematical model to describe the interaction between forward and backward propagating waves in structures with periodic perturbations, making it essential for applications in optical filtering, mode selection, and laser design.

In a DFB/DBR laser cavity, the periodic modulation of the refractive index functions as a distributed reflector, removing the need for conventional mirrors and allowing single-mode lasing with high spectral selectivity. The interaction of counter-propagating waves in these periodic structures is well described by coupled mode equations, which mathematically represent the transfer of energy between modes due to Bragg scattering.

The propagation of the electric field in a periodically modulated optical waveguide follows the fundamental wave equation:

$$\frac{d^2E}{dz^2} + k^2E = 0 \tag{2.5}$$

where E represents the electric field amplitude, k is the propagation constant and is the longitudinal coordinate within the periodic medium. By introducing a periodic variation in the refractive index and gain constant, defined as:

$$\begin{aligned} n(z) &= n + n_1\cos(2\beta_0 z) \\ \alpha(z) &= \alpha + \alpha_1\cos(2\beta_0 z) \end{aligned} \tag{2.6}$$

The system supports two interacting counter-propagating waves: a forward-propagating wave $R(z)$ and a backward-propagating wave $S(z)$. These waves satisfy the fundamental coupled mode equations:

$$\begin{aligned} \frac{dR}{dz} + (\alpha - j\delta) R &= j\kappa S \\ \frac{dS}{dz} - (\alpha - j\delta) S &= j\kappa R \end{aligned} \tag{2.7}$$

where α is the amplitude-gain coefficient and δ is a measure of the detuning of the laser mode from the Bragg wavelength. The CMT method is highly suitable for modeling uniform gratings; the mode distribution and reflection spectrum characteristics of DFB lasers can be obtained by solving Eq. (2.7).

2.1.3 Transfer Matrix Method

For DFB lasers incorporating chirped gratings or sampled gratings, the grating period and phase vary spatially along the cavity. In such cases, the conventional CMT becomes inadequate for accurately modeling structures where these parameters are axially dependent. The transfer matrix method (TMM) provides a robust alternative by discretizing the resonant cavity into multiple small segments, each assumed to have constant parameters such as gain, loss, and carrier density [99], [100], [101]. This method enables precise simulations of reflectivity spectrum, time delay spectrum and power distribution.

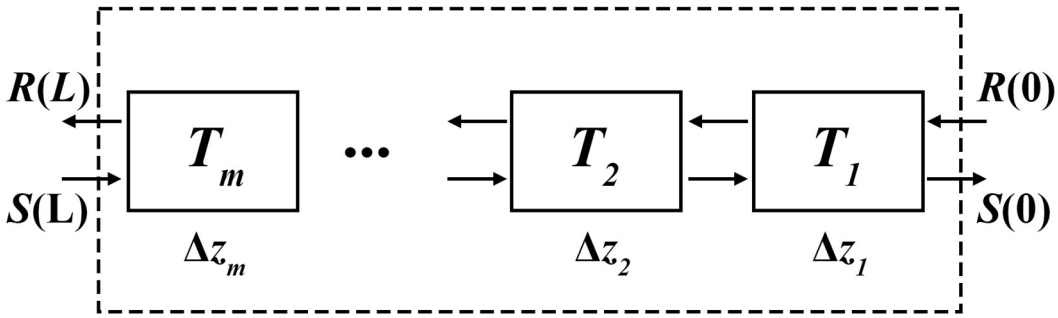

Fig. 2.2 Schematic of TMM.

Fig. 2.2 illustrates the schematic of the TMM, in which the overall optical field evolution through the entire resonator is obtained by accumulating the effects of individual segments. The forward wave *R* and backward wave *S* propagating waves are related to the accumulated net transfer matrix *T*, which is given by:

$$\begin{bmatrix} R(L) \\ S(L) \end{bmatrix} = T_m T_{m-1} \cdots T_2 T_1 \begin{bmatrix} R(0) \\ S(0) \end{bmatrix} = T \begin{bmatrix} R(0) \\ S(0) \end{bmatrix} \tag{2.8}$$

The full set of transmission matrices used in the modeling is provided in [99]. Typically, for phase-shifted gratings, the Bragg gratings are not continuous and there is a phase shift φ. The corresponding phase-shift matrix is given as:

$$T_\varphi = \begin{bmatrix} \exp\left(\frac{-j\varphi}{2}\right) & 0 \\ 0 & \exp\left(\frac{j\varphi}{2}\right) \end{bmatrix} \tag{2.9}$$

One of the key advantages of TMM is its ability to model not only periodic gratings but also structures with discontinuities (such as phase shifts) and non-periodic features. Rozzi et al. successfully applied TMM to the rigorous analysis of second-order gratings, including the detailed evaluation of all radiation modes. Furthermore, comparative studies by Makino demonstrated that TMM and CMT yield equivalent results for uniform gratings [101].

To validate the accuracy and effectiveness of the TMM, I first examined the spectral characteristics and time-domain response of a uniform Bragg grating (UBG). In this simulation, a 1-mm-long uniform grating was modeled with a center Bragg wavelength of 1550 nm and an effective refractive index of 3.19. To facilitate subsequent time-domain analysis, the frequency shift was used as the x-axis for spectral characterization.

Fig. 2.3(a) presents the reflection and transmission spectra of UBG. As expected, a bandgap appears around the Bragg frequency, where incident light is strongly reflected, preventing

transmission through the grating. In Fig. 2.3(b), the reflection spectrum is plotted in dB scale, along with the corresponding group delay spectrum. Notably, the two low reflection points closest to the main reflection lobe exhibit relatively higher group delays. This indicates that in a DFB cavity constructed with a UBG, these frequency components experience prolonged propagation within the grating. Consequently, they accumulate greater optical gain, ultimately emerging as the dominant lasing modes of the laser.

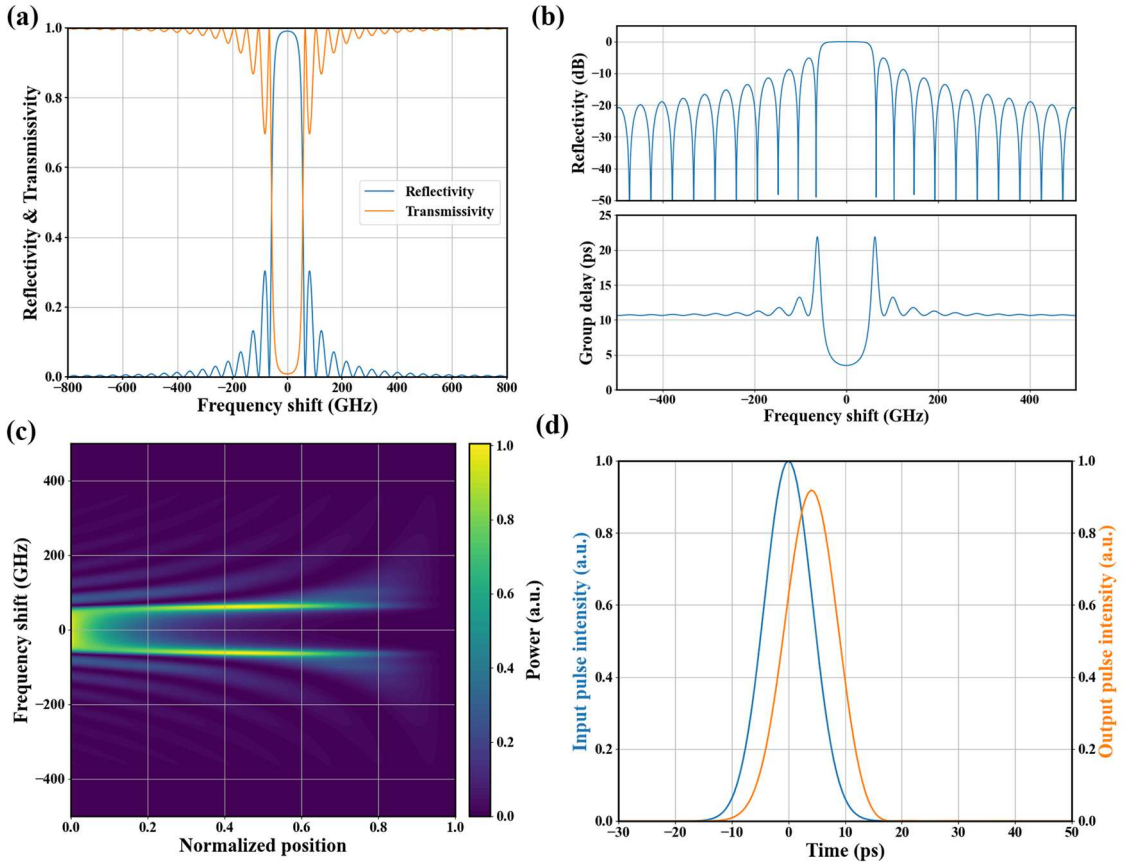

Fig. 2.3 Characteristics of the UBG: **(a)** reflection and transmission spectrum, **(b)** reflection spectrum in dB and group delay, **(c)** power distribution of forward propagating wave, **(d)** time domain response.

One major advantage of the TMM approach is its ability to provide a spatially resolved power spectrum along the propagation direction. This allows us to observe how different frequency components interact with the grating at different locations. Fig. 2.3(c) illustrates the forward optical power distribution for frequencies corresponding to the main reflection

peak and the adjacent side lobes of the UBG reflection spectrum. A key observation is that the power distributions for frequencies equidistant from the center frequency exhibit symmetry, consistent with the symmetry of the group delay spectrum in Fig. 2.3(b). Inside the main reflection lobe, the contour lines in Fig. 2.3(c) progressively extend toward the grating's end as the frequency offset increases. This suggests that forward-propagating light penetrates deeper into the grating before being reflected, effectively shifting the equivalent reflection point spatially toward the end of the grating. To further analyze the UBG response, a Gaussian pulse was used as an input probe, and the reflected pulse was examined (see Fig. 2.3(d)). The main reflection pulse remains nearly identical in shape but with reduced intensity. This is because light within the stopband is reflected immediately upon entering the grating, carrying most of the incident pulse energy.

In DFB lasers, a π-phase shift is often introduced to facilitate mode selection. The π-phase shift modifies the standing wave conditions within the cavity, effectively creating a localized defect state within the bandgap. To illustrate this effect, I introduced a π-phase shift at the center of the previously analyzed UBG and obtained the results shown in Fig. 2.4. The most notable feature is the emergence of a zero-reflection point at the center of the stopband. This indicates that a resonant mode has been introduced within the photonic bandgap. From the group delay spectrum in Fig. 2.4(b), it is evident that the Bragg-frequency mode exhibits the highest group delay. This means that in a DFB laser incorporating a π-phase shift, this mode undergoes self-excitation and amplification through stimulated emission, ultimately evolving into the primary lasing mode of the laser. From the power distribution in Fig. 2.4(c), the main optical power gathers around the center of the cavity with the Bragg frequency. As shown in Fig. 2.4(d), after reflection the Gaussian beam exhibits two distinct pulse components. The first pulse corresponds to the portion of the incident light that is immediately reflected upon entering the grating, carrying less energy than the input pulse due to partial transmission into the structure. The second pulse arises from light components that match the Bragg frequency, which propagate deeper within the grating and experience

prolonged interaction before being reflected. Due to dispersion effects, this delayed pulse undergoes temporal broadening as different spectral components travel at varying group velocities, further extending its duration.

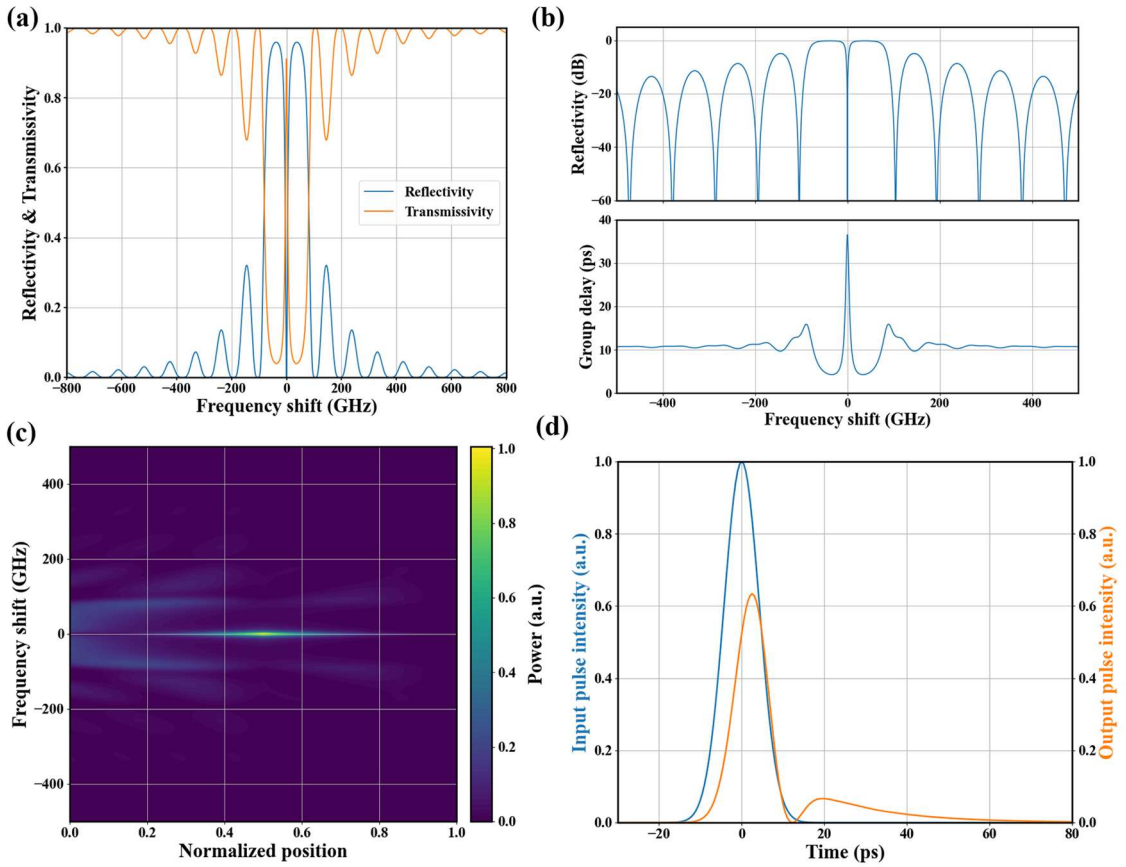

Fig. 2.4 Characteristics of the UBG with a centered π-phase shift: **(a)** reflection and transmission spectrum, **(b)** reflection spectrum in dB and group delay, **(c)** power distribution of forward propagating wave, **(d)** time domain pulse response.

In this work, the π-phase shift is implemented within the DFB grating, not the DBR reflector. The π-phase shift creates a transmission peak at the center of the stopband, which corresponds to the mode experiencing the longest photon lifetime and hence the greatest amplification. This facilitates robust single-mode lasing. In dual-wavelength designs, asymmetric gratings on either side of the cavity enable the formation of two distinct π-shift-induced resonance peaks, supporting dual-mode operation.

2.1.4 Sampled Bragg Grating (SBG)

The Bragg Condition has given a way to control the center wavelength by changing the pitch of the grating as described in Eq. (2.4). However, the grating pitch is usually on the scale of hundred nanometers. It's likely to exceed the resolution of electron beam lithography (EBL) if a small wavelength difference needs to be achieved. SBG is a structure that can control the center wavelength more precisely. The sampling period is usually on the scale of microns. Compared to the uniform grating periods, which are only of the order of several hundred nanometers, SBG can be used in more complex designs.

To establish a general mathematical formulation for SBGs, we can begin with the refractive index modulation of a UBG and introduce a sampling function $s(z)$. For a typical Bragg reflector, the refractive index modulation along the longitudinal position z within the cavity can be expressed as:

$$n(z) = n_0 + \Delta n(z) \tag{2.10}$$

Here, n_0 and Δn denote the fundamental effective refractive index and the refractive index modulation along the laser cavity, respectively. The refraction index modulation is typically expressed as a cosine function. In a periodic sampling structure, we can define a spatial sampling function $s(z)$, which is then incorporated into the refractive index modulation. By applying Euler's formula and introducing $s(z)$, the periodic variation of the refractive index modulation can be formulated as:

$$\Delta n(z) = \frac{1}{2} s(z) \Delta n \exp(j \frac{2\pi z}{\Lambda_0}) + c.c \tag{2.11}$$

Where $s(z)$ represents the sampling function, which may incorporate apodization, chirp, and phase information depending on the specific structure. It is a periodic function with a sampling period of P. Λ_0 denotes the seed grating period, and Δn is the refractive index

modulation depth. Based on Fourier analysis, the sampling function can be expressed as a summation of harmonic series:

$$s(z) = \sum_m F_m \exp\left(j\frac{2m\pi z}{P}\right) \tag{2.12}$$

where m is the integer index number corresponding to the Fourier series components. Substituting this expansion into Eq. (2.11) and reorganizing the exponential terms, the refractive index modulation takes the form:

$$\Delta n(z) = \frac{1}{2}\Delta n \sum_m F_m \exp\left[j2\pi z\left(\frac{1}{\Lambda_0} + \frac{m}{P}\right)\right] + c.c \tag{2.13}$$

By comparing with Eq. (2.11) for each harmonic component, we observe that the refractive index modulation results in a superposition of multiple channels, each with an effective grating period different from the original UBG period. The effective period of the m^{th}-order channel, also known as the ghost period, can be expressed as:

$$\frac{1}{\Lambda_m} = \frac{1}{\Lambda_0} + \frac{m}{P} \tag{2.14}$$

Each of these channels corresponds to a distinct Bragg wavelength, meaning that the seed grating with a period of Λ_0 defines the 0^{th}-order channel that is physically present in the SBG structure. This mathematical formulation allows us to determine the wavelength spacing between different order channels in an SBG, which is crucial for designing sampled gratings tailored for multi-wavelength laser applications.

Fig. 2.5 presents schematic illustrations of the UBG, C-SBG, two-phase-shift SBG (2PS-SBG), and 4PS-SBG sidewall gratings. For a DWL based on a UBG, the lasing wavelengths can be determined by the Bragg condition utilizing different seed grating period (Λ_1 and Λ_2)

at each side of the ridge waveguide as shown in Fig. 2.5(a). For EBL with a 0.5 nm resolution, the smallest achievable dual wavelength spacing is calculated as 3.2 nm (400 GHz at 1550 nm operation wavelength), assuming an effective refractive index of 3.20.

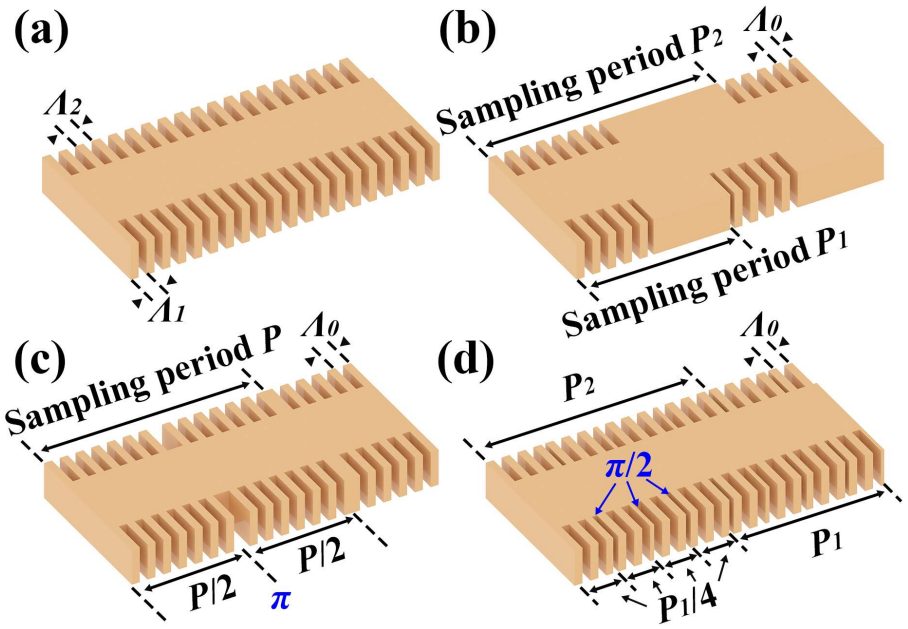

Fig. 2.5 Different sampling structures of each sampling section. **(a)** UBG, **(b)** C-SBG, **(c)** 2PS-SBG, and **(d)** 4PS-SBG.

To achieve a higher precision of the wavelength difference control, C-SBG technology can be employed, as shown in Fig. 2.5(b). The sampled grating periods on each side of the ridge waveguide are denoted as P_1 and P_2, where 50% of each period consists of a grating, while the remaining 50% is unetched. The wavelength difference between the 1st-order channels follows:

$$\Delta\Lambda_{+1} = \frac{1}{(P_1/\Lambda_0 + 1)\,(P_2/\Lambda_0 + 1)} \cdot \Delta P \tag{2.15}$$

where $\Delta P = P_2 - P_1$ is the difference in sampling periods. For C-SBGs with a seed grating period of 257 nm, the fundamental channel appears at 1630 nm, given an effective refractive index of 3.19 at 1550 nm and a waveguide dispersion coefficient of –0.00021/nm. With the 0.5 nm resolution of the EBL system, the smallest achievable grating period variation is

0.0014 nm, corresponding to a minimum channel spacing of 1.1 GHz around 1550 nm. However, a major drawback of C-SBGs is their reduced effective coupling coefficient κ, which is only $1/\pi$ a UBG [102]. Furthermore, unwanted reflections from the 0^{th}-order channel can deteriorate the performance of C-SBG-based DWLs as shown in Fig. 2.6.

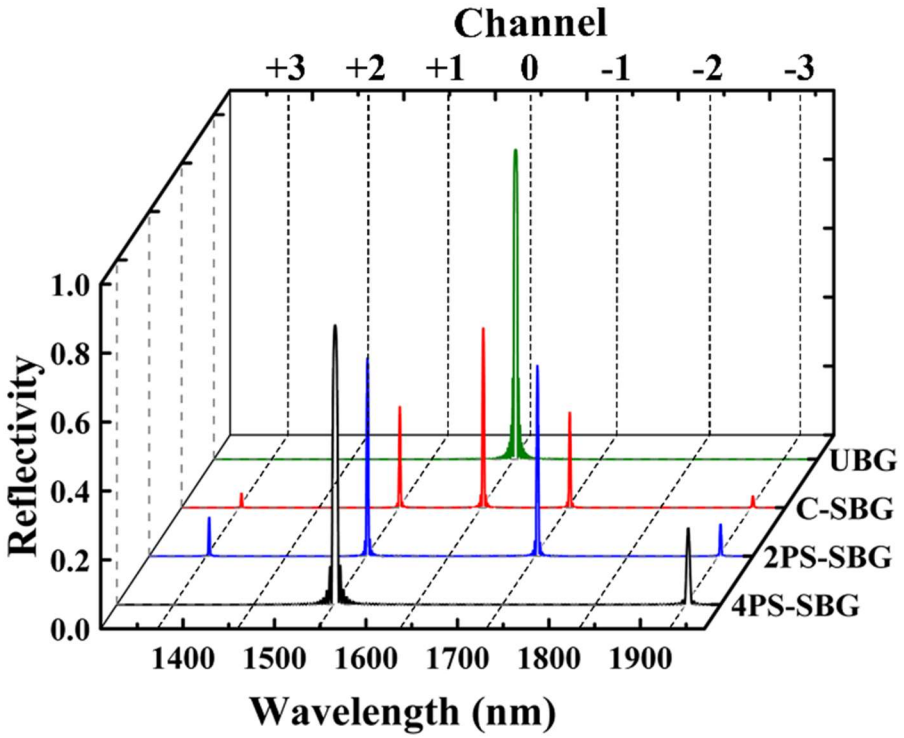

Fig. 2.6 Simulated reflectivity of UBG, C-SBG, 2PS-SBG, and 4PS-SBG.

In the 2PS-SBG configuration shown in Fig. 2.5(c), each sampling period is evenly divided into two segments, with the latter half experiencing a π-phase shift relative to the former. This simultaneously enhances the coupling coefficient of the $\pm 1^{st}$-order channels to 0.64 times that of a UBG and effectively eliminates reflections from the 0^{th}-order channel (see Fig. 2.6). The 2PS-SBG technology is particularly advantageous for THz signal generation, as it enables automatic formation of DWLs while maintaining equal sampling periods on both sides of the ridge waveguide.

To further increase the effective coupling coefficient κ, a 4PS-SBG-based DWL can be implemented. As illustrated in Fig. 2.5(d), this configuration utilizes distinct sampling

periods P_1 and P_2 on each side of the ridge waveguide. By leveraging the $+1^{st}$-order reflections, two lasing modes are generated, with the wavelength spacing between them tunable via adjustments to the sampling periods. Compared to 2PS-SBGs, 4PS-SBGs offer a higher effective coupling coefficient, reaching 0.9 times that of a UBG, as opposed to 0.64 times in 2PS-SBGs. This improvement, combined with the elimination of 0^{th}-order channel reflections, significantly mitigates the impact of unwanted longitudinal modes, leading to enhanced stability and performance in DWL operation.

In this study, a 4PS-SBG is employed to design the DWL array. To further investigate the characteristics of this grating structure, I have also computed key parameters such as group delay and time-domain response. Here, I present a filtering grating designed to generate a dual-wavelength output with a frequency spacing of 320 GHz, incorporating a π-phase shift at the center of the cavity. As shown in Fig. 2.7(a), the reflection spectrum reveals the formation of two zero-reflection points, denoted as f_1 and f_2, within the two stopband lobes. These correspond to a frequency spacing of 320 GHz, ensuring the desired dual-wavelength operation. Fig. 2.7(b) illustrates the computed group delay spectrum, where the two delay peaks at f_1 and f_2 correspond to the two primary lasing modes of the laser cavity.

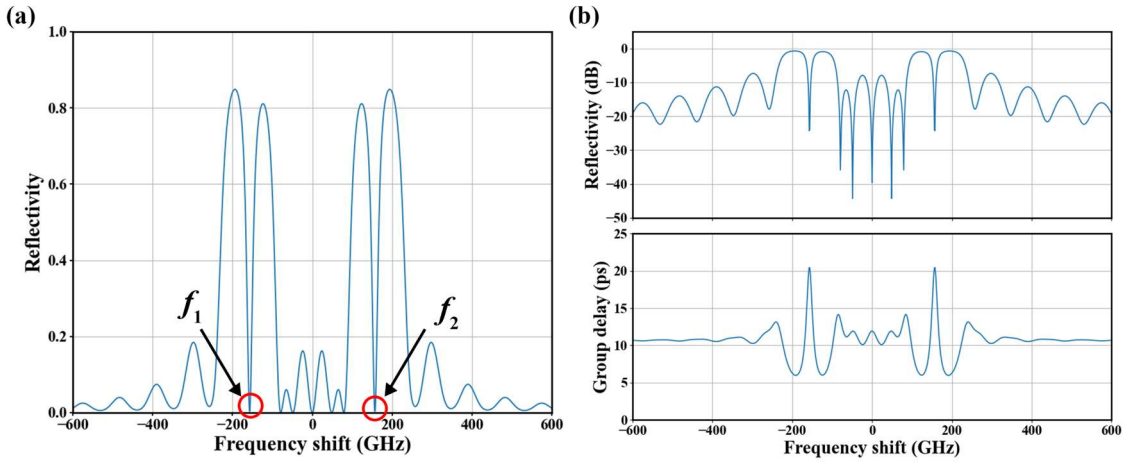

Fig. 2.7 Characteristics of dual wavelength 4PS-SBG with a π-phase shift: **(a)** reflection spectrum, **(b)** reflection spectrum in dB (top right) and group delay (bottom right).

Fig. 2.8 shows the power distribution of the dual-wavelength 4PS-SBG structure. Since the

design incorporates two stopbands, a comparison with the simulation results of the uniform grating in Fig. 2.4(c) reveals that when the two stopbands do not overlap, the reflection spectrum behaves as a linear superposition of individual grating responses. The case where the stopbands significantly overlap will be further discussed in the Moiré grating section (see Chapter 5). However, for THz generation, the required channel frequency spacing is significantly larger than the stopband width.

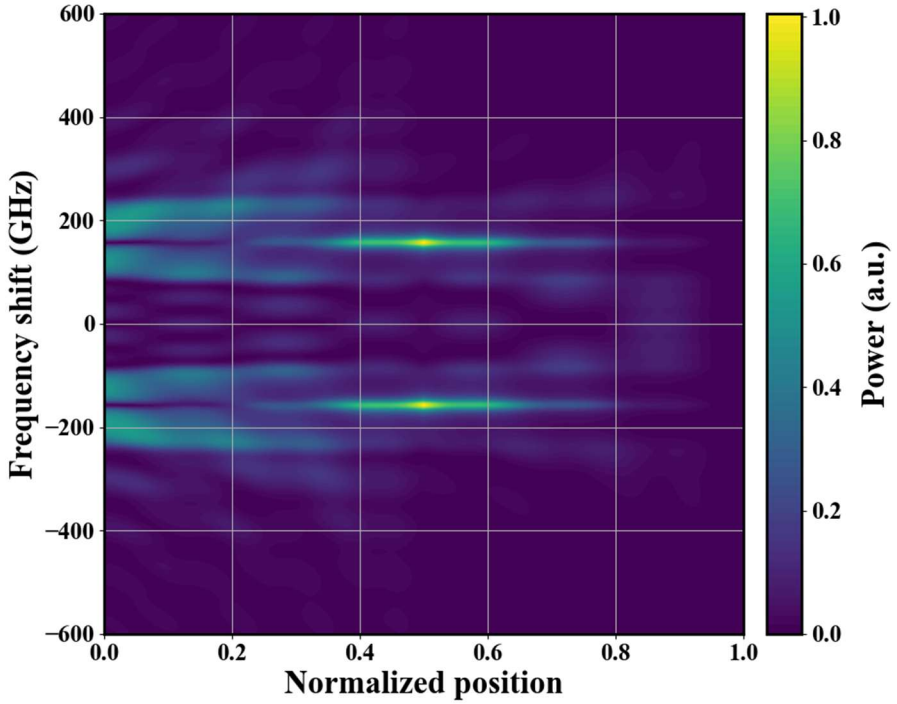

Fig. 2.8 Power distribution of dual wavelength 4PS-SBG structure.

Fig. 2.9 presents the time-domain power distribution of the dual wavelength 4PS-SBG response. The 2D colormap illustrates the evolution of the injected Gaussian pulse inside the grating. The right panel shows the temporal profile of the reflected pulse at the grating input. The results reveal that part of the incident pulse is immediately reflected upon entering the grating, while the remaining energy propagates deeper, experiencing multiple back-reflections. These interactions generate interference patterns along the spatial axis. The reflected pulse profile exhibits temporal broadening and multi-peak splitting, indicating dispersion effects. The delayed reflection components correspond to spectral components that travel further inside the grating before reflection, leading to increased interaction time.

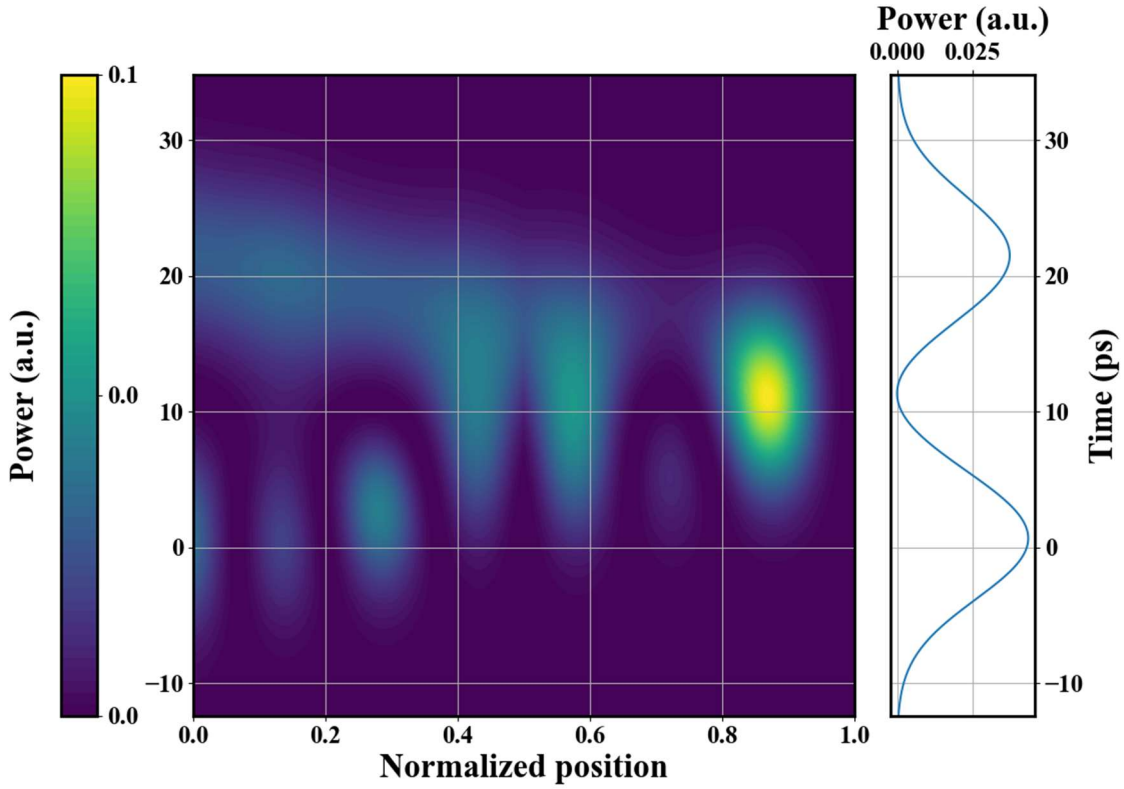

Fig. 2.9 2D map of time domain power distribution (left) and output pulse (right).

2.2 MQW Analysis

2.2.1. Quaternary Semiconductor Alloys

The fundamental materials used for fabricating long-wavelength MQW lasers are typically based on two primary semiconductor alloy systems: $In_{1-x}Ga_xAs_yP_{1-y}$ and $In_{1-x-y}Ga_xAl_yAs$. To determine the material properties of these quaternary compounds, a linear interpolation method is commonly employed. Various physical parameters near the band edges can be approximated using a linear interpolation formula based on the corresponding properties of the relevant binary compounds [103]:

$$\begin{aligned} P(\mathrm{In}_{1-x}\mathrm{Ga}_x\mathrm{As}_y\mathrm{P}_{1-y}) = {} & P(\mathrm{GaAs})\,xy + P(\mathrm{GaP})\,x(1-y) \\ & + P(\mathrm{InAs})\,(1-x)\,y + P(\mathrm{InP})\,(1-x)\,(1-y) \end{aligned} \tag{2.16}$$

$$P(\mathrm{In}_{1-x-y}\mathrm{Ga}_x\mathrm{Al}_y\mathrm{As}) = P(\mathrm{GaAs})\,x + P(\mathrm{AlAs})\,y + P(\mathrm{InAs})\,(1-x-y) \tag{2.17}$$

where P represents a variety of material parameters, including lattice constant (a), elastic stiffness coefficients (C_{11}, C_{12}), deformation potentials (a_c, a_v, b), valence band Luttinger parameters (γ_1, γ_2, γ_3), and the effective masses of electrons and holes. By utilizing the material properties of binary compounds (listed in Table 2.1), an estimation of the physical properties of quaternary compounds can be obtained.

$$\begin{aligned} m_{hh}^{*} &= m_0/(\gamma_1+\overline{\gamma}) \\ m_{lh}^{*} &= m_0/(\gamma_1-\overline{\gamma}) \\ m_{hh\perp}^{*} &= m_0/(\gamma_1-2\overline{\gamma}) \\ m_{lh\perp}^{*} &= m_0/(\gamma_1+2\overline{\gamma}) \\ \overline{\gamma} &= (\gamma_2+\gamma_3)/2 \end{aligned} \tag{2.18}$$

Table 2.1 Parameters for calculation of strain and bandgap energy for the $In_{1-x}Ga_xAs_yP_{1-y}$ and $In_{1-x-y}Ga_xAl_yAs$ material system [103].

Parameter	Symbol(unit)	GaAs	InAs	InP	GaP	AlAs
Lattice Constant	a(Å)	5.6533	6.0584	5.8688	5.4505	5.660
Elastic Stiffness Constant	$C_{11}(10^{11}dyn/cm^2)$	11.879	8.329	10.11	14.05	12.5
Elastic Stiffness Constant	$C_{12}(10^{11}dyn/cm^2)$	5.376	4.526	5.61	6.203	5.34
Hydrostatic deformation potential						
for conduction band	$a_c(eV)$	-7.17	-5.08	-5.04	-7.14	-5.64
for valence band	$a_v(eV)$	1.16	1.00	1.27	1.70	2.47
Shear deformation potential						
for valence band	$b(eV)$	-1.7	-1.8	-1.7	-1.8	-1.5
Valence band parameter	γ_1	6.8	20.4	4.95	4.05	3.45
	γ_2	1.9	8.3	1.65	0.49	0.68
	γ_3	2.73	9.1	2.35	1.25	1.29
Electron effective mass	m_e/m_o	0.067	0.023	0.077	0.25	0.15
Heavy-hole effective mass	m_{hh}/m_o	0.50	0.40	0.60	0.67	0.79

It is important to note that the effective masses listed in Table 2.1 correspond to the (001) growth direction, which is the epitaxial growth axis. The electron and hole effective masses

can also be derived from the Luttinger parameters as shown in Eq. (2.18). The bandgap energy of bulk materials does not strictly follow the linear interpolation rule and is instead better described by an empirical bowing parameter-based formula:

$$\begin{aligned} &\mathrm{In}_{1-x}\mathrm{Ga}_x\mathrm{As}_y\mathrm{P}_{1-y} \\ &E_g(x,\ y) = 1.35 + 0.642x - 1.101y + 0.758x^2 + 0.101y^2 \\ &\qquad - 0.159xy - 0.28x^2y + 0.109xy^2\ \ \mathrm{eV} \end{aligned} \tag{2.19}$$

$$\begin{aligned} &\mathrm{In}_{1-x-y}\mathrm{Ga}_x\mathrm{Al}_y\mathrm{As} \\ &E_g(x,\ y) = 0.36 + 2.093y + 0.629x + 0.577y^2 + 0.436x^2 \\ &\qquad + 1.013xy - 2xy(1-x-y)\ \ \mathrm{eV} \end{aligned} \tag{2.20}$$

Here, I present a bandgap variation diagram of $In_{1-x-y}Ga_xAl_yAs$ as a function of composition, with an InP substrate as shown in Fig. 2.10. Due to the constraint of mole fractions, the diagram is plotted in the form of a ternary phase diagram, where each axis corresponds to the composition fractions of Al, Ga, and In, respectively.

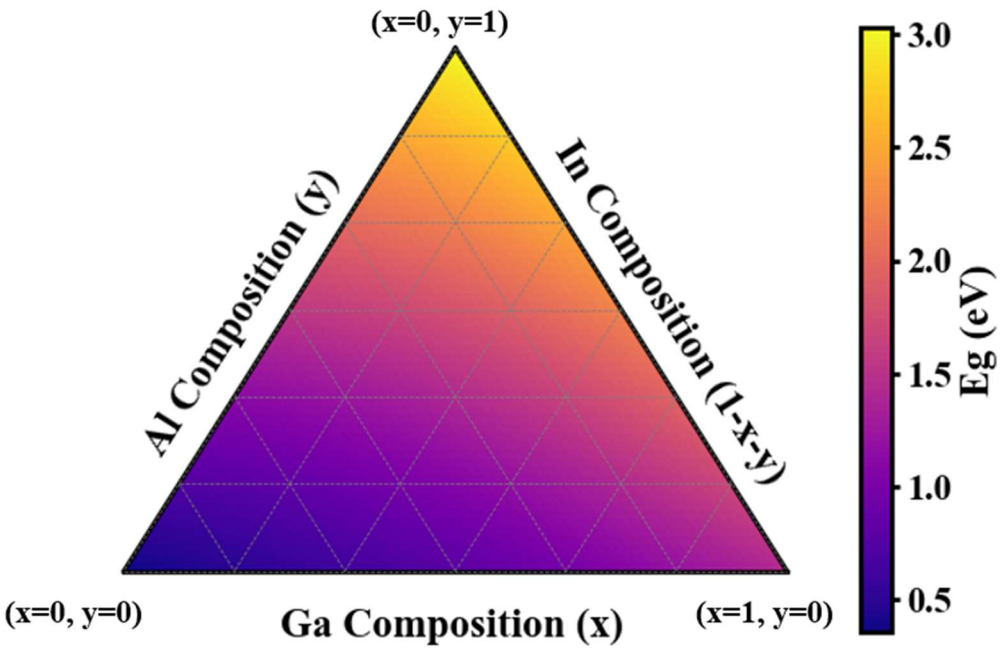

Fig. 2.10 Strained bandgap energy versus Ga (x) and Al (y) mole fractions for the $In_{1-x-y}Ga_xAl_yAs$ material system.

2.2.2 Band Offset and Strain Effects in MQW

In quantum well structures, strain engineering is a critical technique to enhance the performance of optoelectronic devices. Introducing an appropriate level of strain in thin QWs can mitigate the formation of dislocations and defects while simultaneously optimizing key device parameters, such as threshold current and differential gain in MQW lasers. These strain-induced modifications primarily result from alterations in the conduction and valence band energies.

Consider an epitaxial layer grown on a substrate with a lattice constant a_0 which is assumed to be InP and an intrinsic unstrained lattice constant a. When the epitaxial layer thickness remains below the critical thickness, the layer remains elastically strained and fully pseudo-orphic to the substrate, meaning that the in-plane lattice constant is forced to match the substrate value ($a = a_0$). As a result, the strain in the plane and perpendicular direction of the epitaxial growth are:

$$\varepsilon_{\parallel} = \varepsilon_{xx} = \varepsilon_{yy} = \frac{a_0 - a}{a} \tag{2.21}$$

$$\varepsilon_{\perp} = \varepsilon_{zz} = -\frac{2C_{12}}{C_{11}}\varepsilon_{xx} \tag{2.22}$$

The in-plane strain $\varepsilon_{\parallel}$ is typically used as the reference measure of strain in the elastic regime. Tensile strain corresponds to $\varepsilon_{\parallel} > 0$, while compressive strain corresponds to $\varepsilon_{\parallel} < 0$.

Because of strain, the energy of conduction and valence band shift accordingly. For the valence band, the degeneracy between the light hole (*lh*) and heavy hole (*hh*) is lifted, resulting in separation. The shifted energy can be expressed by

$$\delta E_c(x,\ y) = a_c(\varepsilon_{xx} + \varepsilon_{yy} + \varepsilon_{zz}) = 2a_c\left(1 - \frac{C_{12}}{C_{11}}\right)\varepsilon_{\parallel} \tag{2.23}$$

$$\begin{aligned} \delta E_{hh}(x,\ y) &= -P_\varepsilon - Q_\varepsilon \\ \delta E_{lh}(x,\ y) &= -P_\varepsilon + Q_\varepsilon \\ P_\varepsilon &= -2a_v\left(1 - \frac{C_{12}}{C_{11}}\right)\varepsilon_{\parallel} \\ Q_\varepsilon &= -b\left(1 + 2\frac{C_{12}}{C_{11}}\right)\varepsilon_{\parallel} \end{aligned} \tag{2.24}$$

where a_c and a_v are the conduction-band and valence-band hydrostatic deformation potentials, and b is the valence-band shear deformation potential.

Table 2.2 Parameters for calculation of band alignment for the $In_{1-x}Ga_xAs_yP_{1-y}$ and $In_{1-x-y}Ga_xAl_yAs$ material system using Harrison's model [104].

Parameter	**Symbol (unit)**	**GaAs**	**InAs**	**InP**	**GaP**	**AlAs**
Conduction band position	E_c^H (eV)	1.53	0.801	1.35	2.352	2.5255
Valence band position	E_v^H (eV)	0.111	0.441	0.00	-0.388	-0.4245

To fully illustrate the band structure of the QW, the band edge is calculated through Harrison's model. The positions of both the conduction and valence bands are determined by

$$E_c(x,\ y) = E_c^H + \delta E_c(x,\ y) \tag{2.25}$$

$$E_v(x,\ y) = \begin{cases} E_v^H(x,\ y) + \delta E_{hh}(x,\ y) & \text{for compressive strain} \\ E_v^H(x,\ y) + \delta E_{lh}(x,\ y) & \text{for tensile strain} \end{cases} \tag{2.26}$$

where E_c^H and E_v^H are obtained by the linear interpolation of the binary parameters in Table 2.2. It's important to mention that this model only gives the parameter $\Delta E_c/\Delta E_g$ which may be used to determine the alignment between well and barrier materials as expressed by

$$\frac{\Delta E_c}{\Delta E_g} = \frac{E_c^{H,b} - E_c^{H,w}}{(E_v^{H,w} - E_v^{H,b}) + (E_c^{H,b} - E_c^{H,w})} \tag{2.27}$$

2.2.3 Calculation of Energy Levels

The electronic band structure near the center of the Brillouin zone in direct-bandgap semiconductor materials can be well described using the $k \cdot p$ perturbation theory [105]. For most direct-bandgap III-V semiconductors, the conduction band characteristics can be accurately modeled using the following approach.

$$H^c(\mathbf{k}) = \left(\frac{\hbar^2}{2}\right)\left(\frac{k_x^2 + k_y^2}{m_{n,t}} + \frac{k_z^2}{m_{n,z}}\right) + V_\varepsilon(z) + a_c \mathrm{Tr}\left(\overline{\overline{\varepsilon}}\right) \tag{2.28}$$

where the wave vector $\mathbf{k}$ is interpreted as a differential operator $-i\nabla$. $m_{n,t}$ and $m_{n,z}$ are the electron effective masses perpendicular (t) and parallel (z) to the growth direction, respectively, $V_\varepsilon(z)$ is the potential energy of the unstrained conduction band edge, and $\overline{\overline{\varepsilon}}$ is the symmetric strain tensor. By considering the anisotropy of the conduction band while neglecting non-parabolicity effects [106], the conduction band energy levels $E_n^c(k)$ can be obtained by solving the corresponding Schrödinger equation

$$H^{c}\phi_{n}(z;k_{t}) = E_{n}^{c}(k_{t})\phi_{n}(z;k_{t}) \tag{2.29}$$

where ϕ_n is the n^{th} envelope function of conduction sub band.

According to the Luttinger-Kohn and Bir-Pikus theories [107], the valence band structure of a strained semiconductor consists of the heavy hole, light hole, and spin-orbit split-off (*so*) bands. These can be represented by a 6×6 Hamiltonian matrix. Under the axial approximation [108], this Hamiltonian can be block-diagonalized into a simplified form:

$$H^{v}(\mathbf{k}) = \begin{bmatrix} H_{3\times3}^{U}(\mathbf{k}) & 0 \\ 0 & H_{3\times3}^{L}(\mathbf{k}) \end{bmatrix} \tag{2.30}$$

$$H_{3\times3}^{\sigma} = -\begin{bmatrix} \mathcal{P}+\mathcal{Q}-V_h(z) & R_k \mp iS_k & \sqrt{2}\,R_k \pm \dfrac{i}{\sqrt{2}}S_k \\ R_k \pm iS_k & \mathcal{P}-\mathcal{Q}-V_h(z) & \sqrt{2}\mathcal{Q} \pm i\sqrt{\dfrac{3}{2}}S_k \\ \sqrt{2}\,R_k \mp \dfrac{i}{\sqrt{2}}S_k & \sqrt{2}\mathcal{Q} \mp i\sqrt{\dfrac{3}{2}}S_k & \mathcal{P}+\Delta(z)-V_h(z) \end{bmatrix} \tag{2.31}$$

where σ denotes either the upper (U) or lower (L) blocks, determining the sign conventions in the matrix elements. And where

$$
\begin{aligned}
\mathcal{P} &= P_k + P_\epsilon \\
\mathcal{Q} &= Q_k + Q_\epsilon \\
P_k &= \left(\frac{\hbar^2}{2m_0}\right)\gamma_1 (k_t{}^2 + k_z{}^2) \\
Q_k &= \left(\frac{\hbar^2}{2m_0}\right)\gamma_2 (k_t{}^2 - 2k_z{}^2) \\
R_k &= \left(\frac{\hbar^2}{2m_0}\right)\sqrt{3}\left(\frac{\gamma_2 + \gamma_3}{2}\right)k_t{}^2 \\
S_k &= \left(\frac{\hbar^2}{2m_0}\right)2\sqrt{3}\,\gamma_3 k_t k_z \\
P_\epsilon &= -a_v(\epsilon_{xx} + \epsilon_{yy} + \epsilon_{zz}) \\
Q_\epsilon &= -\frac{b}{2}(\epsilon_{xx} + \epsilon_{yy} - 2\epsilon_{zz})
\end{aligned}
\tag{2.32}
$$

In this representation, $V_h(z)$ is the unstrained valence band edge, and the spin-orbit splitting energy is denoted as $\Delta(z)$. The in-plane wave vector is given by $k_t=k_x{}^2+k_y{}^2$, while the out-of-plane wave vector is expressed as $k_z=-i\partial/\partial z$. The hole wavefunction can be expressed as:

$$
\Psi_{m,k_t}^{v\eta} = \frac{e^{ik_t\rho}}{\sqrt{A}} \sum_{i=hh,lh,so} g_{m,i}^{\sigma}(z;k\,)|u_i^{\sigma}\rangle \tag{2.33}
$$

where A represents the quantum well cross-sectional area, $\rho = \sqrt{x^2 + y^2}$. The valence band structure can then be determined by solving the Schrödinger equation:

$$
\sum_{j=hh,lh,so} H_{3\times 3,ij}^{\sigma}\left(k_z = -i\frac{\partial}{\partial z}\right) g_{m,j}^{\sigma}(z;k_t) = E_{\sigma,m}^{v}(k_t)\, g_{m,j}^{\sigma}(z;k_t) \tag{2.34}
$$

The Schrödinger equations governing the conduction and valence band energy levels are solved using the finite difference method. All differential operators appearing in Eq. (2.29) and (2.34) can be expressed in the form $A(z)\partial^2/\partial z^2$ or $B(z)\partial^2/\partial z^2$, where A and B represent position-dependent inverse effective mass parameters for the well and barrier regions. The

elements of the Hamiltonian and the boundary conditions [109] are rigorously preserved by employing the following finite difference schemes:

$$\begin{aligned} A(z)\frac{\partial^2 g}{\partial z^2}\bigg|_{z=z_i} &\to \frac{\partial}{\partial z}\left(A(z)\frac{\partial g}{\partial z}\right)\bigg|_{z=z_i} \\ &\approx \frac{A(z_{i+1})+A(z_i)}{2(\Delta z)^2}g(z_{i+1}) \\ &- \frac{A(z_{i-1})+2A(z_i)+A(z_{i+1})}{2(\Delta z)^2}g(z_i) \\ &+ \frac{A(z_i)+A(z_{i-1})}{2(\Delta z)^2}g(z_{i-1}) \end{aligned} \tag{2.35}$$

$$\begin{aligned} B(z)\frac{\partial g}{\partial z}\bigg|_{z=z_i} &\to \frac{1}{2}\left(B(z)\frac{\partial g}{\partial z}+\frac{\partial (Bg)}{\partial z}\right)\bigg|_{z=z_i} \\ &\approx \frac{B(z_{i+1})+B(z_i)}{4\Delta z}g(z_{i+1}) \\ &- \frac{B(z_i)+B(z_{i-1})}{4\Delta z}g(z_{i-1}) \end{aligned} \tag{2.36}$$

where $\Delta z = z_{i+1} - z_i = z_i - z_{i-1}$.

2.2.4 Calculation of gain spectrum

The local gain spectrum corresponding to electronic transitions from the *i*-th subband in the conduction band to the *j*-th subband in the valence band can be expressed as

$$g_{ij}(\hbar\omega) = g_0(\hbar\omega)\,|M_{v,ij}|^2\,\rho_{r,v,ij}(f_{c,i}-f_{v,j}) \tag{2.37}$$

$$g_0(\hbar\omega) = \frac{\pi\hbar e^2}{m_0^2\varepsilon_0 c n_{eff}\hbar\omega} \tag{2.38}$$

$$|M_{v,ij}|^2 = |M_b|^2 M_0 |M_{cv}|^2 \tag{2.39}$$

where $g_0(\hbar\omega)$ represents the gain coefficient, $|M_{v,ij}|^2$ denotes the momentum matrix element associated with the transition between the conduction i^{th} subband and the valence j^{th} subband, and $\rho_{r,v,j}$ corresponds to the joint density of states. The terms $f_{c,i}$ and $f_{v,j}$ represent the Fermi distribution functions for electrons in the conduction and valence bands, respectively. The parameters $|M_b|^2$, $|M_{cv}|^2$, and M_0 correspond to the average momentum matrix element for dipole transitions in bulk materials, the conduction-valence band overlap integral, and the polarization factor.

$$|M_b|^2 = \frac{m_0{}^2 E_{g0}(E_{g0}+\Delta)}{12 m_e (E_{g0}+2\Delta/3)} \tag{2.40}$$

Here, m_0 and m_e denote the free electron mass and the effective mass of electrons in the conduction band, while E_{g0} and Δ correspond to the bandgap energy and the spin-orbit splitting energy of the bulk quantum well material. The overlap integral term $|M_{cv}|^2$ can be obtained from the subband wavefunctions computed previously using the finite difference method.

For bulk materials, the polarization factor is given by $M_0 = 1$. However, in quantum well structures, the polarization factor varies depending on the kinetic energy of light and heavy holes along different in-plane directions:

$$\begin{aligned} |M_0|_{c,hh} &= \frac{3+3\cos(\theta)}{4} \\ |M_0|_{c,lh} &= \frac{5-3\cos(\theta)}{4} \end{aligned} \quad \text{for TE} \tag{2.41}$$

$$\begin{aligned} |M_0|_{c,hh} &= \frac{3-3\cos(\theta)}{2} \\ |M_0|_{c,lh} &= \frac{1+3\cos(\theta)}{2} \end{aligned} \quad \text{for TM} \tag{2.42}$$

$$\cos(\theta) = \begin{cases} E_{ij}^0/E & \text{for } E > E_{ij}^0 \\ 1 & \text{for } E \leqslant E_{ij}^0 \end{cases} \tag{2.43}$$

The joint density of states $\rho_{r,v,ij}$ is expressed as:

$$\rho_{r,v,ij} = \frac{m_{r,v}}{\pi\hbar^2 L_z} h(\hbar\omega - E_{ij}^0) \tag{2.44}$$

$$h(\hbar\omega - E_{ij}^0) = \begin{cases} 1 & for \ \ \hbar\omega \geqslant E_{ij}^0 \\ 0 & for \ \ \hbar\omega < E_{ij}^0 \end{cases} \tag{2.45}$$

$$\frac{1}{m_{r,v}} = \frac{1}{m_{c,\parallel}} + \frac{1}{m_{v,\parallel}} \tag{2.46}$$

For gain spectrum calculations, the in-plane effective masses must be applied, which can be determined using Eq. (2.18). The Fermi distribution functions are given by:

$$f_{c,i} = 1 + \exp\left(\frac{E_i^0 + \frac{m_{r,v}}{m_c}(E - E_{ij}^0) - E_{fn}}{kT}\right) \tag{2.47}$$

$$f_{v,j} = 1 + \exp\left(\frac{E_j^0 + \frac{m_{r,v}}{m_v}(E - E_{i,j}^0) - E_{fp}}{kT}\right) \tag{2.48}$$

where E_{fn} and E_{fp} represent the quasi-Fermi levels of the conduction and valence bands, which are obtained from the electron and hole density:

$$n = \sum_i \rho_i kT \ln\left[1 + \exp\left(\frac{E_{fn} - E_i}{kT}\right)\right] \tag{2.49}$$

$$p = \sum_j \rho_j kT \ln\left[1 + \exp\left(\frac{E_{fp} - E_j}{kT}\right)\right] \tag{2.50}$$

In this study, the strain-compensated MQW core consists of five 6 nm $Al_{0.07}Ga_{0.22}In_{0.71}As$ quantum wells with a +1.2% compressive strain, separated by six 10 nm $Al_{0.224}Ga_{0.28}In_{0.49}As$ barriers with a -0.3% tensile strain. Fig. 2.11 present the material gain spectra for both transverse electric (TE) and transverse magnetic (TM) modes at 300 K under varying carrier densities. The simulation employs a Gaussian lineshape function to account for the simplest non-Markovian quantum kinetics, with an intraband relaxation time set to an empirical constant of 40 fs. As shown in Fig. 2.11(a) the TE mode gain spectrum increases with carrier density, exhibiting a broad gain bandwidth with a peak centered around 1560 nm. In contrast, the TM mode gain spectrum, shown in Fig. 2.11(b), remains close to zero when carrier density is less than 1.5×10^{18} cm^{-3}. Even at higher carrier densities, the maximum material gain for the TM mode remains below 150 cm^{-1}, which is significantly lower than the TE mode gain under comparable conditions. This indicates that the material system is strongly biased toward TE-polarized lasing, with TM mode emission effectively suppressed. Notably, some kinks appear in the TM gain spectrum, which may be attributed to numerical artifacts in the band structure solver or discontinuities in subband transitions under low optical confinement and gain levels.

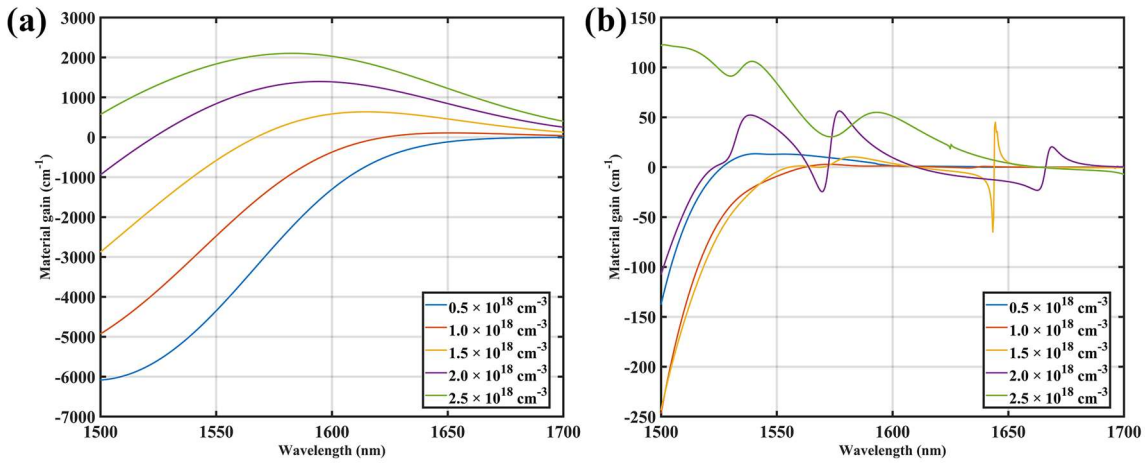

Fig. 2.11 Material gain of the 6 nm $Al_{0.07}Ga_{0.22}In_{0.71}As$ quantum well and 10 nm $Al_{0.224}Ga_{0.28}In_{0.49}As$ quantum barrier structure for **(a)** TE mode, and **(b)** TM mode.

2.3 Waveguide and Optical Mode

For a DFB laser incorporating a compressively strained QW structure, lasing occurs exclusively in the TE modes [110]. The number of supported TE modes is primarily governed by the ridge waveguide width. When the ridge is sufficiently narrow, only the fundamental TE mode is guided, while higher-order modes are effectively suppressed due to their increased propagation losses and reduced confinement, ensuring single-mode operation.

To analyze the optical modes, simulations were conducted using Lumerical MODE Solutions, focusing on ridge waveguides etched to a depth of 1920 nm. This software employs the finite difference eigenmode (FDE) solver to compute the mode field profile and effective index by solving Maxwell's equations on a cross-sectional mesh of the waveguide structure. The relationship between the waveguide modal effective index and ridge width for the TE_{00}, TE_{01}, TE_{02} modes was simulated at a wavelength of 1550 nm, as depicted in Fig. 2.12.

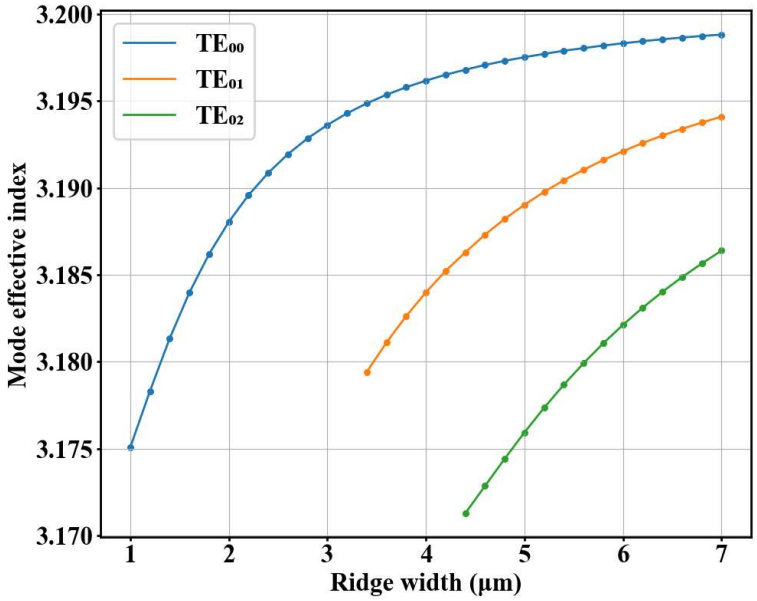

Fig. 2.12 Mode effective index versus ridge width for TE_{00}, TE_{01}, and TE_{02} modes at the wavelength of 1550 nm.

For a given TE mode, the modal effective index increases with increasing ridge width. However, for the same ridge width, higher-order modes exhibit a lower waveguide modal effective index. The results indicate that only the fundamental TE mode is supported when the ridge width is 3.2 μm or less. Considering fabrication tolerances, a ridge width of 2.5 μm was selected for the semiconductor lasers in this study. Experimental observations confirmed that only the fundamental TE mode was lased, while higher-order TE modes were not supported due to their significantly higher propagation losses compared to the fundamental mode. Fig. 2.13 shows the fundamental mode TE_{00} electric field distribution of a 2.5 μm-wide ridge waveguide, obtained using FDE simulation. Due to the higher refractive index in the quantum well region, the optical mode is tightly confined around the active region, ensuring effective overlap between the optical field and the gain medium.

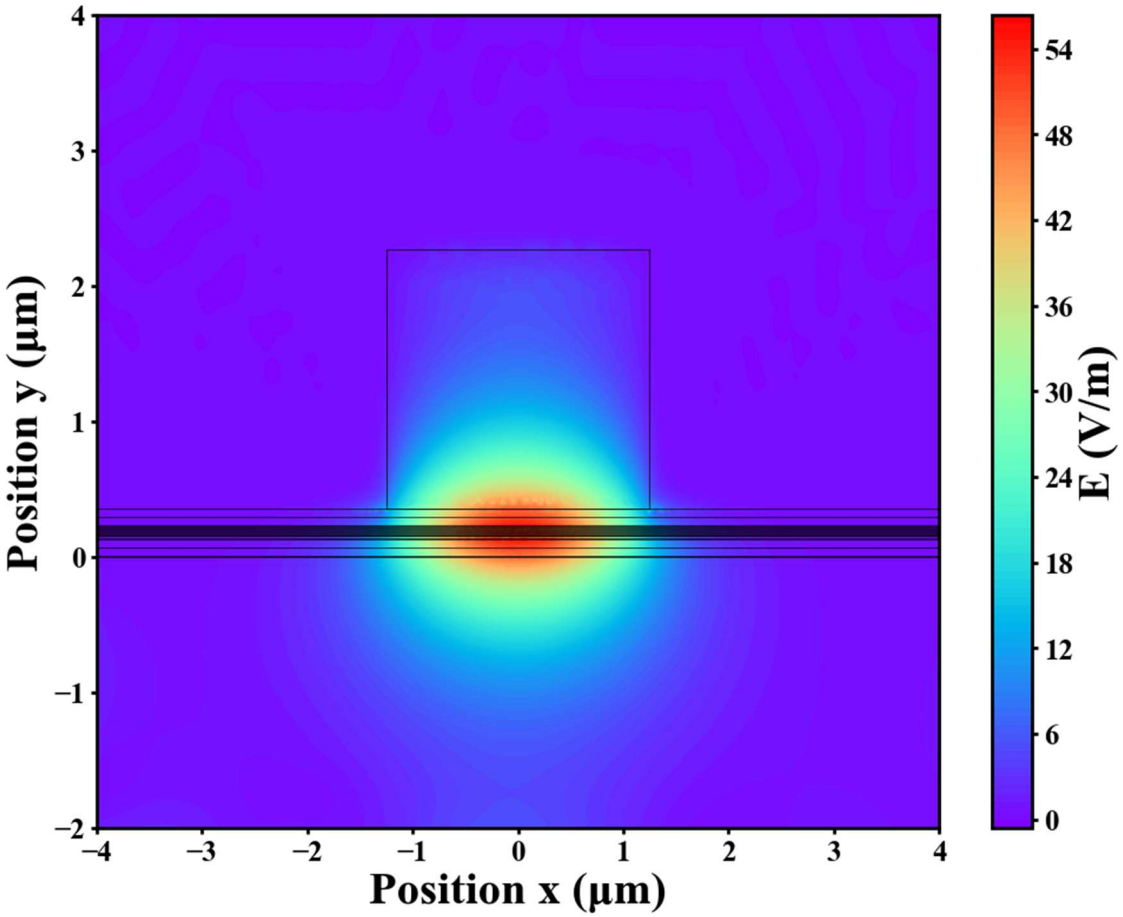

Fig. 2.13 Simulated fundamental optical mode (TE_{00}) for the 2.5 μm wide, 1920 nm deep ridge waveguide.

2.4 Chapter Summary

This chapter presented the theoretical foundations and design methodology for DFB and DBR semiconductor lasers. The design phase was addressed from three perspectives: Bragg grating analysis, MQW analysis, and optical mode analysis.

The discussion began with the Bragg condition and CMT, which form the theoretical basis for modeling periodic grating structures. The TMM was then introduced in detail and demonstrated to be a powerful tool for simulating various types of Bragg gratings. Simulation results for UBGs were shown, followed by the theoretical introduction of SBGs,

where higher-order reflection peaks emerge due to the periodic sampling function. Several methods for constructing DWLs using SBG structures were discussed.

The MQW analysis section provided a simple and efficient framework to investigate the material gain properties of quantum well structures. Two quaternary material systems, InGaAsP and InGaAlAs, were introduced, followed by a discussion on the effects of strain on bandgap and band offsets. Based on these models, quantum confinement energy levels were calculated, and the material gain spectrum for the InGaAlAs QW used in this thesis was obtained.

Finally, waveguide and optical mode analysis were performed using the FDE method. Simulations of ridge waveguides with varying widths were carried out to identify the optimal waveguide geometry and ensure effective single-mode confinement.

Chapter 3 Epilayer and Fabrication

The fabrication of lasers based on sidewall grating structure follows a well-defined sequence of processing steps, each carefully designed to ensure precise pattern transfer and high device performance. Since different devices described in this work are based on various ridge waveguide geometries and grating profiles, the processing sequence remains consistent. To provide a clear and step-by-step overview of the fabrication process, a comprehensive fabrication flow table is included in Appendix I, which summarizes the key stages involved in device realization. This table serves as a central reference for the detailed discussions that follow.

In the subsequent sections, I will first introduce the epitaxial layer structures used in this work, followed by a breakdown of the critical nanofabrication steps employed in producing the devices.

3.1 Epilayer Material and Structure

The III-V semiconductor lasers in this study employ commercial MQW epitaxial structures (IQE Company) engineered for 1550 nm emissions. Our DFB implementation features a regrowth-free ridge waveguide design with sidewall-integrated feedback gratings adjacent to the active region, balancing fabrication practicality with performance requirements. While this configuration exhibits marginally higher threshold currents due to lateral current spreading in wide waveguides, it achieves essential output power levels while eliminating regrowth-induced oxidation and contamination issues inherent to conventional DFB processes.

Material selection was critically guided by carrier confinement and thermal stability considerations. The AlGaInAs/InP heterostructure was preferred over InGaAsP/InP alternatives based on its superior electron confinement capability ($\Delta Ec/\Delta Eg = 0.72$ vs. 0.40),

which suppresses carrier leakage and enhances temperature-dependent performance. Strict lattice-matching conditions ($\Delta a/a < 5\times10^{-4}$) were maintained throughout epitaxial growth via metalorganic vapor phase epitaxy (MOVPE) on sulfur-doped InP substrates [111], [112], [113], [114].

Fig. 3.1 presents a complete epitaxial architecture. The structure commences with an 800 nm n-InP buffer layer (Si-doped, 2×10^{18} cm^{-3}), establishing the crystalline foundation, followed by systematically engineered confinement and active regions. A graded-index separate confinement heterostructure (GRINSCH) configuration employs dual 60 nm $Al_xGa_yIn_{1-x-y}As$ layers with precisely controlled aluminum composition gradients linearly decreasing from x=0.423 to 0.338 in the lower layer and reversing this gradient in the upper counterpart. This strategic grading creates a parabolic potential profile that synergistically enhances both carrier confinement and optical mode overlap. The strain-compensated MQW core incorporates five 6 nm $Al_{0.07}Ga_{0.22}In_{0.71}As$ quantum wells (+1.2% compressive strain) separated by six 10 nm $Al_{0.224}Ga_{0.28}In_{0.49}As$ barriers (-0.3% tensile strain), achieving net strain compensation while maintaining lattice integrity ($\Delta a/a < 0.03\%$ in non-active regions). Doping architecture implements Zn/Si modulation doping (5×10^{17} cm^{-3}) in p/n-type layers respectively, culminating in a heavily doped p^+-InGaAs ohmic contact layer (1.5×10^{19} cm^{-3}) to minimize series resistance.

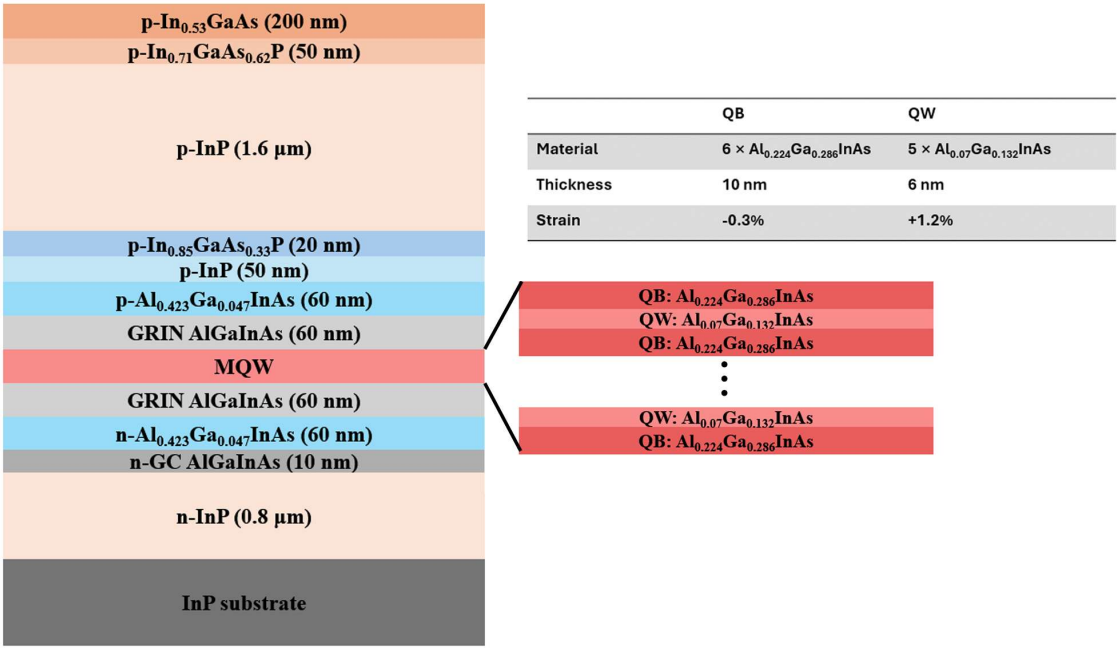

Fig. 3.1 Schematic of the epitaxial structures.

3.2 Mask Design and Sample Preparation

The fabrication mask design was carried out using multiple software tools, including MATLAB, CleWin, and L-Edit. Complex patterns were generated in MATLAB and transferred to GDSII format through the CleWin MATLAB API. These grating structures were subsequently integrated into the L-Edit design file. Fig. 3.2 presents the complete layout of the EBL mask design created using L-Edit. The use of hierarchical layers allows independent control over different lithography levels within the design. In total, seven layers were utilized in the design process, including “Substrate”, “Marker”, “Isolation”, “ProtectLayer”, “Grating”, “OpenWindow”, and “Metal”. Among them, the “Substrate” layer defines the physical boundary of the sample area (11 mm × 12 mm) and serves as a visual reference. The “ProtectLayer” and “Grating” layers are written during the same EBL exposure step, but they are separated in the design due to the distinct exposure doses required for each. Therefore, across the full fabrication process, a total of five EBL steps are employed.

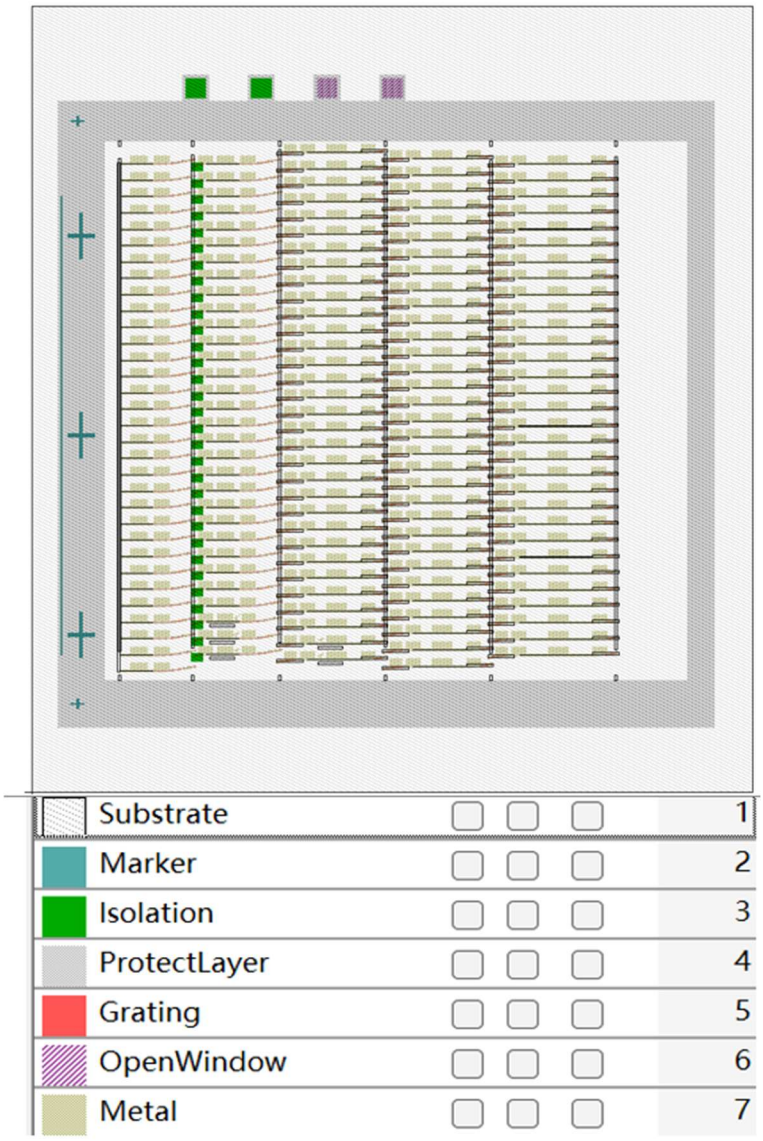

Fig. 3.2 EBL mask design in L-Edit.

In the chip layout, devices are organized into multiple bars, each corresponding to a different cavity length. The bars are spatially separated and accompanied by cleaving markers, which facilitate accurate cleavage of the sample after fabrication is completed.

For device fabrication, prior to processing, the wafer was cleaved into smaller samples to accommodate the fabrication of different devices. A diamond scribe was used for precise cleaving, yielding sample dimensions of approximately 11 mm × 12 mm. Notably, samples obtained near the wafer edge exhibited a curved upper boundary due to the inherent wafer

curvature. To maintain sample integrity during handling and storage, each cleaved piece was placed in individual plastic containers throughout the fabrication process. Fig. 3.3 shows a cleaved sample for fabrication.

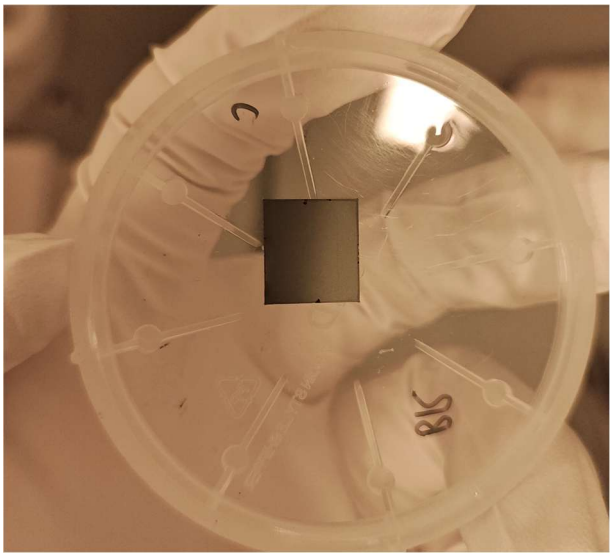

Fig. 3.3 Sample cleaved with dimensions 11 mm ×12 mm.

The cleaved sample is then cleaned under these procedures. The sample underwent a sequential solvent cleaning procedure to ensure surface integrity prior to device fabrication. Initially, the substrate was immersed and rinsed in reagent-grade acetone (CH_3COCH_3) for 3 minutes. This was followed by subsequent rinsing in analytical-grade isopropyl alcohol (IPA, C_3H_8O) and reverse osmosis (RO) water with each immersion step lasting 3 minutes. To enhance contaminant removal efficacy, ultrasonic agitation could be optionally implemented. Following the aqueous cleaning phase, residual liquid was removed through forced nitrogen drying to prevent watermark formation.

3.3 Electron Beam Lithography

EBL is a high-resolution patterning technique that utilizes a focused beam of accelerated electrons to directly write nanoscale features into an electron-sensitive resist. The system consists of an electron gun, electromagnetic lenses, beam deflection coils, and a high-

precision stage, all controlled by CAD software. During exposure, the electron beam is scanned across the resist-coated sample according to a predefined pattern, inducing chemical changes in the resist via electron scattering. Subsequent development reveals the pattern, which is then transferred to the underlying material through etching or lift-off processes. Due to its serial writing nature, EBL offers unparalleled flexibility and sub-10 nm resolution, making it ideal for defining gratings and other critical nanostructures required in DFB/DBR laser fabrication. The EBL system used in this work is a Raith EBPG 5200 operating at 100 kV. It features a minimum beam spot size of 3 nm and supports feature sizes well below 10 nm. The system is equipped with a 200 mm XY stage and a 10 mm Z stage, offering high stability and precision, with typical stitching errors around 20 nm [115]. The machine uses a vector scan system which means the beam is only deflected to the areas where it needs to expose part of the pattern and never to areas where there is nothing to expose.

The advantages of EBL are resolution, placement and flexibility. The machine allows you to access length scales not practically available with any other lithography technique. It also allows you to overlay different levels of lithography very accurately (<20 nm mean + 3σ). The pattern is defined only as a software mask, which means it is very easy to change designs without having to make a new mask. Whereas the disadvantage is that it is slower compared to photolithography performed with a mask aligner or a stepper. It is also typically slower than photolithography performed with a laser writer. This is because EBL is inherently a serial process; with the pattern having to be exposed 1 pixel at a time, and the size of the pixel is much smaller than on a laser writer, so there are many more pixels in EBL.

When a pattern extends beyond a single block, stitching is required to align adjacent writing fields. Ideally, with proper system calibration, the stitched fields align seamlessly. The stitching accuracy of the system is typically characterized by mean + 3σ values, where the system achieves an alignment precision of approximately 18 nm. The system achieves a minimum electron beam spot size of 4 nm and a pattern resolution down to 0.5 nm, with a writeable field size of 0.5 mm × 0.5 mm. However, given that certain device structures, such

as laser cavities, exceed this field size (e.g., 1 mm cavity length), stitching errors between adjacent exposure fields can arise. These errors introduce minor phase shifts in the gratings but have negligible impact on the single-mode operation of DFB lasers, given the relatively large grating periods (~243 nm).

Although holographic lithography provides an alternative approach to fabricating gratings without stitching errors, it is limited by the inability to define varying grating periods at different locations on the sample. EBL, in contrast, allows precise control over grating period variations, making it the preferred technique for this study.

3.3.1 Writing frequency

The writing frequency refers to the rate at which the electron beam steps from one pixel to the next while patterning the resist. It is a critical parameter that influences both writing speed and pattern fidelity, and it typically ranges from 0.5 kHz up to 125 MHz. Higher frequencies result in faster exposure, improving throughput. The writing frequency is determined by the measured beam current, the beam step size (BSS) and the dose required to fully expose the resist, as expressed:

$$F[MHz] = 0.1 \times \frac{Current[nA]}{dose\left[\frac{\mu C}{cm^2}\right] \times bss^2[\mu m]} \tag{3.1}$$

The optimal exposure dose is process-dependent and is typically determined experimentally through exposure tests. Once the required dose and the minimum feature size are established, the writing frequency can be calculated accordingly. It is important to ensure that all input values correspond to the appropriate units.

3.3.2 Proximity Effect Correction

The exposure dose is a critical parameter in electron beam lithography, representing the charge per unit area required to expose the resist, typically measured in μC/cm². Achieving optimal exposure does necessitate careful consideration of electron scattering effects within the material, as scattered electrons can lead to unintended exposure beyond the intended pattern. To compensate for these effects, a process known as proximity effect correction (PEC) is applied, where the exposure dose distribution is modified to ensure uniform pattern fidelity. In this study, Beamer, a commercial software tool, was employed for proximity correction calculations.

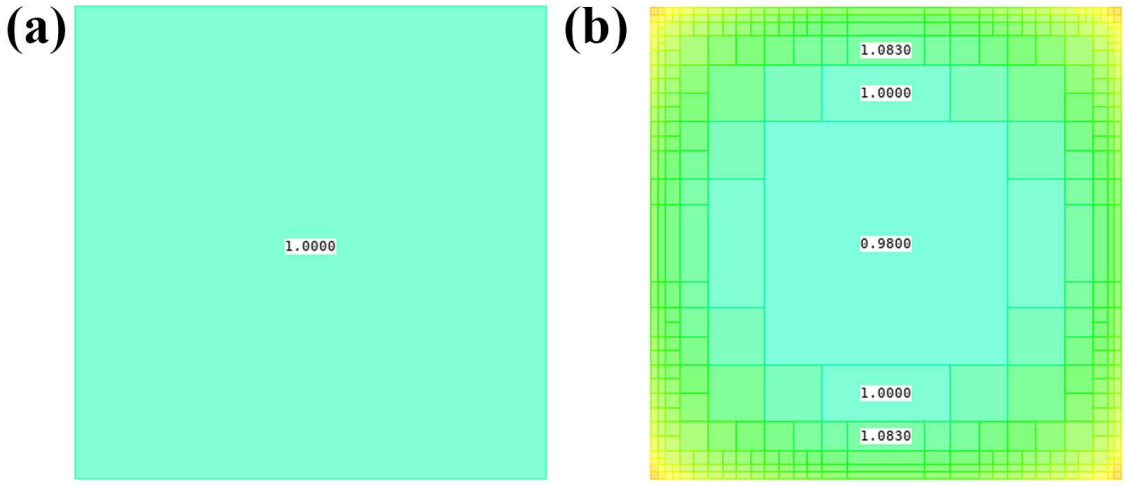

Fig. 3.4 The exposure does distribution **(a)** before and **(b)** after PEC of a 20 μm square.

As illustrated in Fig. 3.4, the exposure does distribution for a 20 μm square undergoes significant adjustments after correction. Initially, before proximity correction, the exposure dose remains uniform across the entire region shown in Fig. 3.3(a). However, after correction (Fig. 3.3(b)), the square is segmented into numerous smaller rectangles, each assigned a different dose value. In the central region, the exposure dose is reduced, whereas at the edges, it is increased. This adjustment accounts for the fact that central areas receive a higher proportion of scattered electrons compared to edge regions. By redistributing the exposure

dose accordingly, proximity correction enhances the accuracy of the pattern transfer, minimizing distortions and ensuring well-defined feature profiles.

3.4 Aligned Marker Definition

Aligned markers were initially defined to facilitate multi-step lithography, ensuring precise alignment between subsequent lithography stages. Well-defined markers are crucial, especially for EBL, where the alignment process is automated and relies on markers with high contrast. Both etched markers and metalized markers are viable options for EBL. In my study, metalized markers were selected to enhance contrast. The fabrication process was carried out in the James Watt Nanofabrication Center (JWNC) at the University of Glasgow.

3.4.1 Lift-off

The lift-off process is widely used in semiconductor laser fabrication for patterning metal contacts and gratings. It allows precise patterning without damaging the underlying semiconductor. This method is particularly advantageous when etching is not feasible due to substrate or material constraints. I utilized a bilayer polymethyl methacrylate (PMMA) resist structure for marker fabrication [116]. The bilayer resist system improves the process by creating an undercut profile, ensuring smooth lift-off, preventing metal re-deposition and edge defects, and enabling high-resolution patterning with EBL. Compared to a single-layer resist, the bilayer lift-off provides a more reliable and cleaner pattern definition. As depicted in Fig. 3.5, the first resist layer comprised 15% PMMA dissolved in Anisole with a molecular weight of 200K, applied via spin coating to achieve a thickness of around 1.26 μm. The second resist layer consisted of 4% PMMA dissolved in Ethyl Lactate with a molecular weight of 600K, with a thickness of around 220 nm. The higher molecular weight chain segments “freeze-out” more rapidly than the lower molecular weight segments that would be found in the exposed regions. After each spin coating step, the resist was baked on a hot plate at 180°C for 4 mins to remove the solvents in the resist. The development was

conducted to reveal the pattern using a developer comprising a mixture of methyl isobutyl ketone (MIBK) and IPA, with the ratio according to the exposure dose, resist thickness, and feature size [117]. For this process, the sample underwent immersion in MIBK: IPA (1:2.5) for 35 seconds at 23°C, followed by rinsing in IPA at room temperature for 30 seconds. For better adhesion in the metal deposition, the sample was cleaned by O_2 plasma using the plasma system Asher Yield YES G-1000 to remove the resist residue on the developed surface. The 20 sccm O_2 flow with RF power of 200 W can have an etching rate of around 10 nm/min. The sample was cleaned by this recipe for 2 mins before metal deposition.

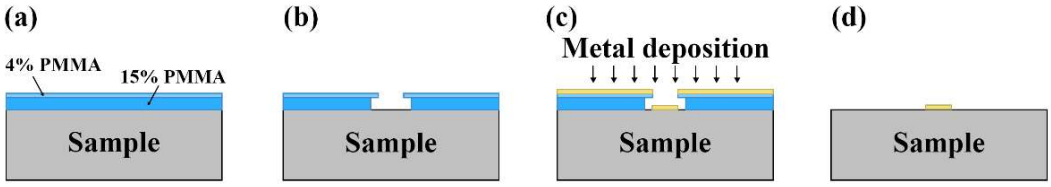

Fig. 3.5 Process of lift-off.

For the metal stack deposition, I used NiCr and Au layers with thicknesses of 33 nm and 100 nm, respectively. Initially, both NiCr and Ti were considered as potential adhesion layers. However, considering the fabrication process involving mask cleaning of HSQ using HF, it was observed that Ti would react during this step, whereas NiCr would remain stable. Therefore, NiCr was selected as the material for marker deposition. Additionally, the top layer of gold serves to prevent oxidation and provide sufficient contrast in EBL alignment recognition. Finally, a 50 ℃ water bath using acetone for about 1h is enough to remove the remaining PMMA.

3.3.2 Fabricated Marker

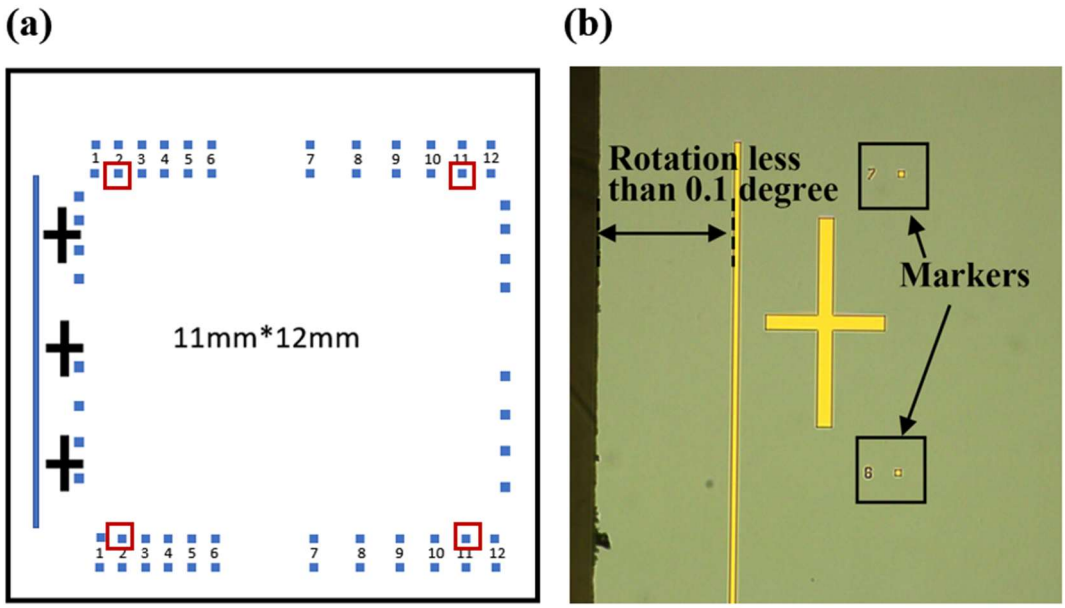

Fig. 3.6 (a) Aligned marker design. **(b)** Aligned marker definition after deposition.

Fig. 3.6(a) illustrates the alignment marker configuration of a 11 × 12 mm sample for EBL. The coarse alignment was performed using fiducial crosses featuring 50 μm-wide arms, while precision alignment employed dual redundant marker arrays enabling precise rotational and translational alignment. A primary set of four vernier markers was supplemented with secondary markers，providing backup alignment references in case of pattern recognition failures. The left-half markers (No.1-6) maintain uniform 500 μm spacing for baseline coordinate calibration, whereas the right-half markers (No.7-12) employ non-uniform spacing (500-900 μm) to enhance pattern recognition robustness through spatial differentiation. This hybrid distribution strategy achieves <50 nm overlay accuracy by compensating for both systematic and random stage errors. The fabricated marker is shown in 错误!未找到引用源。(b). The marker is carefully checked under the microscope. The aligning marker should be oriented with no more than 0.1-degree rotation relative to the natural cleavage plane of the substrate to minimize cleaving errors. This precision is crucial because the sample must be cleaved into bars for further processing. When the aligning

marker has a significant rotation misalignment with respect to natural (100) planes, the sample will cleave along the natural crystalline direction rather than the designed alignment. This will lead to an inconsistent positioning of device edges after cleaving causing phase variation at the laser facets.

3.5 Electrical Isolation Etch

3.5.1 ICP Dry Etch

Dry etching is a fundamental technique in semiconductor fabrication, primarily utilizing plasma-enhanced processes to achieve high-resolution material removal. Compared to wet etching, which relies on chemical solutions, dry etching offers superior anisotropy and fine feature control, making it indispensable for modern nanofabrication. Among various dry etching methods, plasma etching plays a central role by employing high-energy plasma species to facilitate material removal through physical, chemical, or hybrid mechanisms.

Dry etching typically operates under low-temperature, non-equilibrium plasma conditions, where high-energy ions and reactive radicals interact with the target material. The most employed plasma discharge mechanisms include capacitive coupled plasma (CCP) and inductively coupled plasma (ICP).

Fig. 3.7 depicts the simplified equivalent circuit for CCP and ICP. In CCP dry etch scenario, the plasma is generated by applying a RF electric field across two parallel electrodes, ionizing the process gas at a pressure range of a few to tens of millitorr. The ionization rate is typically low ($<10^{-5}$), and the plasma density is relatively moderate, making it suitable for processes where precise control of ion energy is required. In contrast, ICP utilizes an RF-driven coil to induce a time-varying magnetic field, which in turn generates a secondary electric field within the plasma, significantly enhancing ionization efficiency. This method

produces a high-density plasma (>10^{-5} ionization rate) at lower pressures, enabling better control over etching rates, selectivity, and sidewall profiles.

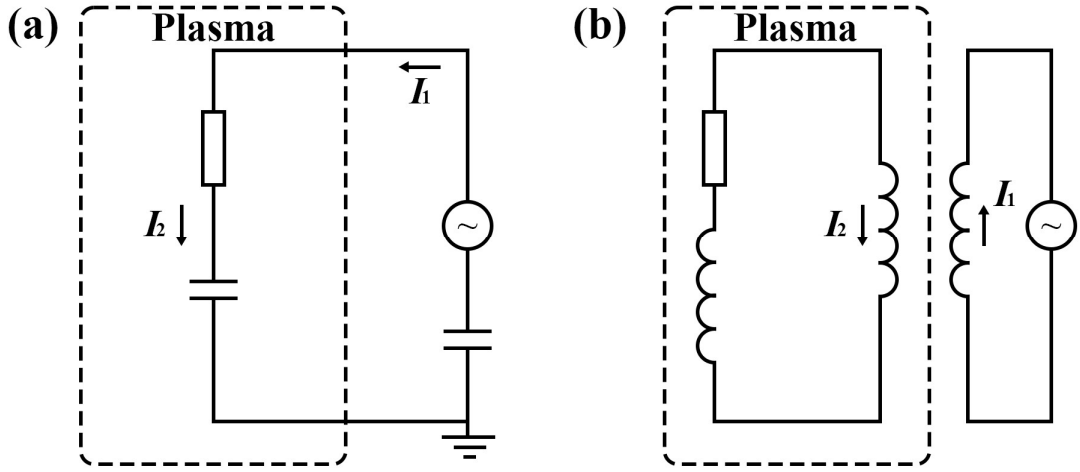

Fig. 3.7 Simplified equivalent circuit for **(a)** CCP, and **(b)** ICP.

In this study, the dry etching process for InP was performed using an Oxford Instruments PlasmaPro System 100 ICP Cobra. The etching procedure employed a gas mixture composed of chlorine (Cl_2), methane-hydrogen (CH_4/H_2) and argon (Ar). The incorporation of chlorine-based chemistry was selected to enhance the etch rate due to its ability to form volatile byproducts with InP, facilitating efficient material removal. Meanwhile, the CH_4/H_2 mixture was introduced to moderate the etching temperature, which was maintained at 60°C in this work. This was followed by an optimized gas composition that ensured a balance between etch rate, selectivity, and surface smoothness, crucial for achieving precise feature definition in semiconductor device fabrication.

3.5.2 Electrical Isolation Definition

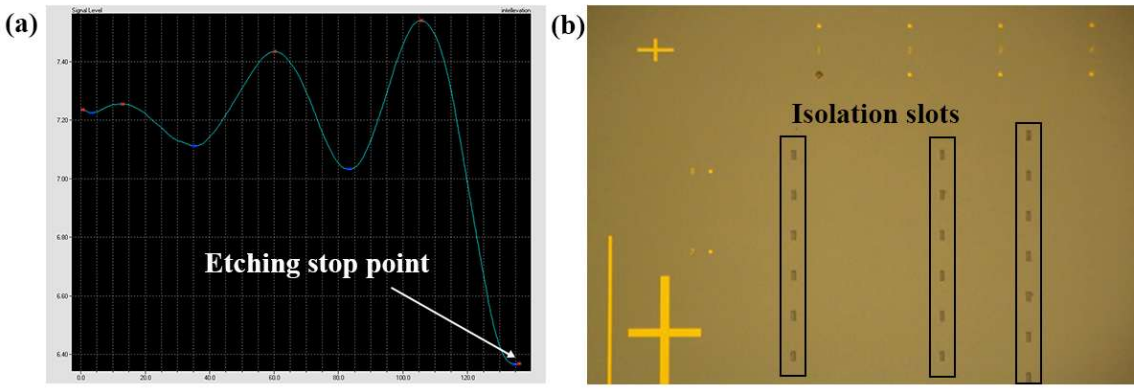

Fig. 3.8 (a) Reflectivity trace from interferometer for dry etching electrical isolation, **(b)** Micrograph of etched electrical isolation on the chip.

The heavily doped 200 nm of InGaAs and 50 nm of 1.3Q layer on the top of the wafer needed to be removed in the process of isolation etching. Due to the shallow etching depth of the electrical isolation, high mask precision is not required. For this step, we opted for PMMA as the masking material. During the etching, to precisely monitor the dry etch process, an interferometer was employed to track the etch depth. The interferometer utilized a laser system with a 675 nm laser beam to measure the light reflectivity from the sample surface [118]. As the sample material is comprised of multiple layers, the reflectivity varied with the etching of each layer. Hence, precise control of the dry etch depth can be realized. The etch recipe, $Cl_2/CH_4/H_2/Ar$ = 8/10/15/15 sccm was chosen, operating at 60°C. The ICP power and RF platen power of the machine were 750 and 100 W respectively, and the gas pressure in the chamber was 5 mTorr. Fig. 3.8(a) shows the interferometer trace of the dry etch process. The etching time was roughly 135 s, and the calculated etching rate was about 2 nm/s. Fig. 3.8(b) shows the electrical isolation after processing.

3.6 Waveguide and Grating

For electrical isolation, precision control is not as strict as for the grating. The definition of the grating requires higher resolution. As discussed in the previous chapter, the fabrication tolerance of the grating in seed grating scale needs to be less than 30 nm. We utilized hydrogen silsesquioxane (HSQ) which is a negative-tone resist known for its high resolution and resistance. After e-beam exposure, it forms a hard mask of silicon dioxide (SiO2), providing effective protection during dry etching processes. As previously discussed, selecting an appropriate exposure dose is crucial for achieving optimal patterning in EBL. Prior to executing the actual EBL process, dose tests were conducted to determine the optimal exposure parameters. This step is particularly critical for HSQ, as its sensitivity to environmental factors such as temperature, humidity, and contamination can significantly affect its lithographic performance. Moreover, the exposure characteristics of HSQ may vary over time, even within the same batch, due to gradual changes in its chemical properties with repeated usage. To account for these variations and ensure consistent patterning quality, a dose test was performed before each fabrication process.

3.6.1 Dose Test

To ensure experimental consistency and enhance the reliability of the results, a standardized spin-coating and development process was adopted during the dose test phase. Based on prior dry etching experience, HSQ has demonstrated a high selectivity (~1:5) in Cl_2-based dry etching, making it a suitable choice for pattern transfer. Given that the ridge waveguide required an etch depth of approximately 1.92 μm, a 600 nm-thick HSQ resist layer was spin-coated onto the sample surface to ensure sufficient etch resistance and prevent mask depletion during the etching process. For development, a 25% tetramethylammonium hydroxide（TMAH） solution was used, which effectively enabled the formation of high-resolution patterns. Maintaining a clean and well-defined HSQ mask was critical to

achieving precise grating structures, necessitating the removal of any residual resist after development [119].

In dose testing for EBL, the choice of the dose increment method is critical to obtaining meaningful results efficiently. Instead of employing an arithmetic progression (where dose values increase by a fixed amount), an exponential (geometric) progression is preferred, as it more accurately reflects the nature of dose variations in EBL processes. This preference arises because all physical dose variations, such as electron backscattering, beam current fluctuations, and development inconsistencies, inherently manifest as fractional changes rather than absolute differences [120].

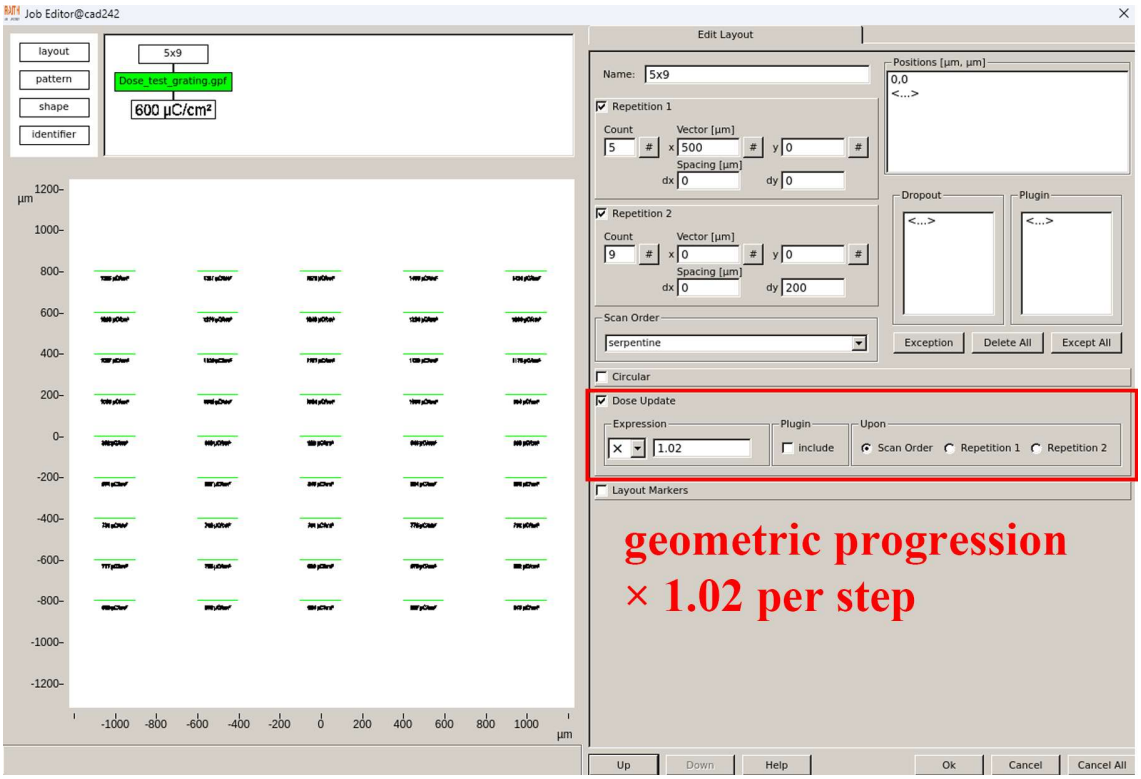

Fig. 3.9 Dose test setup in cjob file.

Fig. 3.9 shows the setup cjob file of dose test. The dose test ranges from the lowest 640 µC/cm² and increases gradually in a geometric progression up to 1440 µC/cm², by multiplying by a factor of ~1.02 per step, allowing a broad yet efficient coverage of dose variations within a reasonable number of test sites. There're 45 patterns with different doses

placed at the center of the test sample. Due to potential fabrication errors such as the beam current drifting, and development temperature varying, there may be an effective dose difference of approximately 5%-10%. Therefore, for the dose test results, it is sufficient to determine a dose range that ensures the proper formation of the grating profile and prevents any residue from overexposure in the grating slots.

Fig. 3.10 shows the comparison between the over exposed, right properly exposed, and less exposed HSQ patterns. Fig. 3.10 (a) presents the grating profile obtained with a dose of 874 μC/cm². It is evident that the duty cycle of the gratings is significantly less than 50%, indicating underexposure, implying that the dose was insufficient. Fig. 3.10 (b) displays an SEM image of the gratings exposed to a dose of 1066 μC/cm², exhibiting well-defined grating profiles. In this scenario, the EBL dose was adjusted to achieve a 50% duty cycle, resulting in rectangular-shaped grating teeth. Higher doses can lead to adverse effects on the grating profile, referred to as overexposure as illustrated in Fig. 3.10 (c). A dose of 1299 μC/cm² resulted in overexposure where regions close to exposed areas are affected by scattering electrons. HSQ residue was observed between gratings, potentially impacting the coupling coefficient after dry etching.

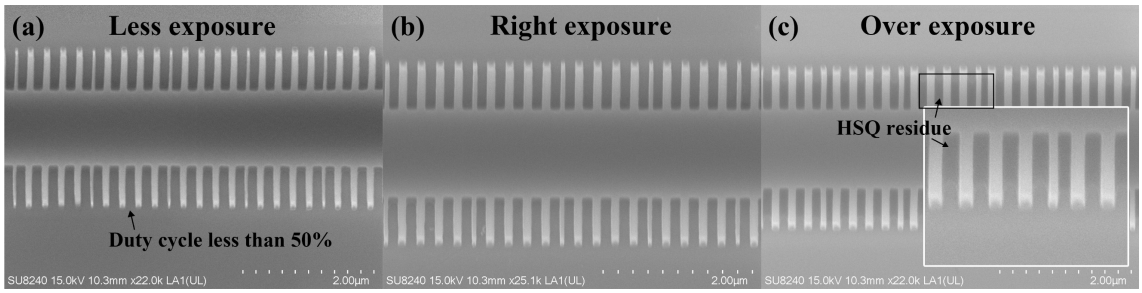

Fig. 3.10 SEM of the HSQ mask with **(a)** less exposure, **(b)** right properly exposure, and **(c)** over exposure.

According to the dose test result, I finally used these steps for grating masks definition. Firstly, an HSQ layer was deposited at 2000 rpm for 60 seconds, yielding a 600 nm-thick resist layer. The backside of the sample was then carefully cleaned with an acetone-soaked

cotton bud to remove residual solvents. followed by a soft bake at 90°C for 2 minutes on a hot plate. The ridge waveguide structures were then defined using an EBPG electron beam writer, with precise control parameters: 0.5 nm resolution, a proximity correction file (GaAs700_100_z650.xrz), an exposure dose of 1066 μC/cm², a measured beam spot size of 36 nm, and a beam current of 8 nA. After exposure, the developed patterns were processed in a 25% TMAH solution at 23°C for 30 seconds, followed by sequential rinsing in RO water for 60 seconds in two separate beakers and a final rinse in IPA for 30 seconds. The sample was then dried using gaseous nitrogen to ensure a clean and well-defined resist profile, ready for subsequent fabrication steps.

3.6.2 Dry Etch Test of InP/InGaAsP

Compared to wet etch using liquid based etchants, dry etching offers several advantages, including anisotropic etching, minimal mask undercutting, and enhanced reproducibility. This method utilizes chemical and physically reactive plasma to selectively remove the desired material. The etching conditions within the system are contingent upon several parameters, including RF power, gas composition, gas flow rates, chamber pressure, and temperature. These parameters are adjusted to establish an optimized etching recipe that yields a desirable etch profile. For various materials, different gas combinations and flow rates can be selected, impacting the proportion and concentration of the generated plasma. The electric field generated by RF power facilitates anisotropic etching, preventing undercutting. Control over pressure and temperature within the chamber enables timely evaporation and removal of by-products from the reaction chamber.

For the InP-based material etching, CH_4/H_2 gas system and Cl_2 gas systems are widely used [121], [122], [123]. Etching in a CH_4/H_2 gas mixture allows for obtaining a smooth surface morphology after etching, with a high aspect ratio of the structures formed. At the same time, the disadvantage of these processes is the usually low etching rate (about 0.1 μm/min or less) due to the formation and redeposition of the passivating polymer. Cl_2 plasma processes yield

high etching rates, typically several microns per minute. However, this process lacks sufficient anisotropy. In addition, the low-volatile component $InCl_x$ formed during the process can redeposit on the substrate resulting in surface roughness. Therefore, the chamber needs to be preheated to a high temperature usually over 150 ℃ in such a process.

In the dry etching process, especially for the high aspect ratio etching required to define the gratings, the etching rate needs to be carefully tuned. In the design, the width of the grating is 0.6 μm, and the etching depth needs to reach close to 1.92 μm near the MQW layer. It's crucial to avoid excessively rapid reaction times to prevent significant discrepancies in etching rates between the sidewalls and inside the grating slots, which could compromise vertical etching uniformity. However, longer reaction times may cause severe undercutting, resulting in a poor grating profile which will affect the device performance. Fig. 3.11(a) highlights this challenge encountered during the dry etching process, known as the Reactive Ion Etching (RIE) lag effect. As the aspect ratio increases, ion transport within the trench becomes diffusion-limited, leading to a gradual reduction in the etch rate. This effect is particularly problematic in deep-etched sidewall gratings with small feature sizes, where insufficient ion diffusion results in non-uniform etching. Fig. 3.11(b) shows a cross-sectional SEM image of the etched grating structure with red outlines highlight the etched ridge waveguide. As evident in the image, the etch depth decreases near the quantum well region due to the RIE lag effect, resulting in incomplete grating formation at the bottom. This limited ion penetration into narrow trenches leads to etch non-uniformity, which can degrade the coupling coefficient and, in turn, affect the device performance.

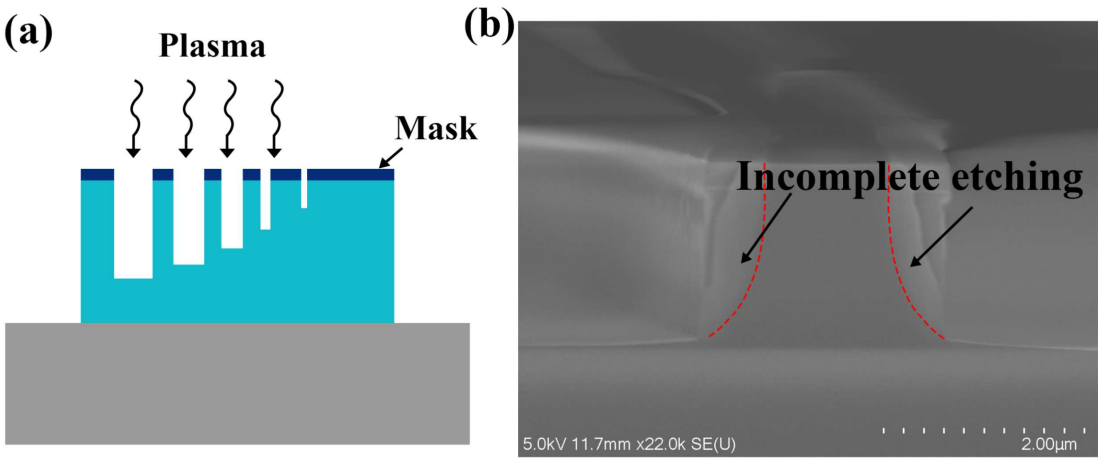

Fig. 3.11 (a) RIE-lag effect in dry etch, **(b)** cross-section of grating with RIE-lag effect.

To optimize this problem, I used a gas mixture based on $Cl_2/CH_4/H_2/Ar$ for dry etch testing. H_2 and CH_4 not only help to balance the chemical reactions between the III and the V components of the compound semiconductors but also creates passivation polymers that form on the vertical sidewalls increasing etch anisotropy. Ar provides a physical component to the etching process, increasing the surface energy of the horizontal interfaces during the etching process. By tuning the composition of each gas, several rounds of the dry etch tests were conducted and the results are shown in Fig. 3.12 with the dry etch recipe listed in Table 3.1.

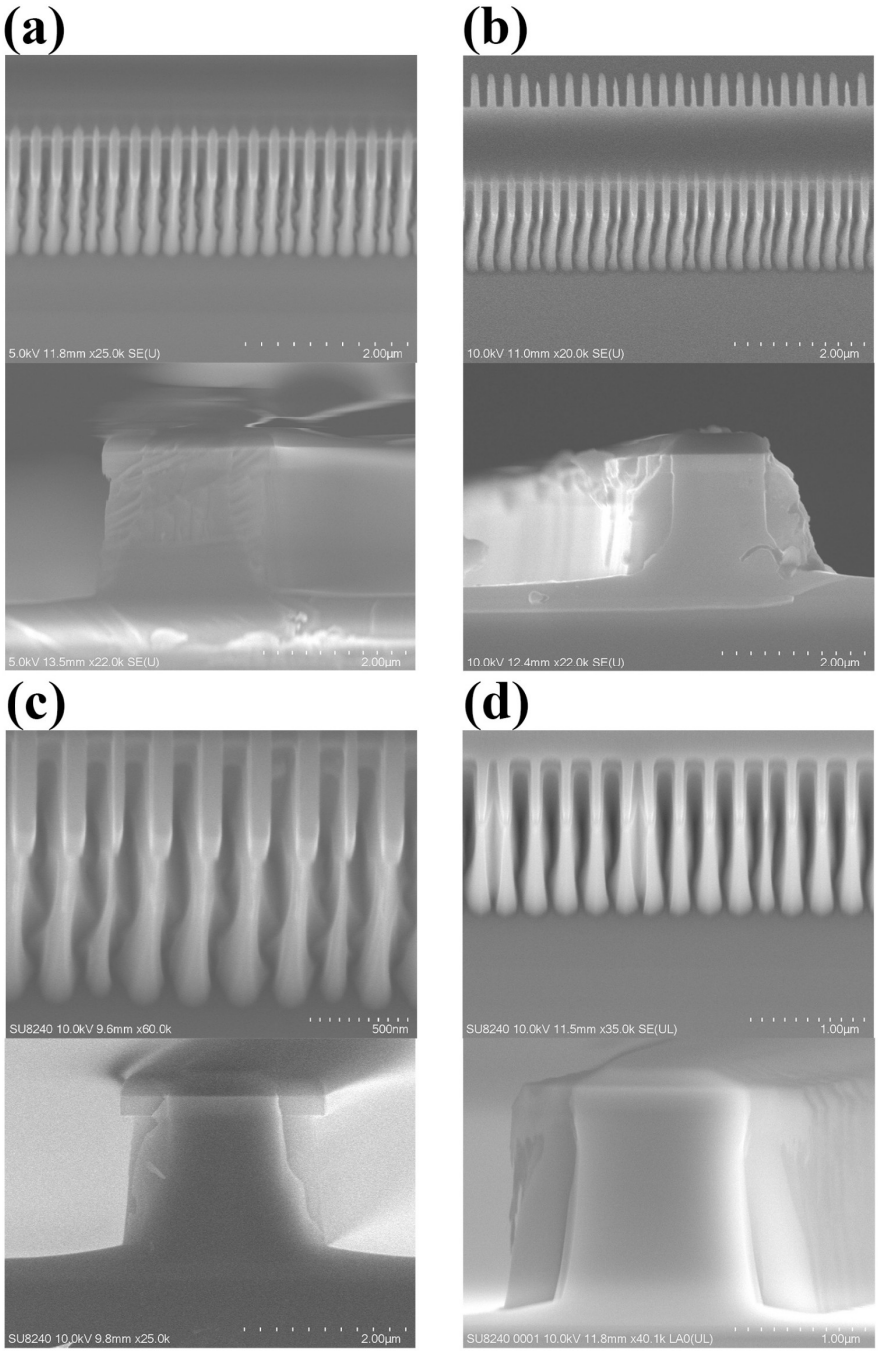

Fig. 3.12 SEM images of dry etch test results with the recipe listed in Table 3.1.

Table 3.1 Recipes for dry etch test.

Test	**Recipe**	**Etch time (s)**	**Results**
1	$Cl_2/CH_4/H_2/Ar$ = 8/10/15/10 sccm, ICP/Platen = 750/100 W, 5 mTorr,	415	Fig. 3.11(a)

	60°C, Backside He = 0 Torr		
2	$Cl_2/CH_4/H_2/Ar$ = 8/10/15/20 sccm, ICP/Platen = 750/100 W, 5 mTorr, 60°C, Backside He = 0 Torr	405	Fig. 3.11(b)
3	$Cl_2/CH_4/H_2/Ar$ = 6/10/15/20 sccm, ICP/Platen = 750/100 W, 5 mTorr, 60°C, Backside He = 0 Torr	367	Fig. 3.11(c)
4	$Cl_2/CH_4/H_2/Ar$ = 15/10/15/20 sccm, ICP/Platen = 750/100 W, 5 mTorr, 60°C, Backside He = 0 Torr	524	Fig. 3.11(d)

The experiment primarily aimed to optimize the composition of Cl_2 and Ar, as these gases respectively represent chemical and physical etching mechanisms. While CH_4/H_2 also contributes to chemical etching, its etch rate is significantly lower than that of Cl_2. The primary role of CH_4/H_2 is to form a compound layer on the etched surface, which enhances anisotropic etching. Given these considerations, our objective was to minimize the impact of the RIE lag effect by carefully tuning the gas composition. In Test 1, I used 8 sccm of Cl_2 and 10 sccm of Ar. The Cross-sectional SEM image in Fig. 3.12(a) revealed the presence of RIE lag, indicating insufficient mitigation of etch rate variation across different feature sizes. To counteract this, I increased the Ar flow rate in Test 2 to 20 sccm aiming to enhance physical etching rate for verticality. Despite this adjustment, the overall etch rate remained relatively unchanged, with the etching process completing in 405 s. I can still observed a slight improvement in the verticality of the grating sidewalls compared to Test 1. To further enhance etching uniformity, I aimed to extend the overall etching duration, as prolonged reaction time allows for more complete material removal within the grating trenches. In Test 3, I reduced the Cl_2 flow rate, anticipating a longer etching time. However, the total etching duration unexpectedly shortened to 367 s, suggesting an unintended alteration in reaction kinetics. Conversely, in Test 4, increasing the Cl_2 flow rate to 15 sccm significantly

prolonged the etching duration to 658 s. This phenomenon may be attributed to the higher viscosity of Cl_2 compared to other gases, leading to the formation of a thicker compound layer on the material surface. Since Ar is primarily responsible for physically removing these reaction byproducts, an increased Cl_2 concentration without sufficient Ar may slow down the removal process, thereby extending the overall etching time. The extended etching duration in Test 4 (524 s) allowed deeper material removal within the grating trenches, effectively reducing the RIE lag effect. While this also increased the risk of undercut, the grating profile remained well-defined. Given that in ridge waveguides, the primary modulation of optical modes occurs at the bottom of the grating, I ultimately selected the etching parameters from Test 4 for fabricating the final grating structures.

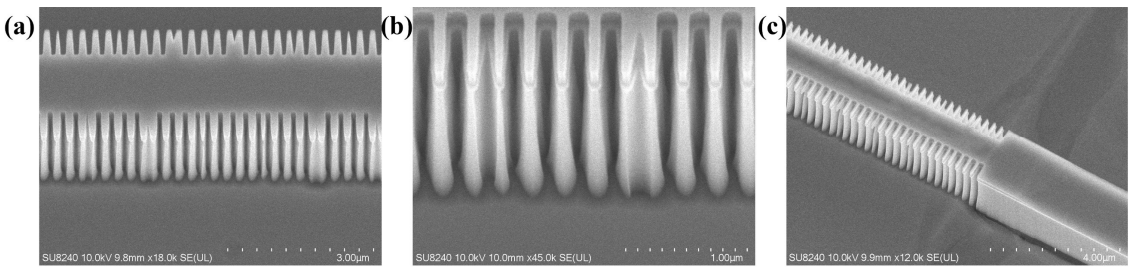

Fig. 3.13 SEM images: **(a)** lean view of the grating, **(b)** detailed view of the grating slots, **(c)** grating and waveguide profile.

The etch recipe, $Cl_2/CH_4/H_2/Ar$ = 15/10/15/20 sccm was chosen, operating at 60°C. The ICP power and RF platen power of the machine were 750 W and 100 W, respectively, and the gas pressure in the chamber was 5 mTorr. This recipe gives an etching rate of around 0.22 μm/min and a selectivity ratio of over 5 using the HSQ mask. Fig. 3.13 shows the SEM images of the etched grating slots using this recipe, although the verticality of the grating is not exceptionally high, the increased coupling coefficient achieved through our previous design of the grating structure renders this grating acceptable.

3.7 Passivation and Open Window

After defining the ridge waveguide and the gratings, dielectric films of SiO_2 were deposited as the insulator. The deposition of SiO_2 was done using a Plasma-Enhanced Chemical Vapour Deposition (PECVD) process, which is a process used to deposit thin films on a substrate by introducing a gas mixture into a vacuum chamber and then exciting it with plasma [124]. Fig. 3.14 shows the process flow of passivation. The deposition of SiO_2 was conducted in the machine PECVD PlasmaPro 100. The PECVD recipe has a deposition rate of 69.4 nm/min under 300 ℃. Following a 2 min 53 s deposition, roughly 200 nm SiO_2 was first deposited on the sample. Then, a layer of HSQ about 400 nm was spun to make the surface more uniform and smoother. The sample was put into a 180 ℃ oven and baked for 2 hours to make the HSQ solid. Finally, a 100 nm PECVD SiO_2 layer was deposited to enhance adhesion for the subsequent P-contact metal deposition, as HSQ exhibits poor adhesion to metals.

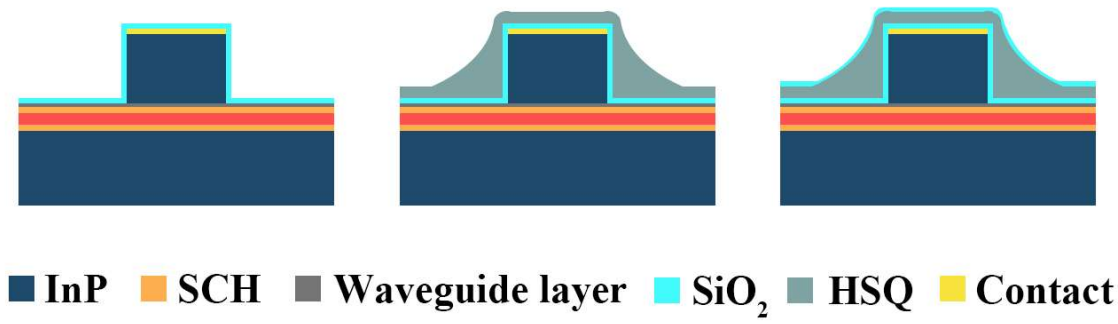

Fig. 3.14 Process of passivation.

Since the ridge waveguide was covered with insulated SiO_2, the next step is to open a contact window for P-metal deposition so that the electric current can only be injected into the top area of the ridge waveguide. In this study, an Oxford Instrument RIE 80+ system at JWNC was employed to etch SiO_2 films for contact window opening. During this process, PMMA was used as the etching mask, with electron beam exposure selectively removing the PMMA

layer only on the top of the ridge waveguides after development. The dry etching was performed using fluoroform (CHF_3) gas, with a flow rate of 30 sccm and a chamber pressure of 30 mTorr. To ensure effective material removal, the RF power was set to 200 W, and the substrate temperature was maintained at 20°C. Under these conditions, the etching recipe achieved a SiO_2 etch rate of approximately 30 nm/min. The process of open contact window is demonstrated in Fig. 3.15.

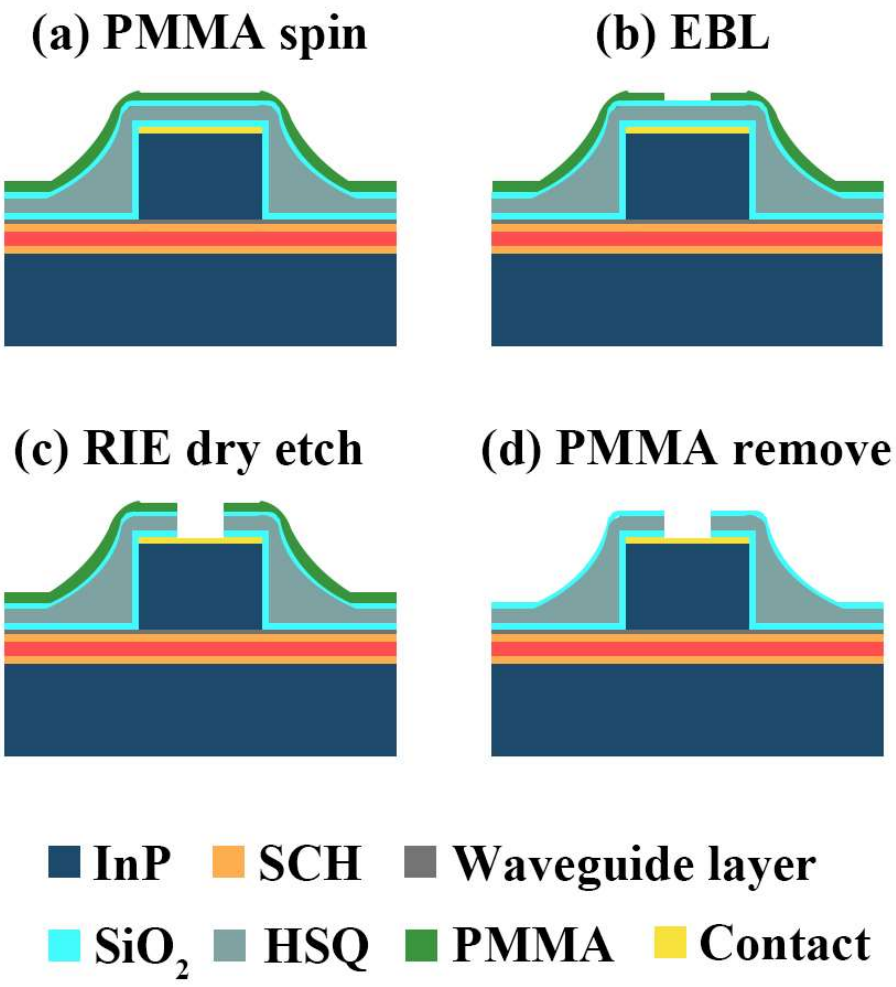

Fig. 3.15 Process of open window for p-contact.

3.8 P-Contact Metal

The process of P-metal deposition is similar to the process of aligned marker. In this step, two layers of 15% PMMA and one layer of 4% PMMA were spun on top of the sample. The P-contact metal was Ti/Pt/Au with a thickness of 33/33/240 nm respectively. The Ti is used as an adhesion layer as it is a reactive metal and oxidizes easily. The Pt layer is adopted to prevent Au from diffusing into the semiconductor layer. After the metallization, the sample was dipped into acetone (water bath at 50 °C) for about 30 minutes to remove the PMMA and lift off the metal.

Fig. 3.16 shows an SEM image of the ridge waveguide after metal deposition and the micrograph of p-contact metal after metallization and lift-off. The p-contact metal is directly interfacing the contact layer of the sample. The top 200 nm InGaAs layer in the wafer structure was heavily doped with Zn (> 1.5×10^{19} cm^{-3}), facilitating the formation of a high-quality p-type ohmic contact with the Ti/Pt/Au metal stack, thereby minimizing contact resistance and ensuring efficient charge transport. Fig. 3.16(b) shows the micrograph of the Ti/Pt/Au electrodes after lift-off process.

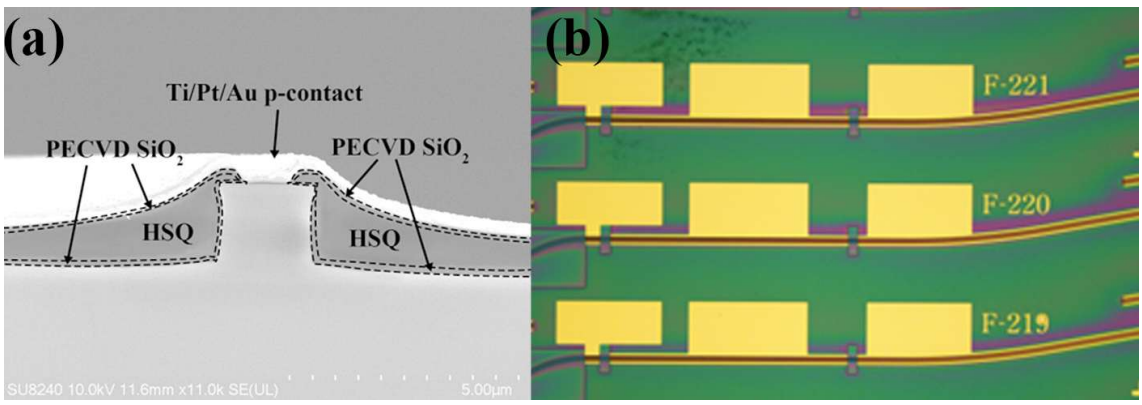

Fig. 3.16 (a) SEM image of the ridge waveguide after metal deposition, **(b)** micrograph of Ti/Pt/Au p-contact layer.

3.9 Thinning and Cleaving

To reduce resistance, the n-type substrate side of the sample was thinned from its original thickness of 370 μm to approximately 180 μm. A mechanical polishing process using Al_2O_3 powder dispersed in water was used for substrate thinning. The sample was first thinned using a 9 μm Al_2O_3 slurry at a relatively high material removal rate, followed by polishing with a 3 μm slurry to reduce surface roughness.

After thinning, n-type metallization was deposited on the backside of the sample surface. For the n-type contact, the InP was doped by Si to a level of 3×10^{18} cm^{-3}, and a metal stack of Au/Ge/Au/Ni/Au of thicknesses 14/14/14/11/240 nm was deposited by metal evaporation. Annealing using a rapid thermal annealing (RTA) machine was then carried out to achieve a better ohmic contact for the n-contact since Ge will slightly diffuse into the substrate. The annealing condition was 380 °C for 60 seconds.

After annealing, the sample was prepared for cleaving into laser bars. To achieve precise separation, a diamond tip was carefully aligned to create a scratch at the sample's edge, and pressure was applied along the crystallographic axis to facilitate clean cleavage along the intended line. Once successfully cleaved, the laser bars were ready for measurement. During testing, heat accumulation within the device can significantly impact performance. To enhance thermal dissipation, the laser bars were adhered to a copper (Cu) submount using indium (In) solder as shown in Fig. 3.17, ensuring intimate contact between the sample's bottom surface and the Cu heat sink. This bonding process effectively eliminated air gaps, thereby enhancing thermal conductivity and enabling efficient heat dissipation during device operation.

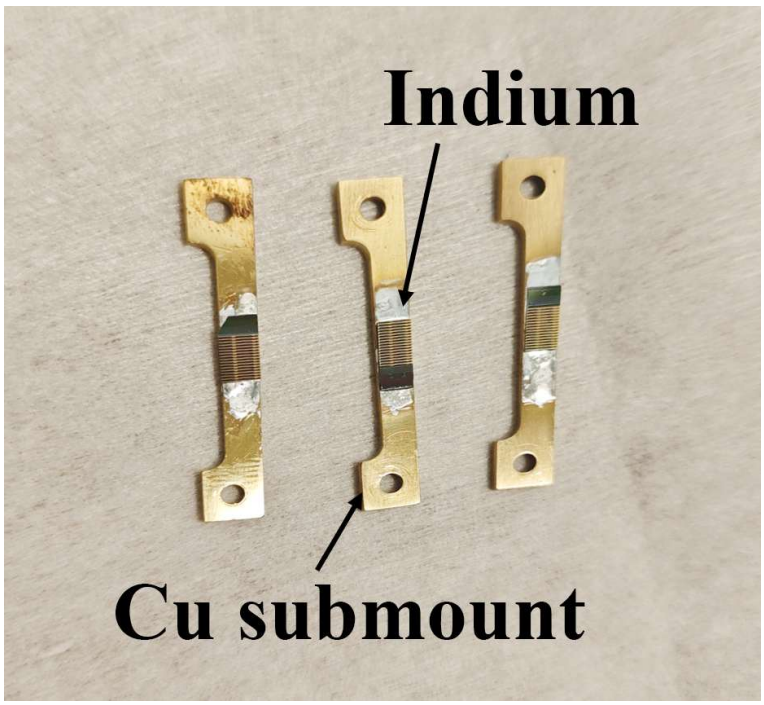

Fig. 3.17 Cleaved laser bar with Cu submount.

3.10 Chapter Summary

In this chapter, the semiconductor materials and fabrication processes used to realize the DFB diode lasers were described. The devices were based on MQW epitaxial wafers grown on AlGaInAs/InP material systems. The fabrication process was detailed step-by-step, with EBL employed throughout for high-resolution pattern definition and transfer, especially for the Bragg grating features. The process includes mask design, aligned marker definition, isolation etching, waveguide and grating etching, passivation and contact window opening, contact metallization, thinning and cleaving. Among them, waveguide and grating definitions were identified as the most critical step. This process was optimized to produce high-aspect-ratio sidewall gratings with minimal RIE lag. The overall fabrication process was consistently applied across all laser devices presented in this thesis.

Chapter 4 Dual wavelength laser based on 4PS-SBG for THz Generation

4.1 Device Design and Structures

The key issue in designing DWL is to use two different +1st order channels and each of them represents a single mode operation. The wavelength of the +1st order subgrating λ_{+1} can be expressed as:

$$\lambda_{+1} = 2n_{eff}\frac{P\Lambda_0}{P+\Lambda_0} \tag{4.1}$$

where n_{eff} denotes the effective refractive index of the waveguide guided mode, while P represents the sampling period, and Λ_0 indicates the seed grating period. The ridge waveguide exhibits an effective refractive index n_{eff} of 3.19. The seed grating period Λ_0 is set to 257 nm, corresponding to a wavelength of 1630 nm at the 0th channel. The sampling periods are precisely adjusted to position the +1st order sub-grating channel around 1555 nm, aligning with the gain peak of the MQW material. It is crucial to consider the dispersion coefficient, measured at –0.00021/nm when determining the sampling periods (P_1 and P_2) for the two lasing modes. For all five DWLs, the sampling period P_1 is set to 4639 nm. The specific sampling periods P_2 for the five DWLs are detailed in Table 4.1.

The schematic of the entire device is illustrated in Fig. 4.1. The DWL features an 1100-μm-long DFB section utilizing two 4PS-SBGs. Two SOAs, each measuring 400 μm in length, are positioned at the front and rear sides, offering gain equalization. Adjustment of the SOA current enables slight alterations in the photon distribution within the DFB laser cavity. The curved waveguides (with a radius of 1730 μm) of the SOAs are designed to produce a 10° angled output facet, thereby minimizing the occurrence of Fabry-Perot (FP) modes induced by facet reflection. Within the DFB laser

Table 4.1 Parameters for the DWL array

Channel	P_1 **(nm)**	P_2 **(nm)**	**Designed Frequency**
CH1	4639	4806	320 GHz
CH2	4639	4906	500 GHz
CH3	4639	4986	640 GHz
CH4	4639	5082	800 GHz
CH5	4639	5206	1 THz

cavity, π-phase shift sections are inserted at 1/3 and 2/3 of the DFB cavity length respectively on either side of the ridge waveguide. This configuration enables each side to operate in a single longitudinal mode (SLM) at the intended wavelength. Given that the photon density peaks occur around the π-phase shifted sections [125], distributing these sections across the DFB laser cavity separates the positions of peak light intensities of the two lasing modes. Consequently, this arrangement mitigates mode competition. Each section is isolated by a 20-μm-long electrical isolation, achieved through etching the heavily doped 200 nm thick InGaAs contact layer and the 50 nm 1.3Q layer. This isolation results in a corresponding resistance of approximately 10 kΩ.

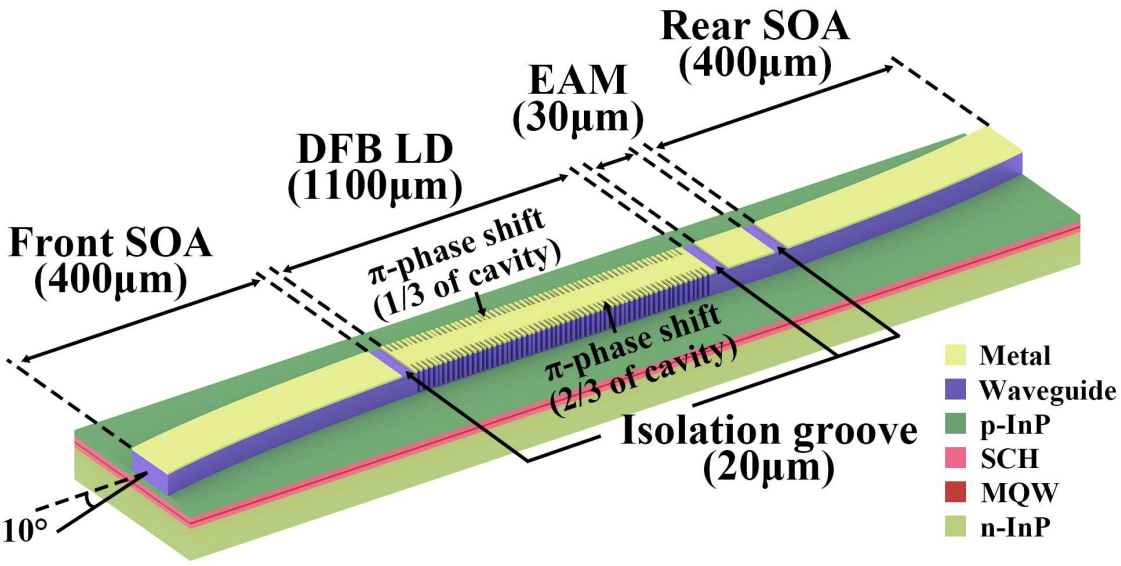

Fig. 4.1 Schematic of the dual-wavelength DFB laser based on 4PS-SBG.

Fig. 4.2(a) shows the HSQ grating mask before the dry etching process. The ridge waveguide is 2.5 μm wide, with grating recesses measuring 0.6 μm on both sides of the ridge. Fig. 4.2(b) is a microscope image of the DWL array, while the sampling periods and frequency spacings for each sidewall are detailed in Table 4.1.

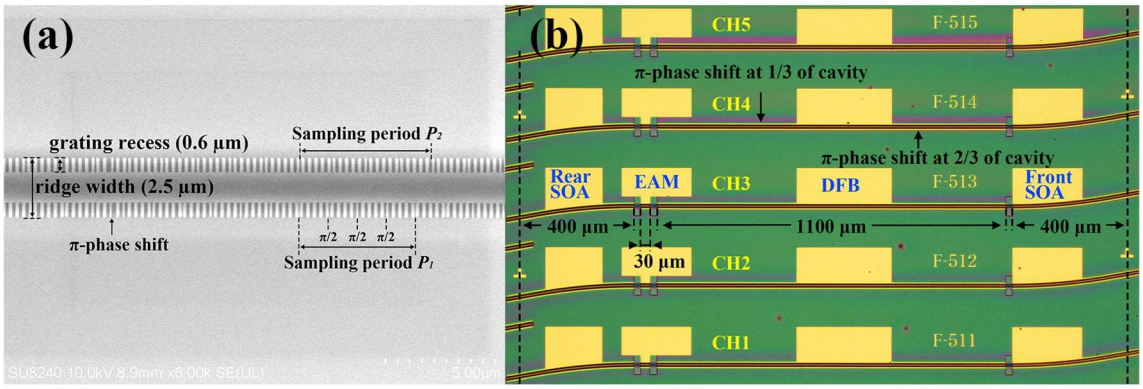

Fig. 4.2 (a) SEM picture of the sidewall 4PS-SBG structure, **(b)** Microscope picture of the fabricated DWL array.

4.2 Device Characterization

4.2.1 P-I Curve

The measurement of devices shown in Fig. 4.3 requires the use of four probes, one for the DFB section, one for the rear SOA section, one for the front SOA section and one for the

EAM section. To set up the measurement system, a schematic is shown in Fig. 4.3. A thermoelectric cooler (TEC) is placed under the laser bar for temperature control (set at 20 °C), and a current driver is used to control the injection currents and the TEC simultaneously. Additionally, a voltage driver is required to apply bias voltage to the EAM section. The output light is then coupled into a lensed fibre and detected by an optical power meter. To facilitate automated control, the general-purpose interface bus (GPIB) interface is used, and Labview is employed for automated control of the current driver. This not only reduces the measuring time significantly but also enables automatic data collection and saving.

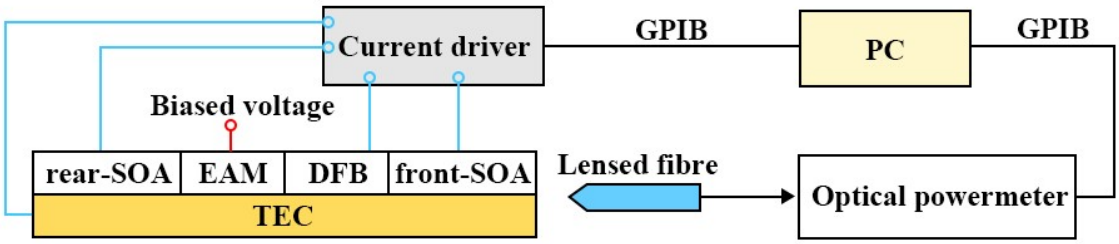

Fig. 4.3 Schematic of the set-up for optical power measurement.

The device contains a 30 μm EAM which can enhance the phase relationship between the two lasing modes and stabilize the mode beating frequency through the mechanism of FWM. In addition, it also has a SOA section to reduce the reflection and material absorption. shows the power-current curve under different front SOA currents ($I_{F\text{-}SOA}$) when the voltage of EAM (V_{EAM}) was set to 0 V. The threshold current is around 60 mA when $I_{R\text{-}SOA}$ is 0 mA and V_{EAM} is 0 V. The optical power can reach 23.6 mW when $I_{F\text{-}SOA}$ is 120 mA, $I_{R\text{-}SOA}$ is 0 mA, and V_{EAM} is 0 V.

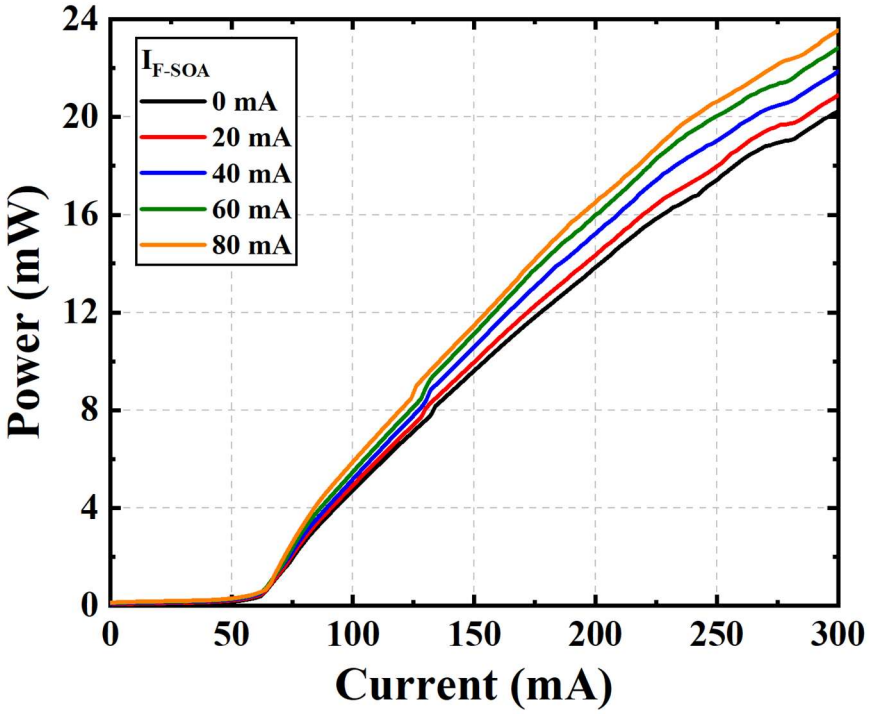

Fig. 4.4 *P-I* curves from the front SOA side when $I_{R\text{-}SOA}$ is 0 mA, and V_{EAM} is 0 V.

4.2.2 Optical Spectrum

To obtain optical spectra of the DWL array, four probes were used in each section of the device, namely the rear-SOA section, EAM section, DFB section, and front-SOA section. The set-up is shown in Fig. 4.5.

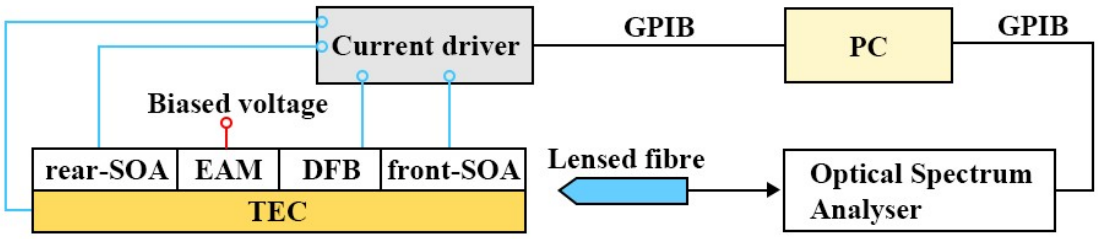

Fig. 4.5 Schematic of the set-up for optical spectrum measurement.

The measured optical spectra of the five DWL devices, along with their designed frequency spacings, are presented in Fig. 4.6. Table 4.2 outlines the measurement conditions for each device. Notably, the DWLs exhibit favorable phase relationships between the two primary lasing modes, with observable four-wave mixing (FWM) signals. In this work related to DWLs, the SMSR is defined as the ratio (in dB) between the power of the weaker of the two

main lasing modes and the highest-intensity side mode outside the main modes, excluding peaks arising from FWM. This definition is adopted to more accurately reflect the spectral purity of DWLs. The SMSRs for each device exceed 30 dB, while the power differences between the two main modes (PDM) are less than 3 dB. In the scanning optical spectra 2D map (320 GHz, 640 GHz, 800 GHz, and 1 THz) depicted in Fig. 4.7, the devices demonstrate dual-mode lasing across a DFB current range exceeding 40 mA. As the DFB current (I_{DFB}) increases, the spacing between the two lasing modes remains constant, ensuring a stable beat tone. However, occasional mode hopping is observed in the 320 GHz and 1 THz DWLs, possibly attributable to random phase shifts introduced at the cleaving facet.

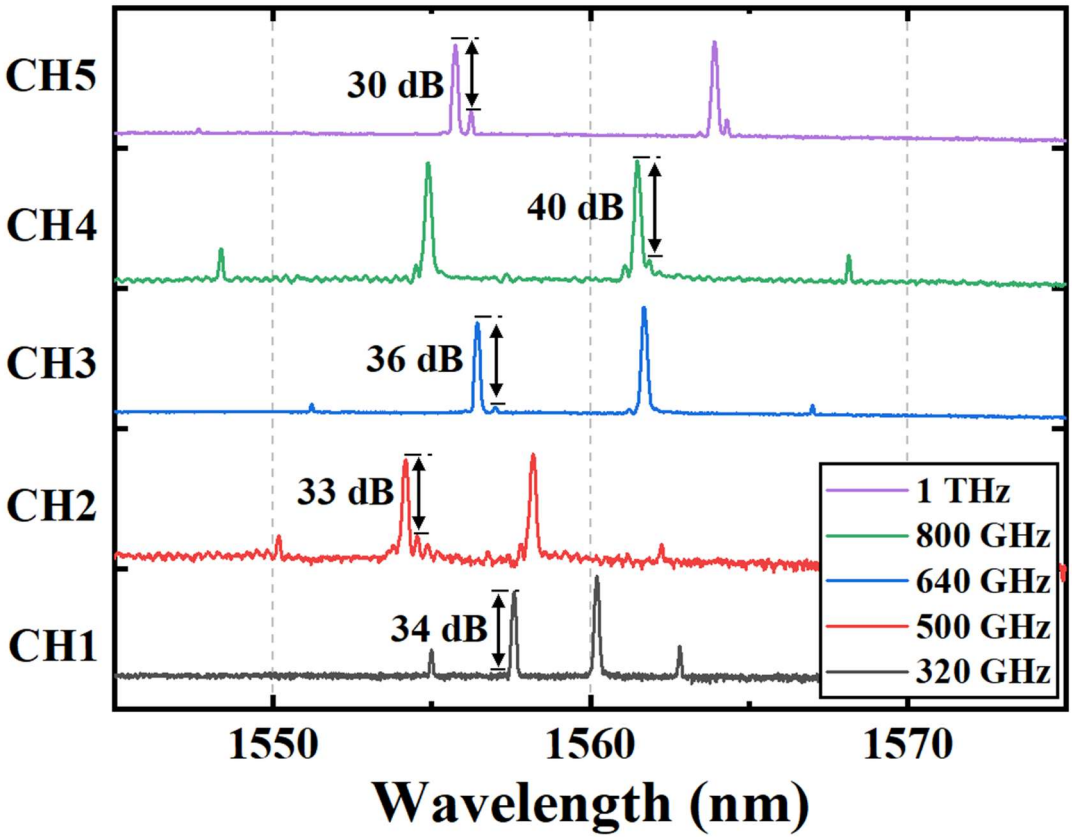

Fig. 4.6 Measured optical spectrum for each DWL device.

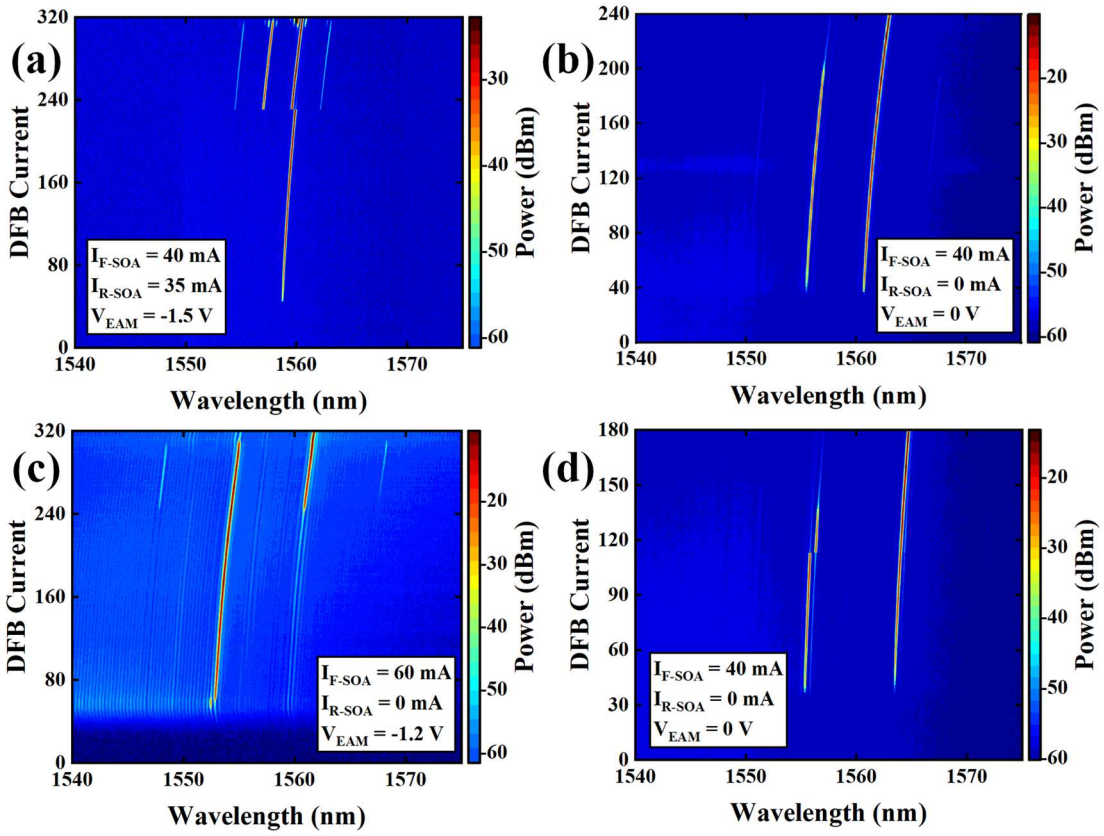

Fig. 4.7 2D optical spectra map of the DWL devices at different frequency spacings: (a) 320 GHz, (b) 640 GHz, (c) 800 GHz, (d) 1 THz.

Table 4.2 Measurement conditions for the DWL array.

Channel	**Designed Frequency**	$I_{R\text{-}SOA}$ **(mA)**	V_{EAM} **(V)**	I_{DFB} **(mA)**	$I_{F\text{-}SOA}$ **(mA)**
CH1	320 GHz	35	–1.5	295	40
CH2	500 GHz	0	0	195	60
CH3	640 GHz	0	0	175	40
CH4	800 GHz	0	–1.2	295	60
CH5	1 THz	0	0	105	40

In Fig. 4.8(a), we present a 2D optical spectrum map for the CH2 DWL (500 GHz). The

device demonstrates stable dual-mode lasing behavior with a frequency spacing of 500 GHz within the I_{DFB} range of 130 mA to 240 mA, with $I_{F\text{-}SOA}$ = 60 mA, $I_{R\text{-}SOA}$ = 0 mA, and V_{EAM} = 0 V. The spectra reveal the presence of a FWM signal under these operating conditions. When I_{DFB} exceeds the threshold current ($I_{DFB} \geqslant$ 60 mA) but remains below 130 mA, the device exhibits some mode hopping, resulting in a dual-wavelength frequency spacing of 450 GHz. The PDM and the SMSR are depicted in Fig. 4.8(b). Within the dual-mode lasing range (I_{DFB} from 130 mA to 240 mA), the PDM remains less than 3 dB, and the SMSR exceeds 32 dB. The sudden jump observed at an I_{DFB} of 130 mA is attributed to mode hopping, as illustrated in Fig. 4.8(a).

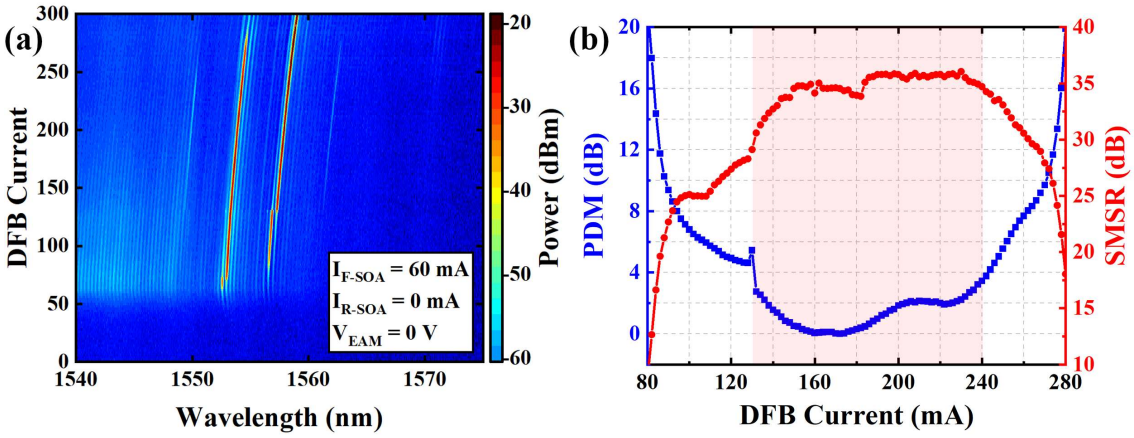

Fig. 4.8 (a) 2D optical spectra map and **(b)** SMSR and PDM as a function of the DFB current for the 500 GHz DWL device.

4.2.3 AC Trace Measurement

To ensure the generated THz frequency, AC traces were measured, which were obtained using the set-up shown in Fig. 4.9. The output light was coupled into a lensed fiber through a polarization controller and amplified by an EDFA. The polarization controller was used to control the polarization of the light to achieve the best performance. In order to prevent unwanted light reflection, an optical isolator was placed between the laser and the polarization controller. The amplified light was then transmitted into an autocorrelator for measurement purposes. The autocorrelator was used to examine the autocorrelation of the light intensity. The electrical signals generated were observed in real-time using an

oscilloscope.

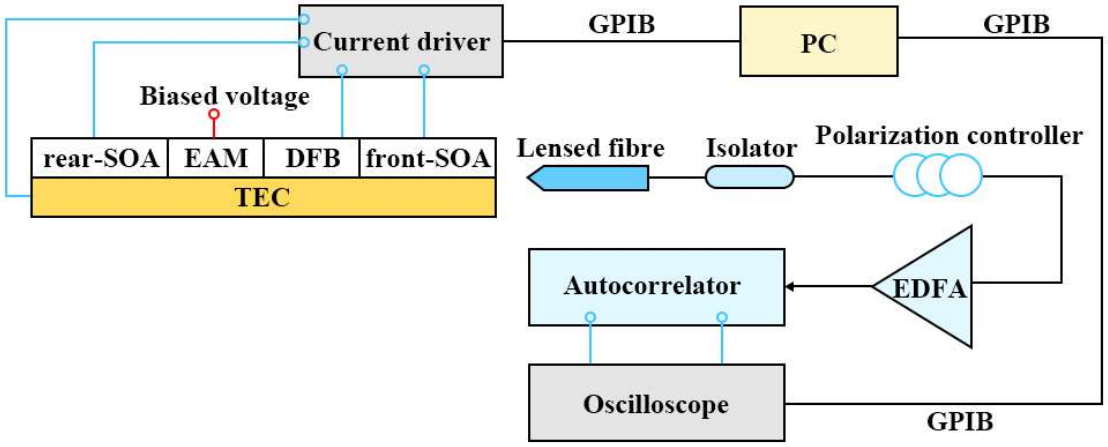

Fig. 4.9 Schematic of the set-up for AC trace measurement.

Fig. 4.10 shows the measured AC traces of the five DWL devices. The measurement condition is the same as listed in Table 4.2. The reciprocal of the average autocorrelation trace period of each DWL is consistent with its frequency separation measured in the optical spectra in Fig. 4.6, which indicates a relatively stable phase relationship between the two SLMs.

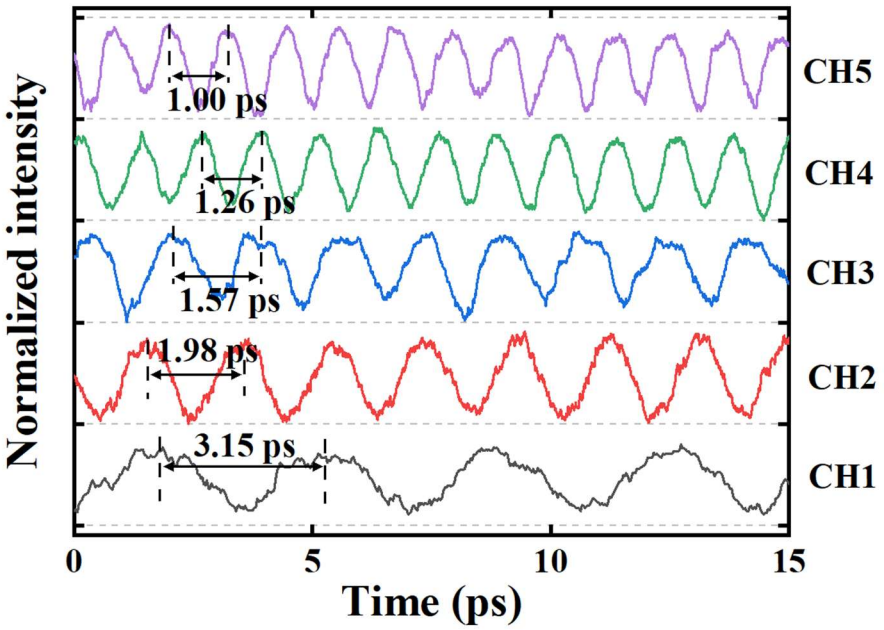

Fig. 4.10 Normalized AC traces for DWL array.

4.2.4 THz Signal Measurement

Fig. 4.11 (a) is a schematic of experimental setup for the generation and detection of THz signals. The output light emitted by the DWL was initially coupled into a lensed fiber, subsequently passing through an optical isolator. The light was amplified by an EDFA and was injected into the PCA to generate THz signals via the photomixing effect. The output signal from the DWL was amplified to an average power of 25 mW maintaining it just below the maximum power specified for the PCA. The PCA operated with a bias voltage of 8 V. The resulting THz waves were then directed into a Golay cell for signal power detection. To extract the small THz signal from the ambient noise, an optical chopper, operating at a modulation frequency of 20 Hz, was employed after the PCA. It is also important to note that during the experiment, a piece of white paper with a density of 80 g/m^2 was placed between the optical chopper and the Golay cell to obstruct the transmission of any 1.55 μm light while allowing the THz signal to pass through effectively. Because the transmission of 1.55 μm radiation through the paper is less than 10%, confirming that the leakage of 1.55 μm laser radiation could not be responsible for more than a small fraction of the signal detected by the Golay cell. Fig. 4.11 (b) shows a 2D intensity map of the THz signal transmitted through the paper, acquired from the CH2 laser with 500 GHz frequency spacing. The signal power below the threshold current is considered as the noise level and has been subtracted. The device exhibits dual-mode lasing as I_{DFB} varies from 130 mA to 260 mA. Notably, the power of the associated THz signal can reach 1.28 μW when I_{DFB} is set to 240 mA and $I_{F\text{-}SOA}$ is adjusted to 80 mA, ensuring that the input power into the PCA does not exceed 25 mW. Approximately 10% of the THz signal was captured by the Golay cell, influenced by several factors: the 30° divergence angle of radiation from the PCA, the distance (140 mm) between the PCA and the entrance of the Golay cell detector, and the 11 mm diameter of the entrance cone of the detector. Considering these factors, the total estimated THz output power is approximately 12.8 μW. Compared to monolithically integrated DFB-based THz sources using 2PS-SBG in [126], which achieved 7.6 μW output

power, exhibit significantly higher THz intensity.

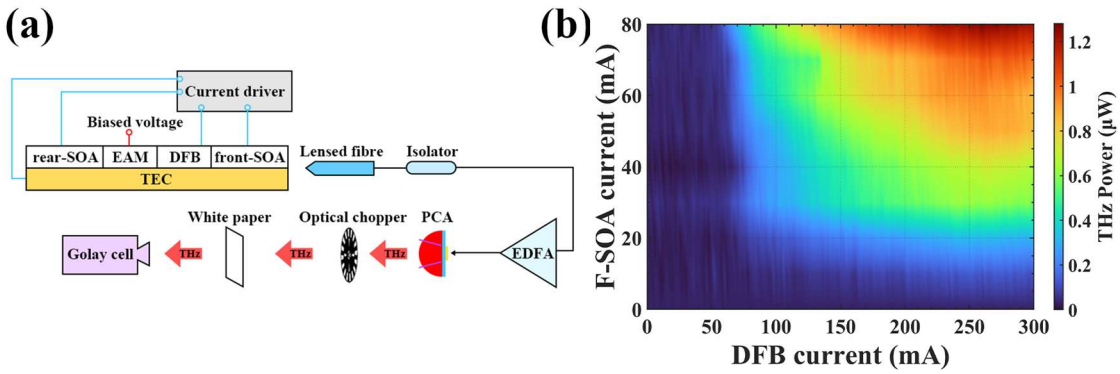

Fig. 4.11 (a) Set-up for THz measurement. **(b)** Measured THz power as a function of I_{DFB} and $I_{F\text{-}SOA}$ when $I_{R\text{-}SOA}$ is at 0 mA.

The THz sources developed in this work are suited for CW THz spectroscopy and imaging applications THz cameras [127]. Although the current setup utilizes a single-pixel Golay cell, which limits spatial resolution and system-level experimentation, the demonstrated devices provide a solid foundation for future integration into more advanced THz systems.

4.3 Chapter Summary

In this chapter, I have demonstrated a DWL array built upon the 4PS-SBG platform, offering frequency spacings of 320 GHz, 500 GHz, 640 GHz, 800 GHz, and 1 THz. The integration of 4PS-SBG enhances coupling efficiency and facilitates precise control of wavelength spacing. The measurement setup including PI curve, optical spectrum, AC traces and THz signal power, have been presented. The lasers exhibit stable dual-mode operation within a maximum current range of 110 mA, with SMSR exceeding 30 dB and PDM lower than 3 dB. AC traces closely align with the designed frequency spacings. Additionally, the THz signal generated by PCA reaches a power level of 12.8 μW.

Chapter 5 Dual-wavelength Laser Based on SMG for MMW Generation

5.1 Introduction

Innovative approaches for MMW signal generation have gained significant attention, particularly in the context of 5G communications, radio systems, and vehicular networks [128], [129]. Researchers have explored both electronic and photonic methods for MMW signal generation. Photonic methods have distinct advantages, offering a more compact system design and better noise characteristics compared to their electronic counterparts [130], [131], [132], [133]. Among the photonic solutions, the utilization of monolithic dual-mode laser sources has emerged as a promising avenue due to their compact form factor and cost-effective fabrication.

For DFB lasers, the grating is a key function determining the optical output signal. DWLs have been reported using different grating modulation schemes such as chirp and apodization [133], [134]. Moreover, Moiré gratings (MGs), formed by superimposing two Bragg gratings with slight period differences, exhibit some special features such as perfect apodization with a cosine profile and π phase shift in the cavity [134]. To generate MMW signals with conventional MGs, a very slight difference in grating periods (~0.1 nm) is needed, which can be challenging to achieve in practice. Recent literature reports that sampled Moiré gratings (SMG) are an effective approach for addressing the challenge of fabricating gratings with extremely small period differences. Using SMGs, the wavelength control precision required for a conventional MG is relaxed from the nanometer scale to the micrometer scale, substantially mitigating the influence of manufacturing inaccuracies. The achievement of single wavelength lasing in such a device was realized with a 20 nm difference between the two sampling periods [135], [136]. In reference [137], the potential for dual-wavelength lasing using conventional sampled Moiré gratings (C-SMG) is discussed, although it remains

in the simulation phase. However, the grating coupling coefficient κ of a C-SMG in the $\pm1^{st}$ channel is only $1/\pi$ of that of a UBG. In addition, the presence of the 0^{th} channel in a C-SMG can also impact the performance of the device.

To overcome the relatively low κ and prevent the effect of 0^{th} channel, I used 4PS-SMG design for dual-wavelength lasing. Utilizing the 4PS-SMG, a sampling period difference of 59 nm is required between the two superimposed 4PS gratings, which can readily be defined using EBL. Meanwhile, in contrast with a C-SMG, the κ of the $+1^{st}$ channel in the 4PS structure can be as high as 0.9 times that of the UBG, and the 0th channel is effectively suppressed [102]. Moreover, the DFB laser relies on a sidewall grating structure, enabling simultaneous fabrication of the ridge waveguide and gratings. In contrast to the traditional buried grating DWL approach, our method requires only a single step of MOCVD and one step of III-V material etching, streamlining the entire device fabrication process. Simultaneously, our approach mitigates the problem of misalignment between the ridge waveguide and the grating, an issue that can arise with multiple exposures [138].

5.2 Device Design and Analysis

The schematic of C-SMG and 4PS-SMG is illustrated in Fig. 5.1(a). The C-SMG structure comprises both grating and non-grating sections, with each section being half of the sampling period in length, resulting in a coupling efficiency for the $+1^{st}$ order sub-grating channel approximately $1/\pi$ times that of a uniform grating. In contrast, the 4PS-SMG structure divides sampling period into four equal sections, with each adjacent section featuring a $\pi/2$-phase shift. This yields a coupling efficiency for the $+1^{st}$ order sub-grating channel approximately 0.9 times that of a UBG. The TMM was used to calculate the reflection spectrum of the UBG, conventional sampled and 4PS sampled gratings in Fig. 5.1(b). Notably, the 4PS sampled structure not only eliminates the 0th order channel but also enhances the $+1^{st}$ order sub-grating channel by approximately three times compared to the conventional sampled structure. In both SMG types, different sampling periods, i.e., P_1 and

P_2, are employed on each side of the ridge waveguide to create an equivalent index modulation along the DFB laser cavity.

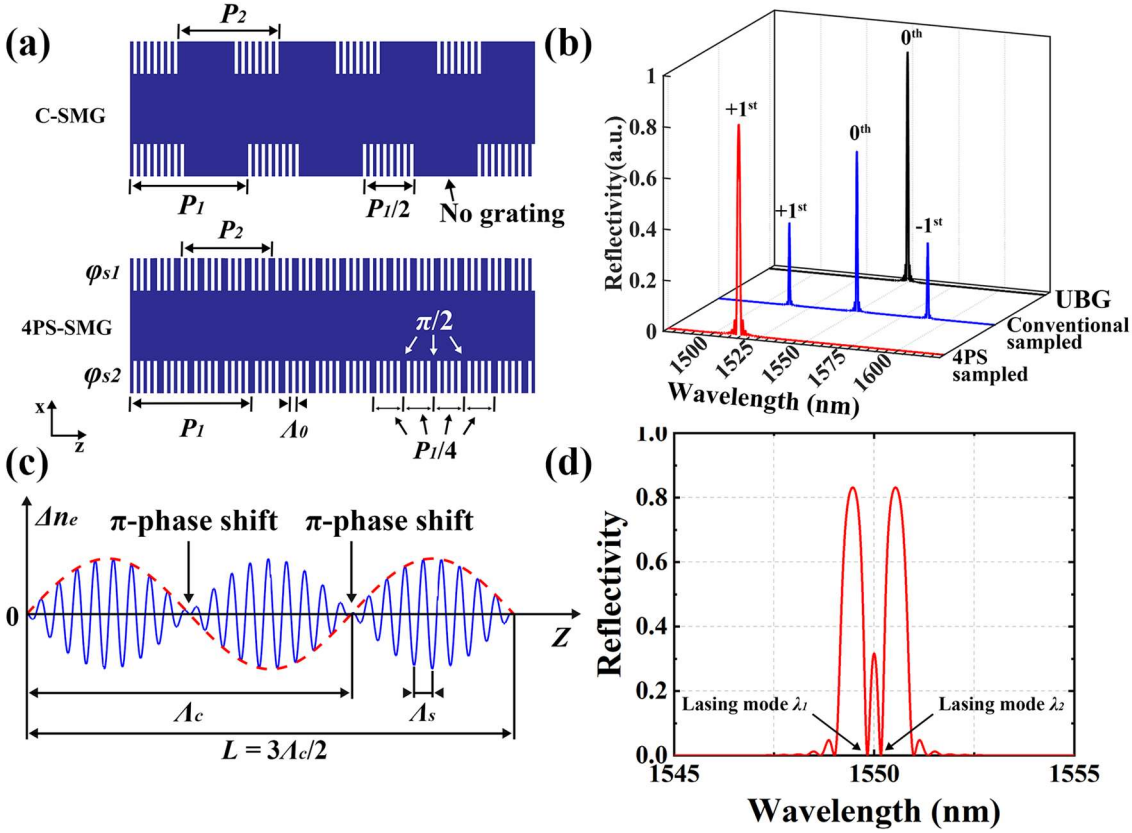

Fig. 5.1 (a) Top view of the C-SMG and 4PS-SMG. **(b)** Calculated reflectivity of UBG, conventional, and 4PS sampled gratings. **(c)** Equivalent refractive index modulation of the +1 order sub-grating inside the grating cavity based on an SMG. **(d)** Calculated reflection spectrum of 4PS-SMG.

For mathematical analysis, a seed grating with a period of Λ_0 and a duty cycle of 50% is assumed. The sampling periods on each side of the grating are denoted as P_1 and P_2. The initial phase of the seed grating is denoted as φ_0, while the phases of the two 4PS-SBGs are represented by φ_{s1} and φ_{s2}. The grating recess is d, and the ridge width is W as shown in the bottom of Fig. 5.1(a). Utilizing Fourier analysis, we can extract the $+1^{st}$ order sub-grating period as [137]:

$$\Lambda_{+1}(x)=\begin{cases}\Lambda_1=P_1\Lambda_0/(P_1+\Lambda_0) & \left(-\frac{W+d}{2}<x<0\right)\\ \Lambda_2=P_2\Lambda_0/(P_2+\Lambda_0) & \left(0<x<\frac{W+d}{2}\right)\end{cases} \tag{5.1}$$

Using the period of the +1st order sub-grating, we can formulate the relative permittivity perturbation. Following the principles of coupled mode theory [139], we isolate the phase-matching component of the perturbation for each sampling structure, allowing us to derive the coupling coefficient of the +1st order sub-grating within the SMG. The variation in the coupling coefficient exhibits a cosine function with a periodicity of Λ_c and an initial phase offset of ($\varphi_2 - \varphi_1$) along the waveguide direction. A comprehensive analysis and in-depth discussion on this topic can be found in [138]. As a result, we can find the equivalent index modulation Δn_e for the +1st order sub-grating channel in the SMG as follows:

$$\Delta n_e(z)=\Delta n\cdot F_{+1}\cos\left(\frac{2\pi z}{\Lambda_s}+\frac{\varphi_1+\varphi_2}{2}\right)\cos\left(\frac{2\pi z}{\Lambda_c}-\frac{\varphi_2-\varphi_1}{2}\right) \tag{5.2}$$

where Λ_c=2$\Lambda_1\Lambda_2$/(Λ_2-Λ_1), and Λ_s=2$\Lambda_1\Lambda_2$/(Λ_1+Λ_2), φ_1=φ_0+φ_{s1}, and φ_2=φ_0+φ_{s2}. F_{+1} is the +1st order Fourier coefficient of the sampling structure. Because the two sampling periods are close in value, there is a significant disparity between the values of Λ_s and Λ_c ($\Lambda_c \gg \Lambda_s$). Therefore, the mathematical form of the refractive index modulation of the +1st order sub-grating in SMG becomes an envelope function with the rapid changing component having a period of Λ_s and the slowly changing envelope a period of Λ_c. In addition, the equivalent refractive index creates a π-phase shift where the cosine variation of the envelope meets a crossover [134].

Fig. 5.1(c) shows the equivalent index modulation within the cavity. The cavity length is set to be L=1.5×Λ_c. The rapidly oscillating component (with the period Λ_s) defines the position of the center of the Bragg reflection band as λ=2$n_{eff}\Lambda_s$, where n_{eff} is the effective index and λ is the center Bragg wavelength. The initial phase of the envelope indicates a phase difference

of π between two sampling structures (φ_{s1} and φ_{s2}). Consequently, this design creates two π-phase shift points within the cavity, resulting in dual longitudinal mode lasing.

To validate these observations, simulations were carried out using TMM, as depicted in Fig. 5.1(d). The coupling coefficient varies along the cavity with a period Λ_c, while the initial phase difference between the two sampling structures is π. The desired lasing modes both fall within the central stop band, as shown in Fig. 5.1(d).

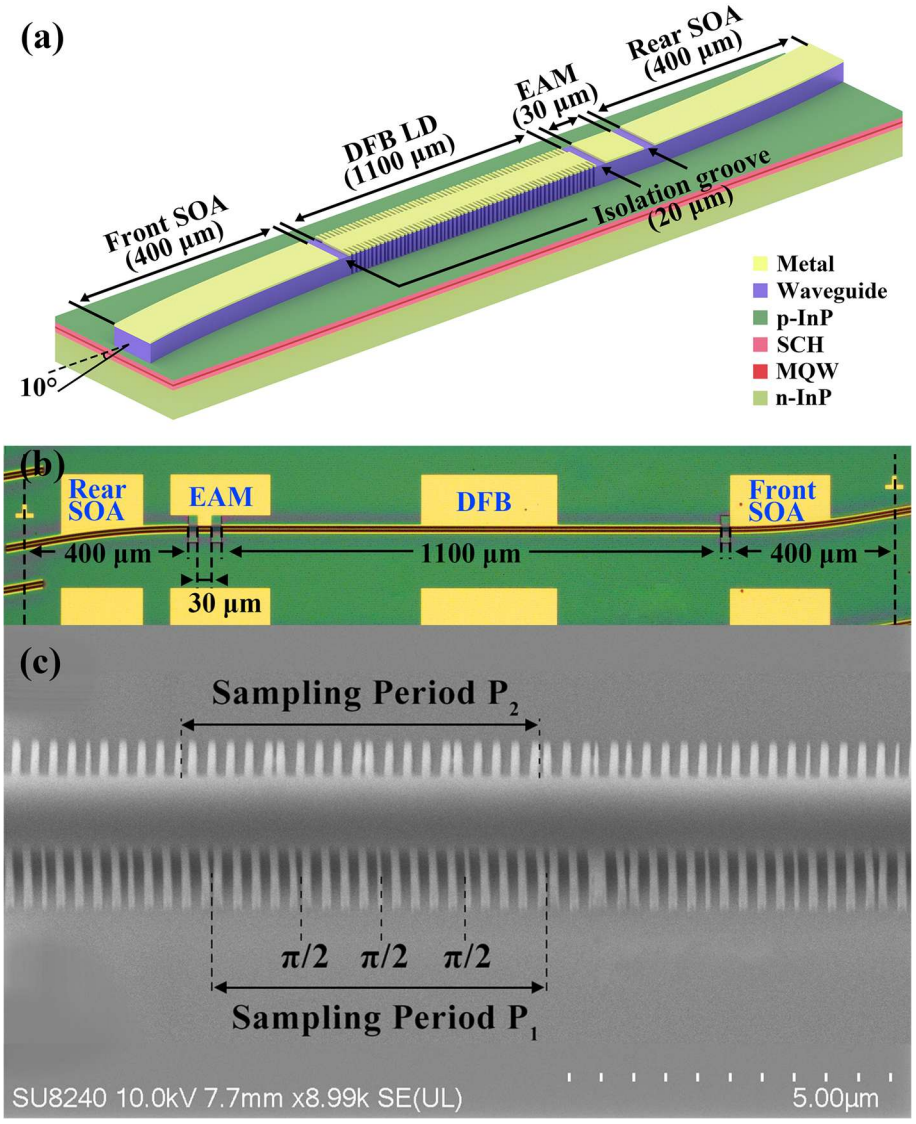

Fig. 5.2 (a) Schematic of the dual-wavelength DFB laser based on SMG structures. **(b)** Optical microscope picture of the device. **(c)** SEM image of the ridge waveguide and sidewall grating defined by HSQ.

The proposed DFB laser is fabricated in the AlGaInAs/InP-based material system. The MQW structure consists of 5 QWs and 6 QBs. Each QW has a thickness of 6 nm with a compressive strain of 1.2%, while the QB has a thickness of 10 nm with a tensile strain of -0.3% [140].

A schematic of the whole device is shown in Fig. 5.2(a). The SMG-based DFB section is 1100 μm long (L=1.5×Λ_c). The device also contains two 400-μm-long SOAs on either side of the DFB section for gain equalization, because adjustment of the SOA currents can slightly alter the photon distribution inside the cavity. The curved waveguides are designed with tilt angles of 10° (radius equals 1730 μm), which also eliminate the FP modes caused by the facet reflection. The 30-μm-long EAM is included to adjust the output power and the phase of the two lasing modes when applying a suitable reverse voltage, ensuring the two longitudinal modes have relatively equal intensities. Between each component, there is a 20 μm wide electrical isolation grove created by etching the heavily doped 200 nm thick InGaAs contact layer and 50 nm 1.3Q layer. The isolation resistance is around 10 kΩ. A micrograph of the whole fabricated device is shown in Fig. 5.2(b).

Fig. 5.2(c) displays the HSQ grating mask prior to the dry etching process. The ridge waveguide has a width of 2.5 μm, while the grating recesses are 0.6 μm on both sides of the ridge. The seed grating has a period of 257 nm. The sampling periods, P_1 and P_2, are 4.609 μm and 4.668 μm respectively on either side of the ridge waveguide. The SMG structure is realized based on 4PS sampled gratings. In each sampling period, it is divided into 4 parts with π/2-phase shift to the adjacent section. The initial phase of the sampled grating at each side has a difference of π according to the previous analysis.

5.3 Device Characterization

The detailed fabrication process can be found in Chapter 3. The completed chip was cleaved into bars, soldered to a copper sub-mount using indium, and characterized under CW

conditions at 20 °C. The cooling system employed a TEC in conjunction with a copper heat sink that integrates water cooling. It is important to note that all the measured results are obtained from the front side of the SOA.

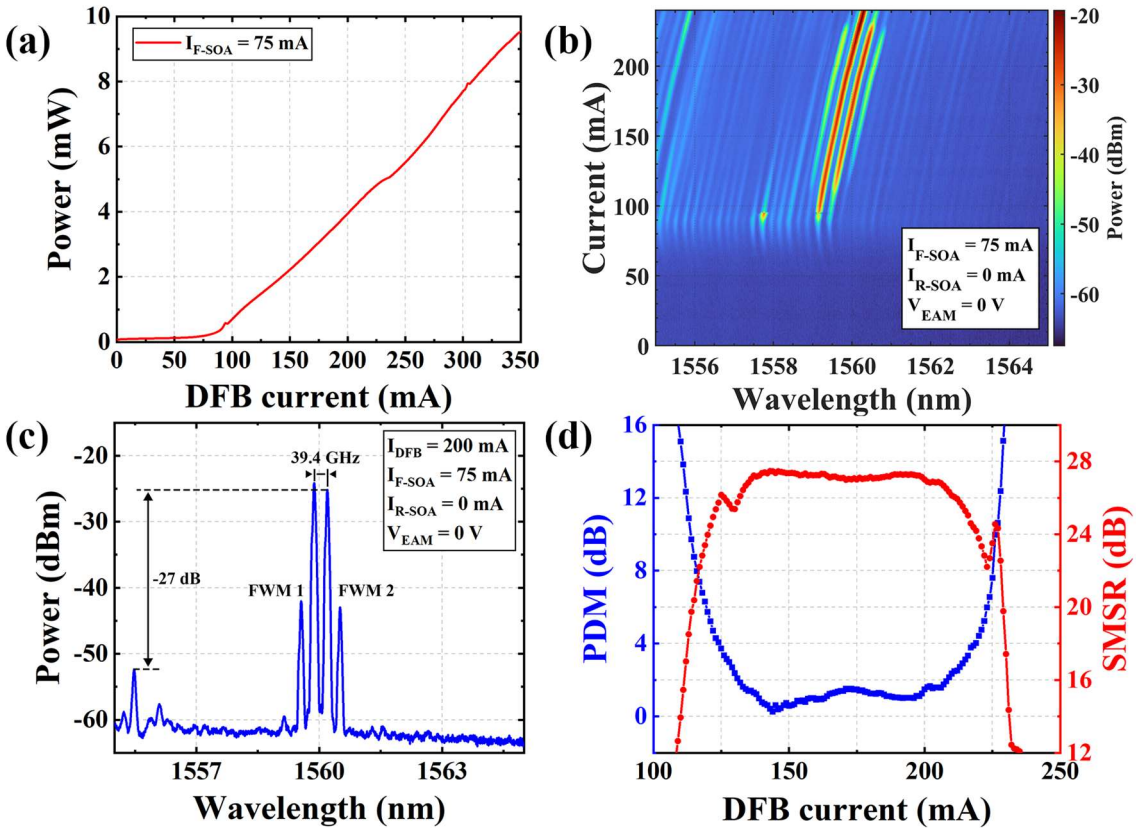

Fig. 5.3 (a) *P-I* curve when $I_{F\text{-}SOA}$ =75 mA, $I_{R\text{-}SOA}$= 0 mA, and V_{EAM} =0 V. **(b)** 2D optical spectrum vs I_{DFB} when $I_{F\text{-}SOA}$ = 75 mA, $I_{R\text{-}SOA}$ = 0 mA, and V_{EAM} = 0 V. **(c)** Dual-mode operation spectrum when I_{DFB} =200 mA. **(d)** PDM and SMSR vs I_{DFB}.

The power-current (*P-I*) curves were measured with the front SOA current ($I_{F\text{-}SOA}$) at 75 mA, the rear SOA current ($I_{R\text{-}SOA}$) at 0 mA and the voltage of EAM (V_{EAM}) at 0 V. As shown in Fig. 5.3(a), the threshold current is 80 mA. The output power can reach 9.6 mW at a DFB current (I_{DFB}) of 350 mA. The comparatively lower output power may result from the misalignment between the peak gain of the front SOA (1523 nm) at 75 mA and the center wavelength of the dual-wavelength DFB laser, which is approximately 1560 nm (refer to Fig. 5.3(c)). Addressing this issue can be achieved by optimizing the length of the SOA.

In Fig. 5.3(b), the 2D optical spectrum is displayed as a function of I_{DFB}. The device exhibited very stable dual-mode lasing behavior within the I_{DFB} range of 130 mA to 210 mA, with $I_{F\text{-}SOA}$ =75 mA, $I_{R\text{-}SOA}$=0 mA, and V_{EAM} =0 V. The spectra reveal the presence of a FWM signal, indicating a good phase relationship between the two main lasing modes. The TE_{01} leaky mode, which is manifest around 1555 nm, can be attributed to the asymmetry of the dual-sided grating within the SMG cavity. This asymmetry leads to mode conversion between the forward TE_{00} mode and the backward TE_{01} mode [127]. Fortunately, this leakage mode does not affect the performance of DWL devices. A detailed optical spectrum at I_{DFB} = 200 mA is depicted in Fig. 5.3(c). The corresponding optical frequency difference between the two lasing modes is 39.4 GHz. The SMSR is measured as 27 dB. The PDM and the SMSR are shown in Fig. 5.3(d). The device shows very stable dual-mode lasing over a range of 80 mA (130 mA-210 mA), where the PDM is less than 2 dB and the SMSR exceeds 25 dB.

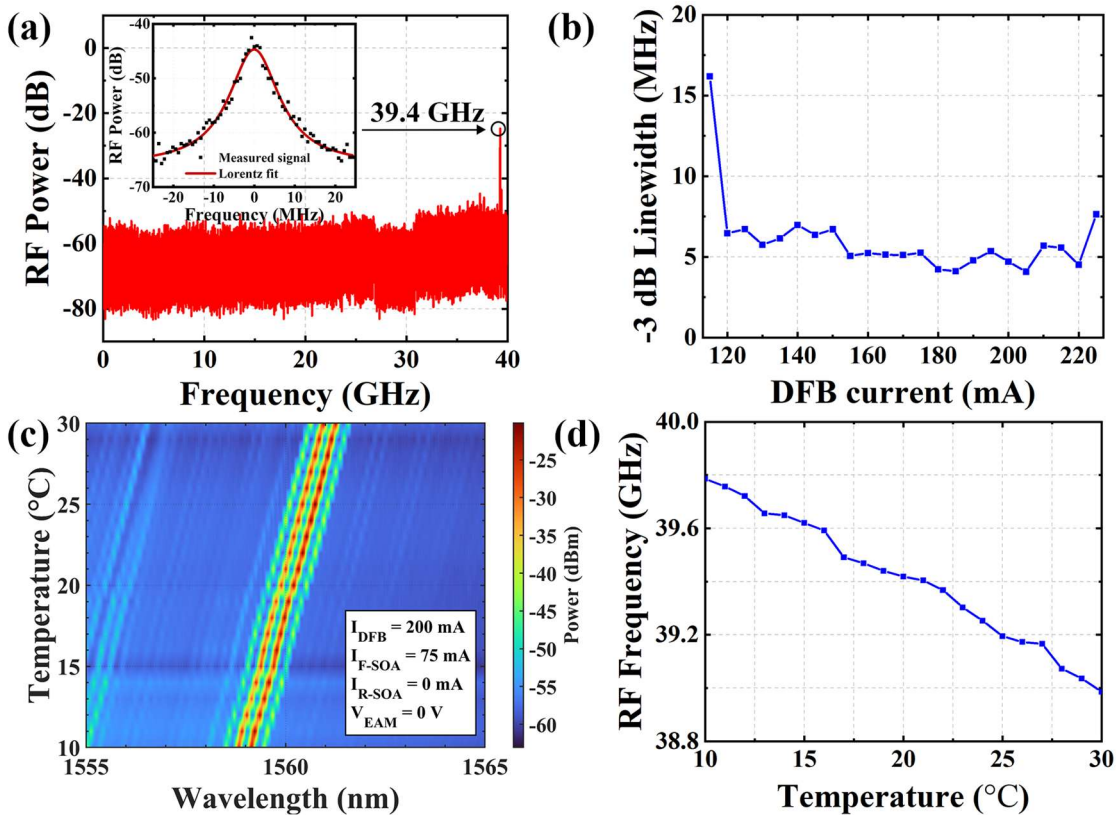

Fig. 5.4 (a) Measured full span RF signal and zoomed-in RF peak with Lorentz fit (inset). **(b)** Measured –3 dB linewidth vs I_{DFB}. **(c)** 2D optical spectrum vs temperature when I_{DFB} = 200 mA. **(d)** RF frequency vs temperature when I_{DFB}= 200 mA.

Fig. 5.4(a) shows the RF signal with I_{DFB} set to 200 mA, $I_{F\text{-}SOA}$ to 75 mA, $I_{R\text{-}SOA}$ at 0 mA, and V_{EAM} at 0 V. The RF signal has a 30 dB peak over the noise floor, with a resolution bandwidth (RBW) value set at 1 MHz. The center frequency is 39.4 GHz which corresponds to the wavelength spacing of dual-mode lasing as shown in Fig. 5.3(c). As demonstrated in the inset of Fig. 5.4(a), the beat note of the RF signal (black dots) was fitted using a Lorentz profile (red line), where the RBW of the electrical spectrum analyzer (ESA) was set to 10 kHz and the span was 400 MHz. The –3 dB bandwidth is 4.7 MHz according to the fitted profile when I_{DFB} is 200 mA. The –3 dB linewidth as a function of I_{DFB} is shown in Fig. 5.4(b). The device shows a stable linewidth around 5 MHz when I_{DFB} is within the range of 120-220 mA. The device shows a typical trend of the linewidth reducing as I_{DFB} is increased. When I_{DFB} falls outside the dual-mode operation range, the PDM experiences a significant increase, resulting in a corresponding broadening of the linewidth. The narrowest linewidth is 4.07 MHz when I_{DFB} is 205 mA.

Fig. 5.4(c) illustrates the wavelength shift over a working temperature range from 10 °C to 30 °C. The temperature tuning coefficient of the wavelength is 0.105 nm/°C. The corresponding RF frequency is also measured, as shown in Fig. 5.4(d). The wavelength separation between the two primary modes remains constant, whereas the center wavelength experiences a redshift with increasing temperature. The RF frequency, as a result, changes from 39.8 GHz to 39.0 GHz. The minor deviations observed in the RF frequency, as compared to a straight line, can be attributed to factors such as the noise generated by the DC source and external environmental variables, including temperature fluctuations within the device and mechanical vibrations. Implementing a battery-powered DC source, enhancing temperature control, and ensuring a more stable measurement platform with reduced vibration, along with packaging the device, would likely mitigate this phenomenon.

The demonstrated RF signal, located within the Ka band, aligns with frequencies of interest for MMW wireless communications, particularly in future 5G/6G backhaul links and short-range high-resolution radar systems. These applications demand compact, frequency-stable

sources with low phase noise and moderate output power. The device has the potential to serve as an integrated photonic source for such systems.

5.4 Chapter Summary

In this chapter, I demonstrate a DWL utilizing a sidewall 4PS-SMG. The approach requires only a single step of MOCVD and a solitary step of III-V dry etching, resulting in a substantial simplification of the fabrication processes. The lasers displayed stable dual-mode operation over a current range of 80 mA. The generated RF frequency was measured to be around 39.4 GHz, with a linewidth of approximately 5.0 MHz. These experimental findings underline the potential of the device as a highly integrated, user-friendly source of MMW.

Chapter 6 Mode-Locked DBR and DFB Lasers with Multiple Phase-Shifted Gratings for THz Generation

6.1 Introduction

MLLDs have emerged as essential components in advanced photonic systems, driving innovations in telecommunications, high-speed data processing, and THz signal generation. Their compact form factor, robustness, and cost-effective fabrication make them ideal for integration into miniaturized systems. Furthermore, the ability of MLLDs to produce ultra-short pulses at high repetition rates is critical for generating high-quality THz signals using photoconductive components [141].

The generation of ultra-short pulses is typically achieved using mode-locking techniques [71], which synchronize the phases of longitudinal modes to produce periodic pulse trains. For mode-locked frequency generation into the THz range, various approaches have been explored, including HML techniques with CCM [88], [91] and CPM [82]. The QCLs using active mode-locking method have also been reported. QCLs typically operate in the 1.2–4.9 THz range [142]. However, at lower frequencies within this window, they often face significant challenges such as reduced gain and higher losses due to increased free carrier absorption and material limitations. These challenges necessitate cryogenic cooling to achieve efficient operation, which restricts their practicality in many applications [143]. To cover the frequency range between 200 GHz and 1 THz, an ideal approach leverages 1550 nm MLLDs operating at THz frequencies in combination with PCAs for THz signal generation. The 1550 nm wavelength offers access to a wide range of components for modulating, controlling, and manipulating optical signals. Additionally, EDFAs can be employed to boost the signal power to hundreds of watts, if necessary, enabling high-power operation.

Achieving mode-locking at THz frequencies requires the generation of multiple longitudinal modes with equal frequency spacing and precise control of their phase relationships. To enable mode-locked DBR (ML-DBR) lasers operating at THz rates, approaches such as SBGs have been employed to generate multiple lasing channels, demonstrating stable pulse trains at frequencies of 640 GHz and 1.28 THz [92]. Additionally, super-structure gratings (SSGs) have been proposed as a viable alternative for multi-channel lasing [144]. These developments underscore the critical role of multi-channel lasing structures, such as SBGs and SSGs, in facilitating the generation of dense optical spectra. However, both SBGs and SSGs often encounter challenges, including non-uniform coupling coefficients across channels, which result in varying reflectivity and compromise the mode-locking conditions. Our work addresses these challenges by introducing MPSGs that leverage numerical optimization algorithms. Although phase-shift gratings have been widely utilized [145], [146], our approach focuses specifically on characterizing and calculating the coupling coefficients for individual channels within the MPSG. This method avoids the need to compute the entire grating spectrum during iterative optimization, thereby significantly reducing computational time per iteration. By incorporating the MPSG design, we present a practical solution for achieving optimized THz mode-locking performance with enhanced computational efficiency. We propose ML-DBR lasers and mode-locked DFB (ML-DFB) lasers based on MPSGs, with the latter integrating an equivalent π-phase shift (EPS). These devices enable multi-channel lasing, with passive mode-locking achieved by applying a biased voltage to the SA section. Sidewall grating structures in the DBR and DFB sections were fabricated using a single step of MOCVD and one step of III-V material etching. ML-DBR lasers operating at THz frequencies of 150 GHz, 400 GHz, 800 GHz, and 1.2 THz were successfully demonstrated, with pulse trains confirmed through SHG measurements using an autocorrelator. Additionally, a 200 GHz ML-DFB laser was developed. After amplification with an EDFA, the 1550 nm pulsed light was used to generate THz signals via a PCA, achieving a measured THz power of up to 19.6 μW.

6.2 Device Optimization

As previously discussed in Chapter 2, the representation of a sampled grating is expressed as Eq. (2.11). For the MPSG design, several phase-shifted points are introduced within each sampling period indicating a phase-only modulation. Consequently, the sampling function can be expressed as:

$$s(z) = \exp(j\phi(z)) \tag{6.1}$$

Fourier analysis enables the decomposition of the periodic sampling function into multiple channels, each corresponding to harmonic ghost periods. By applying a Fourier series expansion, we obtain:

$$\Delta n(z) = \frac{1}{2}\Delta n \sum_m F_m \exp(j\frac{2\pi z}{\Lambda_0})\exp\left(j\frac{2\pi m}{P}\right) + c.c \tag{6.2}$$

Where m is the integer number representing each sub-channel number and the F_m is the complex Fourier coefficient of $s(z)$ The which can be written as:

$$\begin{aligned} F_m &= \frac{1}{P}\int_P s(z)\exp(-j\frac{2\pi mz}{P})dz \\ &= \frac{1}{P}\int_P \exp\left[-j\left(\frac{2\pi mz}{P} - \phi(z)\right)\right] \end{aligned} \tag{6.3}$$

In this case, the integral is continuous. However, after introducing phase shift points, the phase shift function $\phi(z)$ becomes piecewise constant over a certain interval. The calculation can be converted into a discrete integral form for functions like $\phi(z)$, which exhibit a step-like behavior. We introduce N phase-shift points within a single sampling period, dividing it into N segments. Each phase shift occurs at the boundary between two segments, with the final phase shift of one sampling period seamlessly transitioning into the next. This approach

establishes a continuous phase-shift function across the grating, ensuring structural consistency. As a result, the transformation into a discrete Fourier series representation can be expressed as:

$$F_m = \frac{1}{N}\sum_{k=0}^{N-1}\left[\exp(j\phi[k])\exp(-j\frac{2\pi mk}{N})\right] \tag{6.4}$$

Here, the phase shift function also becomes discrete, represented as $\phi[k]$. In the reflectivity spectrum, the reflectivity of the m^{th} channel sub-grating is related to the corresponding Fourier coefficient and can be expressed as [147]:

$$R_m = \tanh^2(|\kappa_0 * F_m|L) \tag{6.5}$$

Here, κ_0 represents the coupling coefficient of the uniform seed grating, and L denotes the grating length. In this case, the reflectivity of each channel, R_m, can be efficiently determined using Eq. (6.5), eliminating the need to analyze the entire reflection spectrum. This approach significantly streamlines the optimization process, making it more compact and efficient.

To achieve the desired reflectivity spectrum, an optimal phase shift function $\phi(z)$ can be designed using numerical parameter optimization methods. By defining a trial function T, which represents the sum of the squared differences between the target reflectivity and the actual reflectivity. This T can be minimized to determine the corresponding $\phi(z)$.

$$T = \sum_{m}^{N}(R_m^{target} - R_m)^2 \tag{6.6}$$

We follow the simulated annealing algorithm for optimization [147], as this approach effectively facilitates the identification of a global optimal solution. Additionally, the reflectivity of each channel is calculated solely through Fourier series and only the peak

reflectivity of each channel is considered, eliminating the need to simulate the entire reflection spectrum using the TMM. This significantly reduces computation time, with a single optimization iteration typically completed in approximately 15 seconds using an AMD Ryzen 7 6800H CPU.

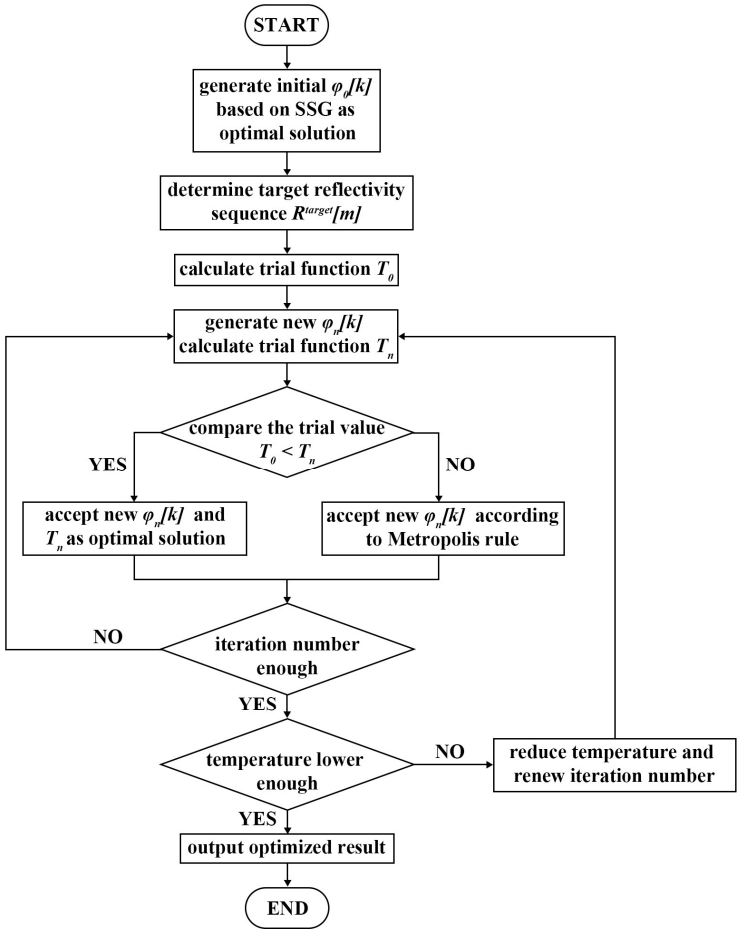

Fig. 6.1 Flowchart of the simulated annealing algorithm.

In this process shown in Fig. 6.1, a phase-shift sequence $\phi_0[k]$ within one sampling period was first generated as the initial condition. Then a target reflection spectrum is defined according to the design. Notably, here we only consider the reflectivity of each channel for the target spectrum ($R^{target}_{[m]}$) according to Eq. (6.5). The trial function (Eq. (6.6)) was first calculated for the temporal optimum value. Within the simulated annealing algorithm, the phase-shifting array $\phi[k]$ is generated randomly during each iteration, and the algorithm aims

to find the optimal array that gradually aligns the solution with the target spectrum. A cost function is implemented to prevent the solution from converging to local minima, as detailed in [147]. By controlling optimization parameters, such as the Markov chain length and annealing temperature, we can efficiently obtain the desired phase shift results while ensuring consistency with the target spectrum. Notably, the term “annealing temperature” refers to a control parameter in the algorithm that governs the acceptance probability of worse solutions during the early optimization stages, rather than any physical temperature. A higher annealing temperature increases the probability of accepting suboptimal solutions in early iterations, which helps the algorithm escape local minima and explore the solution space more broadly. As the temperature gradually decreases, the algorithm becomes more selective, refining the solution around the global minimum. This annealing schedule is crucial for balancing exploration and convergence efficiency. These optimized phase parameters are subsequently used in the design of the MPSG.

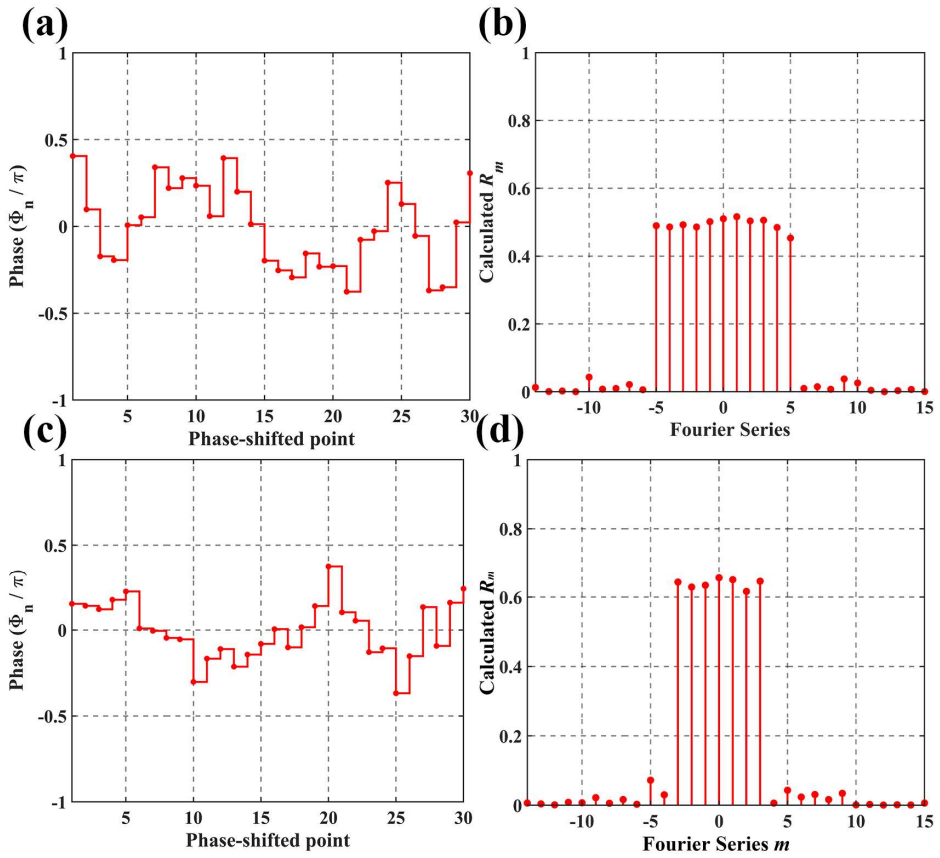

Fig. 6.2 (a) phase-shift sequence, **(b)** calculated R_m for the 11-channel MPSG, **(c)** phase-shift sequence, and **(d)** calculated R_m for the 7-channel MPSG.

Here, I present two optimized phase sequences designed for target channel counts of 11 and 7, tailored for ML-DBR and ML-DFB lasers, respectively. During each sampling period, 30 phase-shift points are applied. The optimized phase-shift sequence for the 11-channel MPSG is illustrated in Fig. 6.2(a). This optimization ensures uniform reflectivity across the lasing channels while effectively suppressing undesired modes to near-zero levels. The corresponding calculated reflectivity R_m after optimization is shown in Fig. 6.2(b), highlighting consistent reflectivity for the target channels and significant suppression of non-target channels. Similarly, the phase sequence and calculated R_m for the 7-channel MPSG are displayed in Fig. 6.2(c) and Fig. 6.2(d), respectively. As a result, this optimized phase sequence is implemented in the MPSG design. Fig. 6.3 illustrates the schematic of one sampling period of the sidewall MPSG structure, designed for both ML-DBR and ML-DFB

lasers. Phase-shift points were introduced within each sampling period (ϕ_1 to ϕ_N) and distributed evenly.

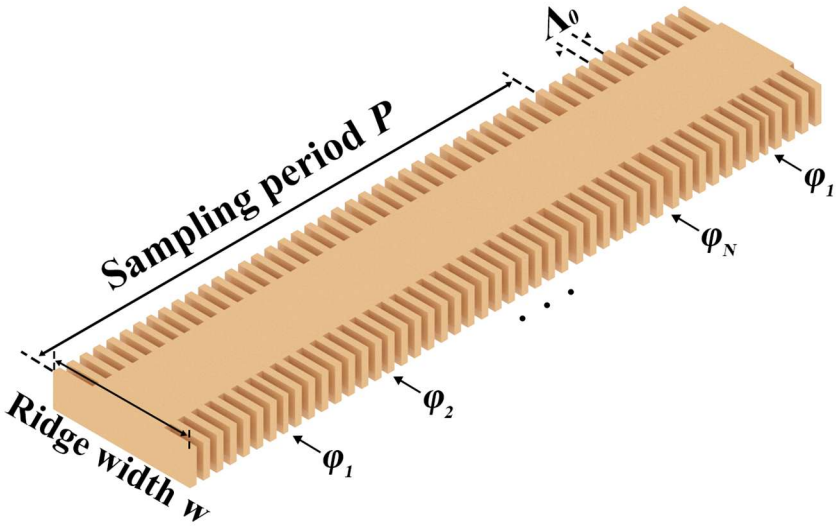

Fig. 6.3 schematic of one sampling period of MPSG structure.

The channel spacing was calculated by determining the wavelength difference between successive sub-gratings, accounting for dispersion. The center wavelength of the m^{th} sub-grating can be expressed as:

$$\lambda_m = 2n_{eff}\frac{P\Lambda_0}{m\Lambda_0 + P} \tag{6.7}$$

where n_{eff} is the effective refractive index, Λ_0 is the seed grating period, and m represents the channel number. Importantly, the channel spacing remains independent of the optimized phase-shift sequence. This decoupling allows the optimized phase information to be applied across devices with varying specifications, streamlining the design and fabrication process. Consequently, these phase parameters can be applied across a range of devices with varying sampling periods.

6.3 ML-DBR lasers based on MPSG

In ML-DBR lasers, the grating structure functions as a high-reflectivity mirror at the ends of the gain medium, providing external optical feedback. The optimized phase-shift sequence ($\phi_{optimal}$) in each sampling period is the same and is repeated along the cavity. The repetition of the sampling period enhances the reflection from the backside mirror, enabling narrow-bandwidth lasing.

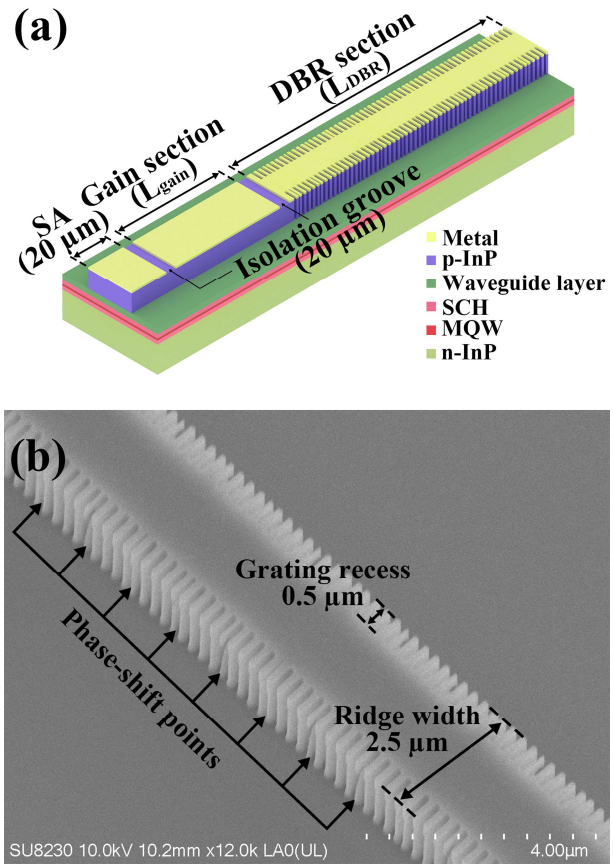

Fig. 6.4 (a) schematic of the ML-DBR laser structure, **(b)** SEM of the etched grating.

The schematic of the ML-DBR laser structure is shown in Fig. 6.4(a), with a total device length of 2.1 mm. To accommodate an integer number of sampling periods, the lengths of the grating and gain sections vary slightly among devices, as detailed in Table 6.1. The gain section is designed to be at least 560 μm to ensure adequate modal gain. The grating section

incorporates the optimized MPSG, serving as the DBR region to filter the gain spectrum into the desired channels. A 20 μm SA section with cleaving performed to an estimated accuracy of ±10 μm is included to control the phase of the lasing modes and enable passive mode-locking through a biased voltage. Electrical isolation grooves, each 20 μm wide, separate the components. Fig. 6.4(b) provides an SEM image of the etched grating. In the ML-DBR lasers, each sampling period includes 30 phase-shift points uniformly distributed at equal intervals along the grating. The design targets 11 lasing channels. Notably, all ML-DBR devices utilize the same optimized phase sequence, while each device features a unique sampling period. The seed grating features a 243 nm period with a 50% duty cycle, a grating recess depth of 0.5 μm, and a ridge waveguide width of 2.5 μm. The phase-shifted grating determines the wavelength spacing through the sampling period P, as described in Eq. (6.7), while the optimized phase-shift sequence defines the coupling coefficient for each channel.

Table 6.1 Device parameters of the ML-DBR LASER array.

Frequency spacing	**Sampling period P (μm)**	**Number of sampling periods**	**L_{gain} (μm)**	**L_{DBR} (μm)**
150 GHz	295.5	5	562.5	1477.5
400 GHz	110.5	13	603.5	1436.5
800 GHz	55.1	26	607.4	1432.6
1.2 THz	36.7	40	572.0	1468.0

For clarity, I first present the performance of the 800 GHz ML-DBR laser. The fabricated device exhibits a threshold current of 40 mA when the SA voltage (V_{SA}) is 0 V and the current in the DBR section (I_{DBR}) is 60 mA. The current injected into the DBR section compensates for ridge waveguide losses, ensuring sufficient reflection in the grating region. The output

power reaches up to 7 mW when the injection current in the gain section (I_{gain}) is increased to 300 mA.

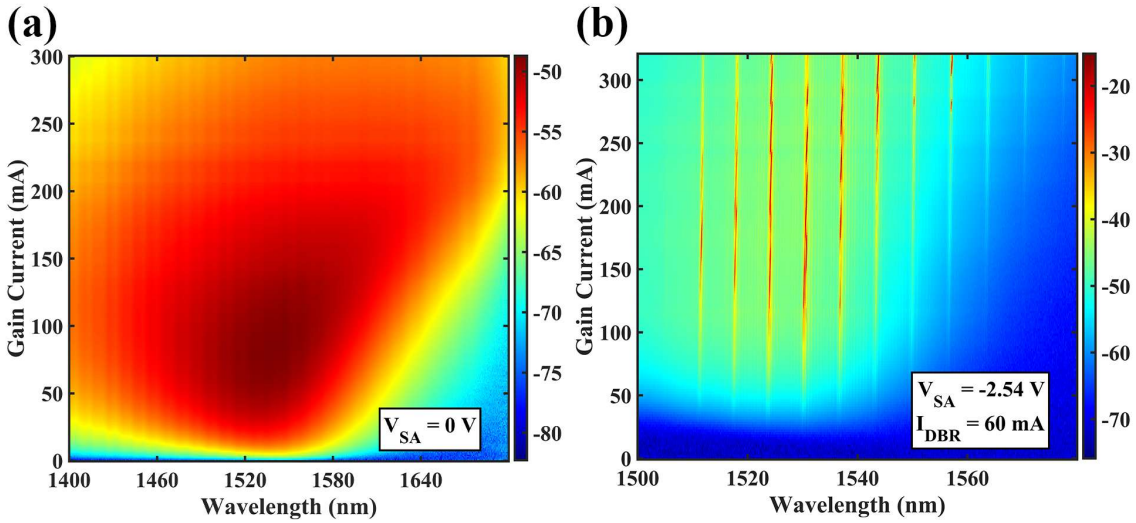

Fig. 6.5 (a) 2D emission spectrum without DBR section when V_{SA} = 0 V, **(d)** 2D spectrum versus I_{gain} of 800 GHz ML-DBR laser when V_{SA} = - 2.54 V and I_{DBR} = 60 mA.

The measured emission spectrum at different I_{gain} values are shown in Fig. 6.5(a), obtained from a device configuration with the DBR section removed, leaving only the gain and SA sections with a combined total length of 647 µm, with V_{SA} = 0 V. This spectrum reflects the amplified spontaneous emission (ASE) profile of the gain section under varying injection conditions. With the DBR section filtering the designed channels, the optical spectrum map of the 800 GHz mode-locked DBR laser is presented in Fig. 6.5(b), with V_{SA}= -2.54 V and I_{DBR}=60 mA. The optical spectrum map matches the designed channels, confirmed by 11 stopbands. However, due to FP modes formed by facet reflections, some channels may coincide with regions of reduced gain in the FP modes, resulting in lower-than-expected reflectivity for specific channels. This issue can be mitigated by applying an anti-reflection (AR) coating to the DBR facet, reducing facet reflections and improving overall performance. Furthermore, the intrinsic envelope of the active material's gain spectrum influences the effective reflectivity across channels. This can be addressed by tailoring the reflectivity of

individual channels during the optimization process, ensuring better alignment with the gain spectrum and achieving the desired performance.

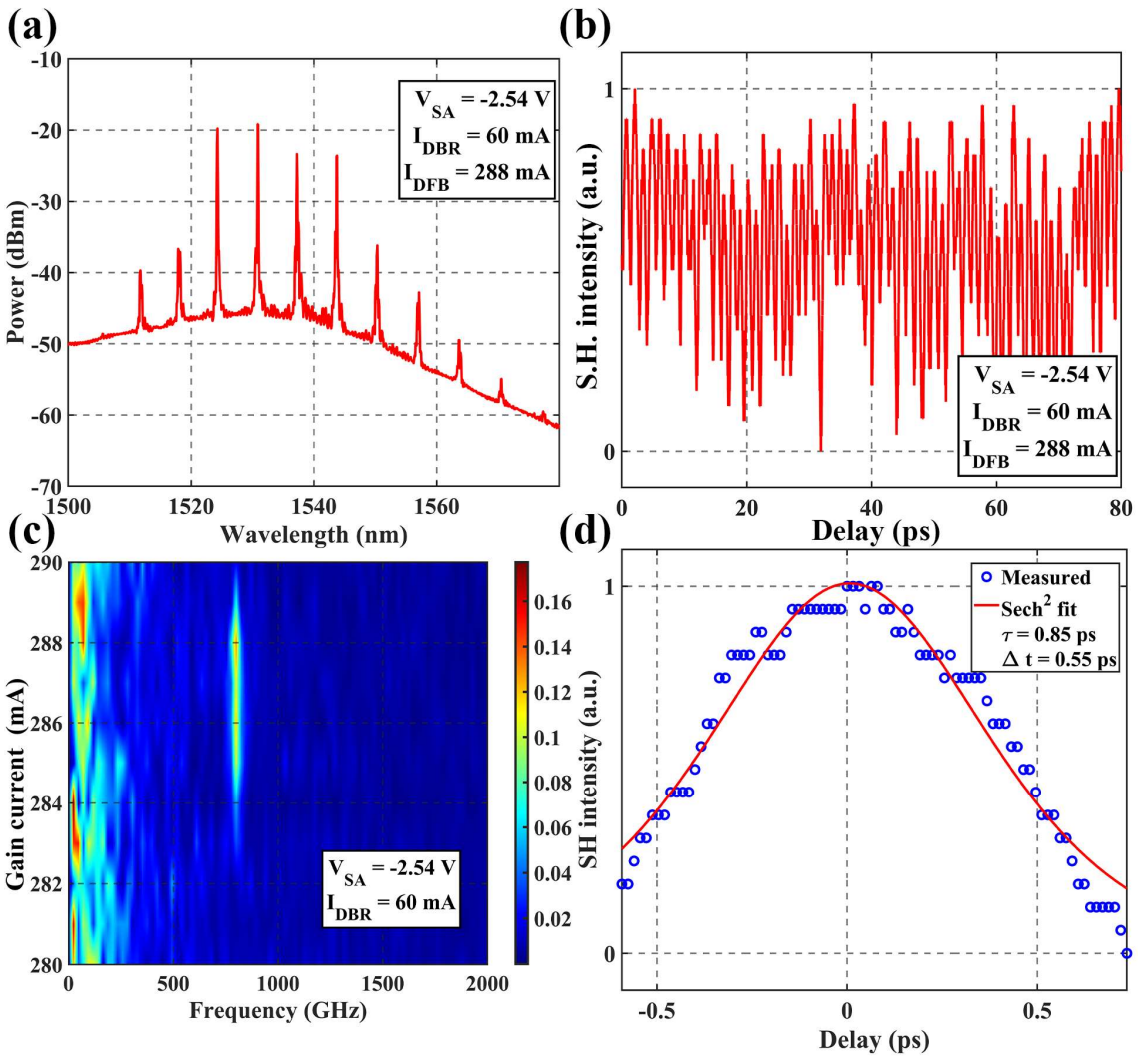

Fig. 6.6 (a) Optical spectrum and **(b)** corresponding AC trace when I_{gain} = 288 mA, I_{DBR} = 60 mA and V_{SA} = -2.54 V. **(c)** FFT map as a function of I_{gain}, **(d)** pulse shape fitted by sech^2 function.

Passive mode-locking in the ML-DBR laser was achieved by applying a bias voltage to the SA and forward injection currents to the gain and DBR sections. The optical spectrum of the 800 GHz device when I_{gain} is 288 mA, I_{DBR} is 60 mA and V_{SA} is -2.54 V is shown in Fig. 6.6(a), the intensity difference between the three main lasing modes is within 4 dB, and the adjacent channels exhibit a consistent frequency spacing of 800 GHz. The measured autocorrelation (AC)

trace is demonstrated in Fig. 6.6(b). The average pulse train period was measured to be 1.25 ps, corresponding to a fundamental mode-locking frequency of 800 GHz, which aligns with the optical spectrum shown in Fig. 6.6(a). Fast Fourier Transform (FFT) analysis of the AC traces was performed as a function of I_{gain}, ranging from 280 mA to 290 mA, to obtain the frequency spectrum of the AC traces versus I_{gain} (Fig. 6.6(c)). The device demonstrates an 800 GHz pulse repetition frequency when I_{gain} is in the range of 284 mA to 289 mA, corresponding to the observed optical spectrum. The AC trace exhibits a low-frequency modulation component of approximately 31.25 GHz. Given the group index of the device, approximately 3.48, the effective length of the grating is estimated to be around 712 μm. This suggests that the actual coupling coefficient (κ_0) is relatively low (5.73/cm), compared to the previously reported value of 20/cm in [148]. This discrepancy is likely due to fabrication imperfections, such as the RIE lag effect. This undesired 31.25 GHz modulation can be mitigated by applying an AR coating to the device's DBR facet, thereby reducing the influence of FP modes and enhancing overall performance. As shown in Fig. 6.6(d), the pulse shape was fitted using a hyperbolic sech^2 function, yielding a full width at half maximum (FWHM) of 0.85 ps in the time domain. The corresponding pulse width was calculated to be 0.55 ps. The FWHM of the optical spectrum was measured as 8.19 nm. The TBP is 0.556, which exceeds the transform-limited value for a sech^2 pulse shape (≈0.315), indicating the presence of chirp introduced by self-phase modulation (SPM) within the laser gain section [75].

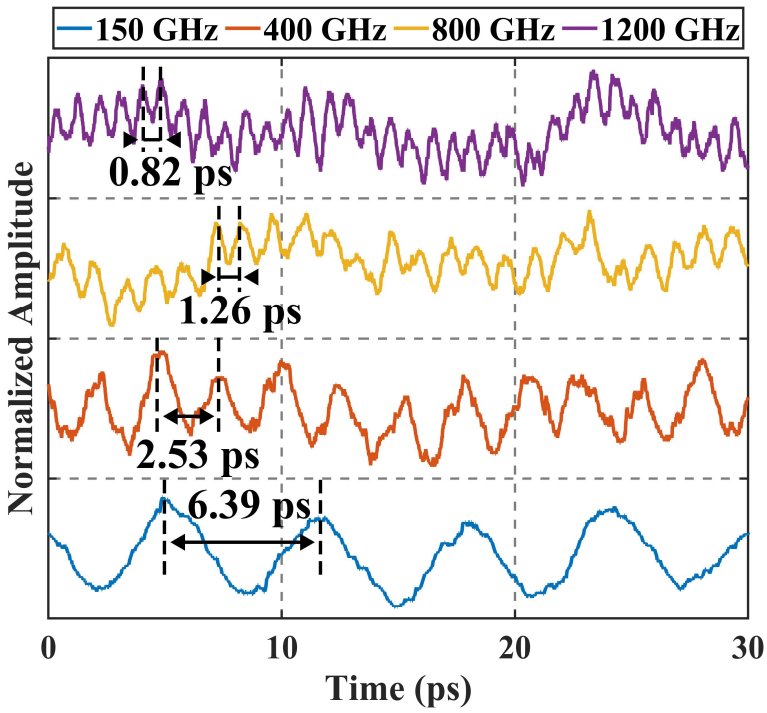

Fig. 6.7 Normalized AC traces measured for each ML-DBR laser with channel spacings of 150, 400, 800 GHz, and 1.2 THz.

Table 6.2 Measured Conditions for AC Traces of Each ML-DBR Laser.

Frequency spacing	V_{SA} **(V)**	I_{gain} **(mA)**	I_{DBR} **(mA)**
150 GHz	-2.50	230	60
400 GHz	-4.81	208	60
800 GHz	-3.31	276	60
1.2 THz	-3.45	323	60

In addition to the 800 GHz device, we measured the AC traces for devices with other designed channel spacings, including 150 GHz, 400 GHz, and 1.2 THz. Fig. 6.7 shows the measured AC traces of the four ML-DBR lasers. The reciprocal of the average autocorrelation trace period of each ML-DBR laser is consistent with its frequency

separation as designed, which indicates a stable and time-independent relationship between the lasing channels. The measurement conditions for the AC traces of the four ML-DBR lasers are listed in Table 6.2.

6.4 ML-DFB laser based on MPSG

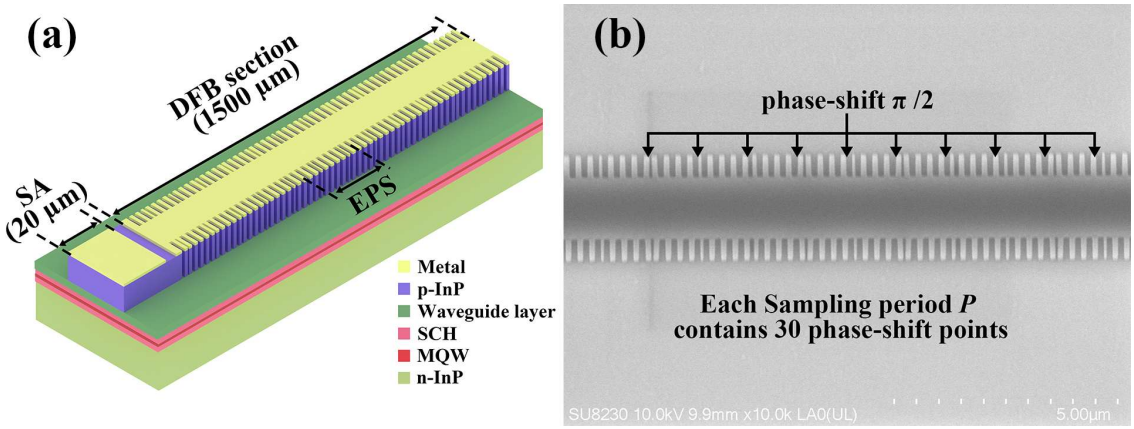

Fig. 6.8 (a) schematic of the ML-DFB laser structure, **(b)** HSQ mask of the EPS.

The ML-DFB laser consists of an SA and a DFB section as shown in Fig. 6.8(a). The 20 μm long SA section plays a crucial role in achieving mode-locking by modulating the phase relationships between longitudinal modes, thereby enabling pulse generation. The DFB section spans a length of 1500 μm and incorporates an optimized MPSG structure to ensure efficient coupling coefficient and uniform multi-channel lasing. The designed channel spacing is 200 GHz, achieved using an MPSG with a sampling period of 215 μm within the DFB section. The MPSG comprises 7 sampling periods, with each period containing 30 phase-shift points. These phase-shift points are determined by the optimized phase profile. A notable distinction in the DFB laser design is the introduction of an EPS at the center of the cavity. The EPS region has a length equal to the sampling period (215 μm) and contains 30 phase-shift points, each providing a phase shift of π/2. This configuration ensures consistency with the surrounding sampling periods while generating an exact π-phase shift. The central π-phase shift facilitates strong feedback, aligning the standing wave within the

gain region to maximize interaction and enabling lasing across all channels [149]. The HSQ mask of the EPS is shown in Fig. 6.8(b).

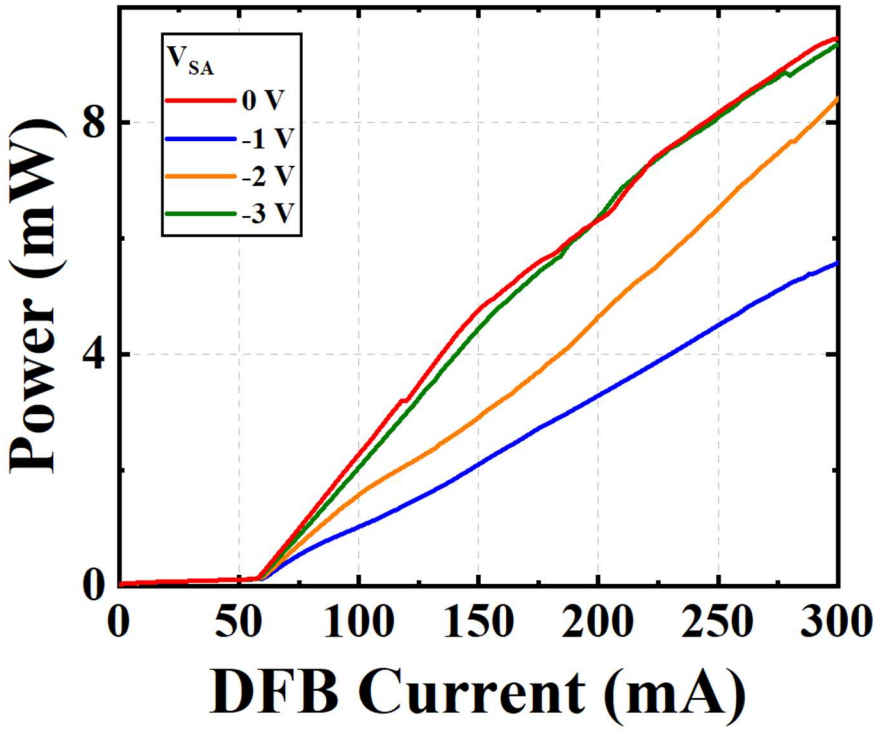

Fig. 6.9 Measured output power from the SA side of the ML-DFB laser for V_{SA} from 0 to -3 V in -1 V steps.

Fig. 6.9 illustrates the output power from the SA facet as a function of injected DFB current (I_{DFB}) under various V_{SA}. The threshold currents for all V_{SA} conditions are 58 mA, with a maximum average output power of 9.5 mW observed at V_{SA} = 0 V and I_{DFB} = 300 mA. As $|V_{SA}|$ increases, the device's output power decreases slightly due to increased absorption from interband and exciton processes. The small kinks in the power-current (*P*-*I*) curve are attributed to mode hopping, which can be mitigated by applying an AR coating to the DFB side facet.

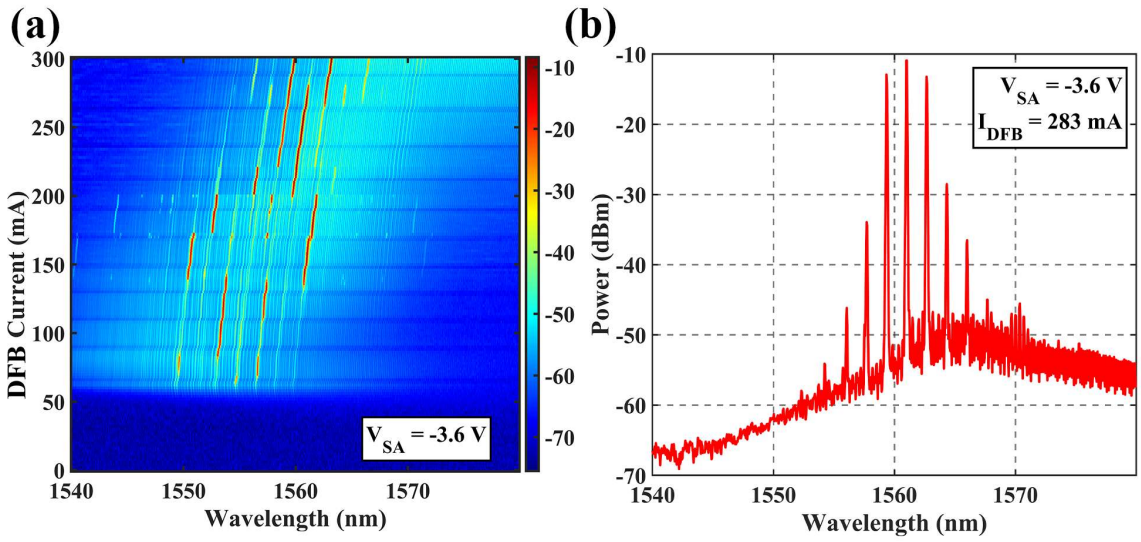

Fig. 6.10 (a) 2D optical spectrum vs I_{DFB} at V_{SA} = -3.6 V, and **(b)** the optical spectrum at I_{DFB} = 283 mA and V_{SA} = -3.6 V.

Fig. 6.10(a) presents the optical spectrum map of the 200 GHz ML-DFB laser with V_{SA}=-3.6 V. Near the threshold current of approximately 60 mA, the spectrum distinctly reveals 7 stopbands as designed in Fig. 6.2(d). As I_{DFB} increases, competitive lasing between the different channels is observed. When the current is further increased (I_{DFB} from 275 mA to 285 mA), the device exhibits stable multi-channel lasing across seven channels. The detailed optical spectrum at I_{DFB} =283 mA and V_{SA} = -3.6 V is shown in Fig. 6.10(b). The intensity difference between the three main lasing modes is within 2 dB, and the adjacent channels exhibit a consistent frequency spacing of 200 GHz. The central wavelength is 1561 nm with a 3 dB bandwidth of 6.11 nm.

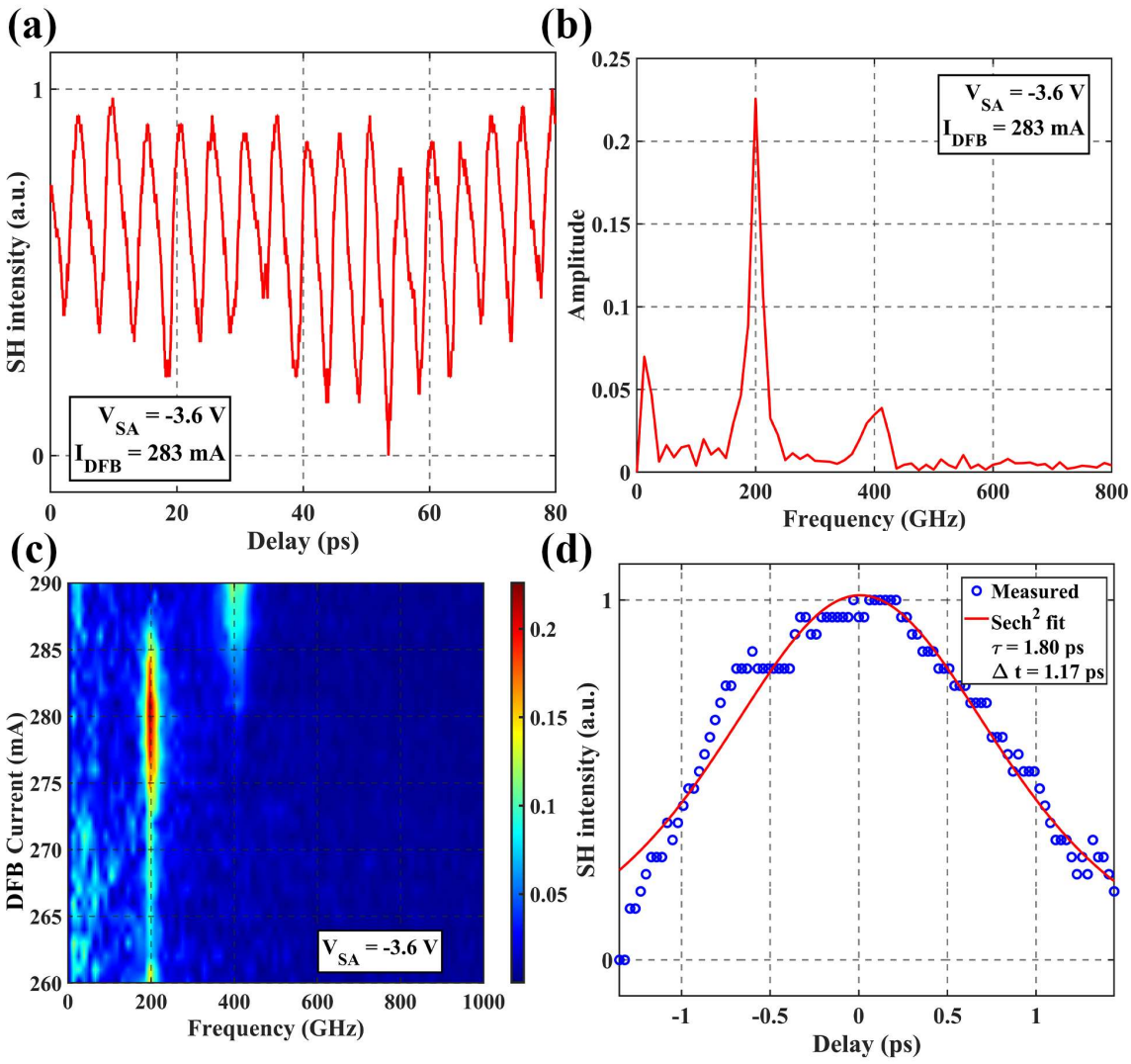

Fig. 6.11 (a) AC trace for I_{DFB} =283 mA and V_{SA} = -3.6V, **(b)** corresponding FFT transform, **(c)** FFT analysis map of the device, **(d)** pulse shape fitted by sech^2 function.

The AC trace of the 200 GHz ML-DFB laser has been recorded under varying I_{DFB} and V_{SA}. The AC trace when I_{DFB} is 283mA and V_{SA} is -3.6 V is shown in Fig. 6.11(a). By FFT analysis, we can extract the pulse repetition frequency from the AC trace which corresponds to the mode-locked frequency as displayed in Fig. 6.11(b). In addition to the fundamental mode-locked frequency at 200 GHz, a second harmonic signal at 400 GHz is also observed. This second HML phenomenon maintains self-starting capability and remains stable across a finite parameter range. Fig. 6.11 (c) shows the FFT of AC traces of the device when V_{SA} is -3.6 V and the I_{DFB} is from 260 mA to 290 mA. The device exhibits a stable 200 GHz pulse repetition frequency within a 10-mA range of I_{DFB} from 275 mA to 285 mA, corresponding

to the observed optical spectrum. As shown in Fig. 6.11(d), the pulse shape was fitted using a sech² function, and the FWHM of the pulse was found to be 1.80 ps. The pulse width was then calculated to be 1.17 ps. The TBP of the pulse is calculated to be 0.88, which is above the transform-limited value due to SPM in the DFB section.

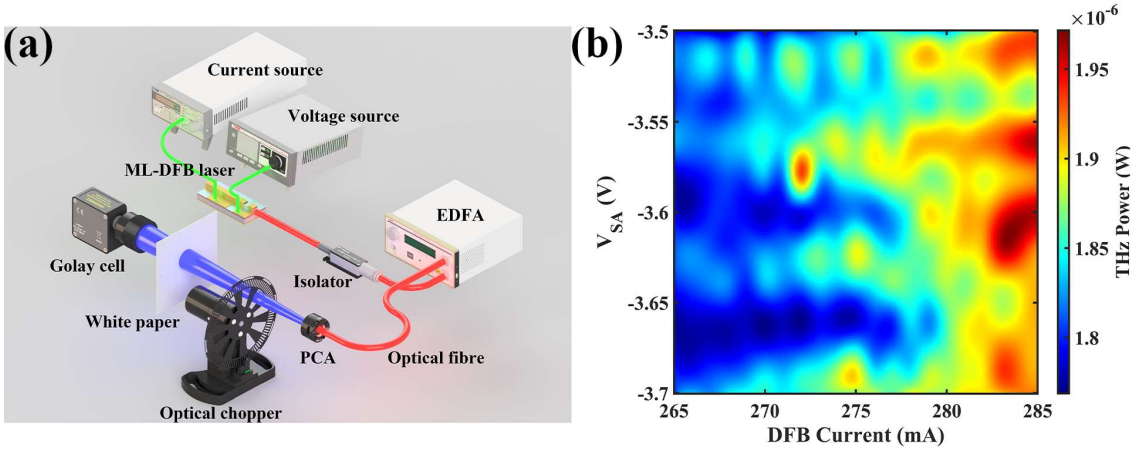

Fig. 6.12 (a) Set up for THz measurement. **(b)** Measured THz power as a function of I_{DFB} and V_{SA}.

Fig. 6.12(a) is a schematic of the experimental setup for the generation and detection of THz signals [150]. The output light from the 200 GHz ML-DFB laser was coupled into a lensed fibre and subsequently passed through an optical isolator. It was then amplified using an EDFA before being injected into the PCA to generate THz signals via the photomixing effect. The amplified output signal reached an average power of 25 mW, remaining just below the maximum power limit specified for the PCA. The PCA was operated with a bias voltage of 10 V. The generated THz waves were modulated by an optical chopper at a frequency of 20 Hz and directed into a Golay cell for signal power detection. Since the 1.55 μm light can also pass through the bowtie structure of PCA, a piece of white paper with a density of 80 g/m^2 was inserted between the optical chopper and the Golay cell to block the transmission of any 1.55 μm light [151]. The measured THz map of the working range of the device with varied I_{DFB} and V_{SA} is shown in Fig. 6.12(b). Approximately 10% of the THz signal was captured by the Golay cell, influenced by several factors: the 30° divergence angle of

radiation from the PCA, the distance (140 mm) between the PCA, the scattering of the paper and the 11 mm diameter of the entrance cone of the detector. The maximum measured THz power is 1.96 μW when I_{DFB} is 283 mA and the V_{SA} is -3.6 V. Considering these factors, the total estimated THz output power is approximately 19.6 μW. While this value is lower than the output power reported for state-of-the-art UTC-PD-based systems which is to the order of milliwatt power level [152], it is slightly higher than that of other monolithic CW sources, such as the 2PS-SBG DFB laser reaching 7.6 μW [126], indicating the potential of this approach for compact and integrable THz generation.

6.5 Chapter summary

In this chapter, I have introduced the MPSG in 1.55 μm range AlGaInAs/InP ML-DBR and ML-DFB lasers operating at THz frequencies. The sidewall grating structure offers simplicity in fabrication, requiring only a single MOCVD step and a single III-V dry etching step. The fundamental operation of ML-DBR lasers based on MPSG at 150 GHz, 400 GHz, 800 GHz, and 1.2 THz has been successfully demonstrated. Additionally, by incorporating EPS techniques, we demonstrated a 200 GHz ML-DFB laser with 7 channels, providing high-quality output suitable for THz generation via photomixing. Using an EDFA and PCA, the generated THz power reached 19.6 μW. Integrating MPSGs provides an efficient and feasible approach for achieving mode-locking and optimizing laser performance across multiple channels. Future research should prioritize optimizing the MPSGs by considering the material gain profile, as it significantly influences the effective reflectivity across channels. Tailoring the reflectivity of individual channels during the optimization process, in alignment with the gain spectrum, will help achieve better performance and further enhance the potential of these devices for advanced THz applications, including spectroscopy and communications. This work lays the foundation for the development of compact, high-power MLLDs, which are crucial for these applications.

Chapter 7 Conclusions and Future Work

7.1 Research Summary

In this thesis, three novel semiconductor laser structures based on 4PS-SBG, 4PS-SMG, and MPSG were proposed, fabricated, and experimentally demonstrated, targeting THz and MMW signal generation.

Firstly, a dual-wavelength DFB laser array incorporating 4PS-SBGs was demonstrated. This design enhances the effective coupling efficiency by a factor of approximately 2.83 compared to conventional structures and supports stable dual-mode lasing with frequency spacings from 320 GHz to 1 THz. When integrated with SOAs, the device delivers an output power of up to 27 mW. THz signal generation via photomixing in a PCA was successfully achieved, with a measured power of 12.8 μW, which supports the promise of the approach for compact and efficient THz generation.

Secondly, a dual-wavelength DFB laser based on a 4PS-SMG was introduced. By employing distinct sampling periods on each side of the ridge waveguide, the structure achieves two equivalent π-phase shifts, enabling high spectral purity and mode stability. The device maintains a power difference below 2 dB over a wide injection current range and generates an RF signal at 39.4 GHz with a linewidth of ~5.0 MHz.

Finally, mode-locked DBR and DFB lasers were developed using MPSGs. The mode-locked DBR lasers operate at repetition frequencies of 150, 400, 800 GHz, and 1.2 THz. A 200 GHz mode-locked DFB laser, amplified by an EDFA and injected into a PCA, achieved a THz output power of 19.6 μW. These results demonstrate the potential of this approach as a compact pulsed THz source.

The table highlights the performance of the devices developed in this work alongside some representative THz sources. Notably, the proposed lasers demonstrate competitive output

power. These results confirm the feasibility and effectiveness of phase-engineered gratings for compact, high-performance dual-wavelength and mode-locked laser sources in the MMW/THz domain.

Table 7.1 Summary and comparison of reported THz and MMW sources based on different architectures.

Device Type	**Frequency**	**Output Power**	**Architecture**
4PS-SBG DWL (this work)	320 GHz–1 THz	12.8 μW (PCA)	DWL + PCA
4PS-SMG DWL (this work)	39.4 GHz	—	DWL + PD
ML-DFB based on MPSG (this work)	200 GHz	19.6 μW (PCA)	ML-DFB + PCA
Tunable THz source [153]	75 GHz to 2.63 THz	Below 10 μW	DFB laser array + UTC PD
QCL-Cherenkov DFG (external cavity) [154]	1.2-5.9 THz	5 – 90 μW	QCL + intra-cavity DFG
2PS-SBG DWL [126]	560 GHz	30 nW	DWL + PCA

7.2 Future Work

Further improvements in the design, fabrication, and characterization of the proposed devices are expected to enhance performance and broaden application scope.

In terms of device design, most of the lasers demonstrated in this thesis utilize phase-modulated sampled grating structures. However, abrupt phase transitions in the grating can result in pronounced side lobes in the reflectivity spectrum, which may degrade mode selectivity. To suppress side-mode competition, future designs may incorporate apodized grating profiles to smoothen the effective refractive index variation and reduce spectral sidelobes. For ML-DBR and ML-DFB lasers based on MPSGs, although multiple lasing channels were realized, their individual intensities are still influenced by the spectral shape of the material gain. Therefore, a more refined grating design considering the gain envelope can be employed, where the reflectivity of each channel is compensated through inverse design to balance the modal gain distribution.

On the fabrication side, although the dry etching process for ridge waveguides with sidewall gratings has been optimized, issues such as undercut and the RIE lag effect still remain. Further improving the etching uniformity is expected to increase the effective coupling coefficient, potentially reaching ~80 cm^{-1}. This would enable the fabrication of shorter-cavity semiconductor lasers with lower threshold currents and higher SMSRs.

In the characterization stage, further validation of THz signal frequencies is required. Interferometric methods such as a Michelson interferometer can be employed. By analyzing the interference fringes of the emitted THz radiation, the frequency can be accurately extracted, enabling comprehensive spectral characterization across a wider frequency domain.

Bibliography

[1] S. Rangan, T. S. Rappaport, and E. Erkip, ‘Millimeter-Wave Cellular Wireless Networks: Potentials and Challenges’, *Proc. IEEE*, vol. 102, no. 3, pp. 366–385, Mar. 2014, doi: 10.1109/JPROC.2014.2299397.

[2] T. S. Rappaport, Y. Xing, G. R. MacCartney, A. F. Molisch, E. Mellios, and J. Zhang, ‘Overview of Millimeter Wave Communications for Fifth-Generation (5G) Wireless Networks—With a Focus on Propagation Models’, *IEEE Trans. Antennas Propag.*, vol. 65, no. 12, pp. 6213–6230, Dec. 2017, doi: 10.1109/TAP.2017.2734243.

[3] H.-J. Song and T. Nagatsuma, ‘Present and Future of Terahertz Communications’, *IEEE Trans. Terahertz Sci. Technol.*, vol. 1, no. 1, pp. 256–263, Sep. 2011, doi: 10.1109/TTHZ.2011.2159552.

[4] C. Lu, Y. Song, C. Li, and C. Jin, ‘Integrated Terahertz Beamforming System Based on Micromachined Silicon Interposer’, in *2023 International Topical Meeting on Microwave Photonics (MWP)*, Nanjing, China: IEEE, Oct. 2023, pp. 1–3. doi: 10.1109/MWP58203.2023.10416595.

[5] E. Restrepo, N. Wang, and D. V. Dimarogonas, ‘Simultaneous Synchronization and Topology Identification of Complex Dynamical Networks’, in *2023 62nd IEEE Conference on Decision and Control (CDC)*, Singapore, Singapore: IEEE, Dec. 2023, pp. 393–398. doi: 10.1109/CDC49753.2023.10383578.

[6] J. Yu, H. Pu, and D.-W. Sun, ‘Dual-band terahertz metamaterial sensor integrated with deep learning for synergistic identification of red wine varieties’, *Chem. Eng. J.*, vol. 520, p. 166006, Sep. 2025, doi: 10.1016/j.cej.2025.166006.

[7] C. Wang, X. Li, A. Wang, J. Bai, and Z. Guo, ‘Recent advances in terahertz biochemical sensing technology: principles, evolution and applications’, *TrAC Trends Anal. Chem.*, vol. 191, p. 118362, Oct. 2025, doi: 10.1016/j.trac.2025.118362.

[8] P. Mogensen *et al.*, ‘B4G local area: High level requirements and system design’, in *2012 IEEE Globecom Workshops*, Anaheim, CA, USA: IEEE, Dec. 2012, pp. 613–617. doi: 10.1109/GLOCOMW.2012.6477644.

[9] Z. Pi and F. Khan, ‘An introduction to millimeter-wave mobile broadband systems’, *IEEE Commun. Mag.*, vol. 49, no. 6, pp. 101–107, Jun. 2011, doi: 10.1109/MCOM.2011.5783993.

[10] T. S. Rappaport, J. N. Murdock, and F. Gutierrez, ‘State of the Art in 60-GHz Integrated Circuits and Systems for Wireless Communications’, *Proc. IEEE*, vol. 99, no. 8, pp. 1390–1436, Aug. 2011, doi: 10.1109/JPROC.2011.2143650.

[11] F. Khan and Z. Pi, ‘mmWave mobile broadband (MMB): Unleashing the 3–300GHz spectrum’, in *34th IEEE Sarnoff Symposium*, Princeton, NJ, USA: IEEE, May 2011, pp. 1–6. doi: 10.1109/SARNOF.2011.5876482.

[12] F. Gutierrez, S. Agarwal, K. Parrish, and T. S. Rappaport, ‘On-chip integrated antenna structures in CMOS for 60 GHz WPAN systems’, *IEEE J. Sel. Areas Commun.*, vol. 27, no. 8, pp. 1367–1378, Oct. 2009, doi: 10.1109/JSAC.2009.091007.

[13] C. H. Doan, S. Emami, D. A. Sobel, A. M. Niknejad, and R. W. Brodersen, 'Design considerations for 60 GHz CMOS radios', *IEEE Commun. Mag.*, vol. 42, no. 12, pp. 132–140, Dec. 2004, doi: 10.1109/MCOM.2004.1367565.

[14] C. H. Doan, S. Emami, A. M. Niknejad, and R. W. Brodersen, 'Millimeter-wave CMOS design', *IEEE J. Solid-State Circuits*, vol. 40, no. 1, pp. 144–155, Jan. 2005, doi: 10.1109/JSSC.2004.837251.

[15] M. Chakraborty, A. Banerjee, D. Kandar, and B. Maji, 'Millimeter Wave: A Novel Approach for Integrating Radar and Communication for Autonomous Driving', in *Trends in Wireless Communication and Information Security*, vol. 740, M. Chakraborty, R. Kr. Jha, V. E. Balas, S. N. Sur, and D. Kandar, Eds., in Lecture Notes in Electrical Engineering, vol. 740. , Singapore: Springer Singapore, 2021, pp. 69–79. doi: 10.1007/978-981-33-6393-9_9.

[16] X. Cai, M. Giallorenzo, and K. Sarabandi, 'Machine Learning-Based Target Classification for MMW Radar in Autonomous Driving', *IEEE Trans. Intell. Veh.*, vol. 6, no. 4, pp. 678–689, Dec. 2021, doi: 10.1109/TIV.2020.3048944.

[17] T. Zhou, M. Yang, K. Jiang, H. Wong, and D. Yang, 'MMW Radar-Based Technologies in Autonomous Driving: A Review', *Sensors*, vol. 20, no. 24, p. 7283, Dec. 2020, doi: 10.3390/s20247283.

[18] I. Hosako *et al.*, 'At the Dawn of a New Era in Terahertz Technology', *Proc. IEEE*, vol. 95, no. 8, pp. 1611–1623, Aug. 2007, doi: 10.1109/JPROC.2007.898844.

[19] P. H. Siegel, 'Terahertz technology', *IEEE Trans. Microw. Theory Tech.*, vol. 50, no. 3, pp. 910–928, Mar. 2002, doi: 10.1109/22.989974.

[20] A. Saha, 'Advances in Terahertz Imaging', in *Emerging Trends in Terahertz Solid-State Physics and Devices*, A. Biswas, A. Banerjee, A. Acharyya, H. Inokawa, and J. N. Roy, Eds., Singapore: Springer Singapore, 2020, pp. 143–168. doi: 10.1007/978-981-15-3235-1_10.

[21] P. H. Siegel, 'Terahertz Technology in Biology and Medicine', *IEEE Trans. Microw. Theory Tech.*, vol. 52, no. 10, pp. 2438–2447, Oct. 2004, doi: 10.1109/TMTT.2004.835916.

[22] D. M. Mittleman, R. H. Jacobsen, and M. C. Nuss, 'T-ray imaging', *IEEE J. Sel. Top. Quantum Electron.*, vol. 2, no. 3, pp. 679–692, Sep. 1996, doi: 10.1109/2944.571768.

[23] M. Koch, S. Hunsche, P. Schumacher, M. C. Nuss, J. Feldmann, and J. Fromm, 'THz-imaging: a new method for density mapping of wood', *Wood Sci. Technol.*, vol. 32, no. 6, pp. 421–427, Dec. 1998, doi: 10.1007/BF00702799.

[24] Z. D. Taylor *et al.*, 'THz and mm-Wave Sensing of Corneal Tissue Water Content: In Vivo Sensing and Imaging Results', *IEEE Trans. Terahertz Sci. Technol.*, vol. 5, no. 2, pp. 184–196, Mar. 2015, doi: 10.1109/TTHZ.2015.2392628.

[25] M. C. Beard, G. M. Turner, and C. A. Schmuttenmaer, 'Progress towards two-dimensional biomedical imaging with THz spectroscopy', *Phys. Med. Biol.*, vol. 47, no. 21, pp. 3841–3846, Nov. 2002, doi: 10.1088/0031-9155/47/21/323.

[26] X. Yang *et al.*, 'Biomedical Applications of Terahertz Spectroscopy and Imaging', *Trends Biotechnol.*, vol. 34, no. 10, pp. 810–824, Oct. 2016, doi:

10.1016/j.tibtech.2016.04.008.

[27] B. B. Hu and M. C. Nuss, 'Imaging with terahertz waves', *Opt. Lett.*, vol. 20, no. 16, p. 1716, Aug. 1995, doi: 10.1364/OL.20.001716.

[28] W. L. Chan, J. Deibel, and D. M. Mittleman, 'Imaging with terahertz radiation', *Rep. Prog. Phys.*, vol. 70, no. 8, pp. 1325–1379, Aug. 2007, doi: 10.1088/0034-4885/70/8/R02.

[29] P. H. Siegel, 'THz Instruments for Space', *IEEE Trans. Antennas Propag.*, vol. 55, no. 11, pp. 2957–2965, Nov. 2007, doi: 10.1109/TAP.2007.908557.

[30] Y. Doi *et al.*, 'Large-format and compact stressed Ge:Ga array for the ASTRO-F (IRIS) mission', *Adv. Space Res.*, vol. 30, no. 9, pp. 2099–2104, Nov. 2002, doi: 10.1016/S0273-1177(02)00594-X.

[31] D. T. Leisawitz *et al.*, 'Scientific motivation and technology requirements for the SPIRIT and SPECS far-infrared/submillimeter space interferometers', presented at the Astronomical Telescopes and Instrumentation, J. B. Breckinridge and P. Jakobsen, Eds., Munich, Germany, Jul. 2000, pp. 36–46. doi: 10.1117/12.393957.

[32] T. Kleine-Ostmann and T. Nagatsuma, 'A Review on Terahertz Communications Research', *J. Infrared Millim. Terahertz Waves*, vol. 32, no. 2, pp. 143–171, Feb. 2011, doi: 10.1007/s10762-010-9758-1.

[33] J. Federici and L. Moeller, 'Review of terahertz and subterahertz wireless communications', *J. Appl. Phys.*, vol. 107, no. 11, p. 111101, Jun. 2010, doi: 10.1063/1.3386413.

[34] R. Piesiewicz *et al.*, 'Short-Range Ultra-Broadband Terahertz Communications: Concepts and Perspectives', *IEEE Antennas Propag. Mag.*, vol. 49, no. 6, pp. 24–39, Dec. 2007, doi: 10.1109/MAP.2007.4455844.

[35] J. Yao, 'Microwave Photonics', *J. Light. Technol.*, vol. 27, no. 3, pp. 314–335, Feb. 2009, doi: 10.1109/JLT.2008.2009551.

[36] L. Goldberg, H. F. Taylor, J. F. Weller, and D. M. Bloom, 'Microwave signal generation with injection-locked laser diodes', *Electron. Lett.*, vol. 19, no. 13, pp. 491–493, Jun. 1983, doi: 10.1049/el:19830333.

[37] L. H. Enloe and J. L. Rodda, 'Laser phase-locked loop', *Proc. IEEE*, vol. 53, no. 2, pp. 165–166, 1965, doi: 10.1109/PROC.1965.3585.

[38] S. Ristic, A. Bhardwaj, M. J. Rodwell, L. A. Coldren, and L. A. Johansson, 'An Optical Phase-Locked Loop Photonic Integrated Circuit', *J. Light. Technol.*, vol. 28, no. 4, pp. 526–538, Feb. 2010, doi: 10.1109/JLT.2009.2030341.

[39] J. Harrison and A. Mooradian, 'Linewidth and offset frequency locking of external cavity GaAlAs lasers', *IEEE J. Quantum Electron.*, vol. 25, no. 6, pp. 1152–1155, Jun. 1989, doi: 10.1109/3.29240.

[40] K. J. Williams, L. Goldberg, R. D. Esman, M. Dagenais, and J. F. Weller, '6–34 GHz offset phase-locking of Nd:YAG 1319 nm nonplanar ring lasers', *Electron. Lett.*, vol. 25, no. 18, pp. 1242–1243, Aug. 1989, doi: 10.1049/el:19890833.

[41] Xiangfei Chen, Zhichao Deng, and Jianping Yao, 'Photonic generation of microwave signal using a dual-wavelength single-longitudinal-mode fiber ring laser', *IEEE Trans.*

Microw. Theory Tech., vol. 54, no. 2, pp. 804–809, Feb. 2006, doi: 10.1109/TMTT.2005.863064.

[42] X. Chen, J. Yao, and Z. Deng, 'Ultranarrow dual-transmission-band fiber Bragg grating filter and its application in a dual-wavelength single-longitudinal-mode fiber ring laser', *Opt. Lett.*, vol. 30, no. 16, p. 2068, Aug. 2005, doi: 10.1364/OL.30.002068.

[43] P. Mukherjee and B. Gupta, 'Terahertz (THz) Frequency Sources and Antennas - A Brief Review', *Int. J. Infrared Millim. Waves*, vol. 29, no. 12, pp. 1091–1102, Dec. 2008, doi: 10.1007/s10762-008-9423-0.

[44] S. Barbieri, J. Alton, H. E. Beere, J. Fowler, E. H. Linfield, and D. A. Ritchie, '2.9 THz quantum cascade lasers operating up to 70K in continuous wave', *Appl. Phys. Lett.*, vol. 85, no. 10, pp. 1674–1676, Sep. 2004, doi: 10.1063/1.1784874.

[45] A. Tredicucci *et al.*, 'Advances in THz quantum cascade lasers: fulfilling the application potential', presented at the Integrated Optoelectronic Devices 2005, C. Mermelstein and D. P. Bour, Eds., San Jose, California, United States, Apr. 2005, p. 146. doi: 10.1117/12.597121.

[46] L. Ajili *et al.*, 'High power quantum cascade lasers operating at $\lambda \simeq 87$ and 130μm', *Appl. Phys. Lett.*, vol. 85, no. 18, pp. 3986–3988, Nov. 2004, doi: 10.1063/1.1810217.

[47] A. Barkan *et al.*, 'Linewidth and tuning characteristics of terahertz quantum cascade lasers', *Opt. Lett.*, vol. 29, no. 6, p. 575, Mar. 2004, doi: 10.1364/OL.29.000575.

[48] B. S. Williams, S. Kumar, Q. Hu, and J. L. Reno, 'Operation of terahertz quantum-cascade lasers at 164 K in pulsed mode and at 117 K in continuous-wave mode', *Opt. Express*, vol. 13, no. 9, p. 3331, 2005, doi: 10.1364/OPEX.13.003331.

[49] L. Mahler *et al.*, 'Single-mode operation of terahertz quantum cascade lasers with distributed feedback resonators', *Appl. Phys. Lett.*, vol. 84, no. 26, pp. 5446–5448, Jun. 2004, doi: 10.1063/1.1767957.

[50] R. F. Kazarinov and R. A. Suris, 'Possibility of the amplification of electromagnetic waves in a semiconductor with a superlattice', *Sov. Phys. Semi-Conduct.*, vol. 5, no. 4, p. 707, 1971.

[51] J. Faist, F. Capasso, D. L. Sivco, C. Sirtori, A. L. Hutchinson, and A. Y. Cho, 'Quantum Cascade Laser', *Science*, vol. 264, no. 5158, pp. 553–556, Apr. 1994, doi: 10.1126/science.264.5158.553.

[52] R. Köhler *et al.*, 'Terahertz semiconductor-heterostructure laser', *Nature*, vol. 417, no. 6885, pp. 156–159, May 2002, doi: 10.1038/417156a.

[53] R. Q. Yang, 'Infrared laser based on intersubband transitions in quantum wells', *Superlattices Microstruct.*, vol. 17, no. 1, pp. 77–83, Jan. 1995, doi: 10.1006/spmi.1995.1017.

[54] A. Soibel *et al.*, 'Midinfrared Interband Cascade Laser for Free Space Optical Communication', *IEEE Photonics Technol. Lett.*, vol. 22, no. 2, pp. 121–123, Jan. 2010, doi: 10.1109/LPT.2009.2036449.

[55] I. Vurgaftman *et al.*, 'Rebalancing of internally generated carriers for mid-infrared interband cascade lasers with very low power consumption', *Nat. Commun.*, vol. 2, no. 1, p. 585, Dec. 2011, doi: 10.1038/ncomms1595.

[56] R. Q. Yang, ‘Interband cascade (IC) lasers’, in *Semiconductor Lasers*, Elsevier, 2013, pp. 487–513. doi: 10.1533/9780857096401.3.487.

[57] R. Q. Yang *et al.*, ‘InAs-Based Interband Cascade Lasers’, *IEEE J. Sel. Top. Quantum Electron.*, vol. 25, no. 6, pp. 1–8, Nov. 2019, doi: 10.1109/JSTQE.2019.2916923.

[58] J. Meyer *et al.*, ‘The Interband Cascade Laser’, *Photonics*, vol. 7, no. 3, p. 75, Sep. 2020, doi: 10.3390/photonics7030075.

[59] H.-J. Song and T. Nagatsuma, Eds., *Handbook of Terahertz Technologies: Devices and Applications*, 0 ed. Jenny Stanford Publishing, 2015. doi: 10.1201/b18381.

[60] X. Li, J. Li, Y. Li, A. Ozcan, and M. Jarrahi, ‘High-throughput terahertz imaging: progress and challenges’, *Light Sci. Appl.*, vol. 12, no. 1, p. 233, Sep. 2023, doi: 10.1038/s41377-023-01278-0.

[61] A. Nahata, A. S. Weling, and T. F. Heinz, ‘A wideband coherent terahertz spectroscopy system using optical rectification and electro-optic sampling’, *Appl. Phys. Lett.*, vol. 69, no. 16, pp. 2321–2323, Oct. 1996, doi: 10.1063/1.117511.

[62] S. Verghese, K. A. McIntosh, S. Calawa, W. F. Dinatale, E. K. Duerr, and K. A. Molvar, ‘Generation and detection of coherent terahertz waves using two photomixers’, *Appl. Phys. Lett.*, vol. 73, no. 26, pp. 3824–3826, Dec. 1998, doi: 10.1063/1.122906.

[63] G. Mouret *et al.*, ‘Far-infrared cw difference-frequency generation using vertically integrated and planar low temperature grown GaAs photomixers: application to H2S rotational spectrum up to 3 THz’, *Appl. Phys. B*, vol. 79, no. 6, pp. 725–729, Oct. 2004, doi: 10.1007/s00340-004-1607-2.

[64] I. S. Gregory *et al.*, ‘Continuous-wave terahertz system with a 60 dB dynamic range’, *Appl. Phys. Lett.*, vol. 86, no. 20, p. 204104, May 2005, doi: 10.1063/1.1935032.

[65] S. Matsuura, M. Tani, and K. Sakai, ‘Generation of coherent terahertz radiation by photomixing in dipole photoconductive antennas’, *Appl. Phys. Lett.*, vol. 70, no. 5, pp. 559–561, Feb. 1997, doi: 10.1063/1.118337.

[66] B. Ferguson and X.-C. Zhang, ‘Materials for terahertz science and technology’, *Nat. Mater.*, vol. 1, no. 1, pp. 26–33, Sep. 2002, doi: 10.1038/nmat708.

[67] K. S. Giboney, J. W. Rodwell, and J. E. Bowers, ‘Traveling-wave photodetector theory’, *IEEE Trans. Microw. Theory Tech.*, vol. 45, no. 8, pp. 1310–1319, Aug. 1997, doi: 10.1109/22.618429.

[68] N. Li *et al.*, ‘High-Saturation-Current Charge-Compensated InGaAs–InP Uni-Traveling-Carrier Photodiode’, *IEEE Photonics Technol. Lett.*, vol. 16, no. 3, pp. 864–866, Mar. 2004, doi: 10.1109/LPT.2004.823773.

[69] N. Shimizu, N. Watanabe, T. Furuta, and T. Ishibashi, ‘InP-InGaAs uni-traveling-carrier photodiode with improved 3-dB bandwidth of over 150 GHz’, *IEEE Photonics Technol. Lett.*, vol. 10, no. 3, pp. 412–414, Mar. 1998, doi: 10.1109/68.661427.

[70] H. Ito, S. Kodama, Y. Muramoto, T. Furuta, T. Nagatsuma, and T. Ishibashi, ‘High-Speed and High-Output InP–InGaAs Unitraveling-Carrier Photodiodes’, *IEEE J. Sel. Top. Quantum Electron.*, vol. 10, no. 4, pp. 709–727, Jul. 2004, doi: 10.1109/JSTQE.2004.833883.

[71] H. A. Haus, ‘Mode-locking of lasers’, *IEEE J. Sel. Top. Quantum Electron.*, vol. 6, no.

6, pp. 1173–1185, Nov. 2000, doi: 10.1109/2944.902165.

[72] R. S. Tucker *et al.*, '40 GHz active mode-locking in a 1.5 μm monolithic extended-cavity laser', *Electron. Lett.*, vol. 25, no. 10, pp. 621–622, May 1989, doi: 10.1049/el:19890421.

[73] L. Hou, M. Haji, J. H. Marsh, and A. C. Bryce, '490 fs pulse generation from a passive C-band AlGaInAs/InP quantum well mode-locked laser', *Opt. Lett.*, vol. 37, no. 5, p. 773, Mar. 2012, doi: 10.1364/OL.37.000773.

[74] E. U. Rafailov, M. A. Cataluna, and W. Sibbett, 'Mode-locked quantum-dot lasers', *Nat. Photonics*, vol. 1, no. 7, pp. 395–401, Jul. 2007, doi: 10.1038/nphoton.2007.120.

[75] G. P. Agrawal and N. A. Olsson, 'Self-phase modulation and spectral broadening of optical pulses in semiconductor laser amplifiers', *IEEE J. Quantum Electron.*, vol. 25, no. 11, pp. 2297–2306, Nov. 1989, doi: 10.1109/3.42059.

[76] H. Haus, 'Theory of mode locking with a slow saturable absorber', *IEEE J. Quantum Electron.*, vol. 11, no. 9, pp. 736–746, Sep. 1975, doi: 10.1109/JQE.1975.1068922.

[77] Y. Silberberg, D. A. B. Miller, A. C. Gossard, W. Wiegmann, P. W. Smith, and D. J. Eilenberger, 'Passive mode locking of a semiconductor diode laser', *Opt. Lett.*, vol. 9, no. 11, p. 507, Nov. 1984, doi: 10.1364/OL.9.000507.

[78] J. Javaloyes *et al.*, 'Dynamics of semiconductor passively mode-locked lasers: Experiment and theory', in *2013 15th International Conference on Transparent Optical Networks (ICTON)*, Cartagena, Spain: IEEE, Jun. 2013, pp. 1–4. doi: 10.1109/ICTON.2013.6602707.

[79] J. Javaloyes and S. Balle, 'Detuning and Thermal Effects on the Dynamics of Passively Mode-Locked Quantum-Well Lasers', *IEEE J. Quantum Electron.*, vol. 48, no. 12, pp. 1519–1526, Dec. 2012, doi: 10.1109/JQE.2012.2221684.

[80] A. A. Lagatsky, C. G. Leburn, C. T. A. Brown, W. Sibbett, S. A. Zolotovskaya, and E. U. Rafailov, 'Ultrashort-pulse lasers passively mode locked by quantum-dot-based saturable absorbers', *Prog. Quantum Electron.*, vol. 34, no. 1, pp. 1–45, Jan. 2010, doi: 10.1016/j.pquantelec.2009.11.001.

[81] A. J. Seeds, H. Shams, M. J. Fice, and C. C. Renaud, 'TeraHertz Photonics for Wireless Communications', *J. Light. Technol.*, vol. 33, no. 3, pp. 579–587, Feb. 2015, doi: 10.1109/JLT.2014.2355137.

[82] T. Shimizu, I. Ogura, and H. Yokoyama, '860 GHz rate asymmetric colliding pulse modelocked diode lasers', *Electron. Lett.*, vol. 33, no. 22, pp. 1868–1869, Oct. 1997, doi: 10.1049/el:19971266.

[83] Y. Katagiri and A. Takada, 'A harmonic colliding-pulse mode-locked semiconductor laser for stable subterahertz pulse generation', *IEEE Photonics Technol. Lett.*, vol. 9, no. 11, pp. 1442–1444, Nov. 1997, doi: 10.1109/68.634702.

[84] J. F. Martins-Filho, E. A. Avrutin, C. N. Ironside, and J. S. Roberts, 'Monolithic multiple colliding pulse mode-locked quantum-well lasers, experiment and theory', *IEEE J. Sel. Top. Quantum Electron.*, vol. 1, no. 2, pp. 539–551, Jun. 1995, doi: 10.1109/2944.401240.

[85] Y. K. Chen, M. C. Wu, T. Tanbun-Ek, R. A. Logan, and M. A. Chin, 'Subpicosecond

monolithic colliding-pulse mode-locked multiple quantum well lasers', *Appl. Phys. Lett.*, vol. 58, no. 12, pp. 1253–1255, Mar. 1991, doi: 10.1063/1.104327.

[86] L. Hou, M. Haji, and J. H. Marsh, '240 GHz pedestal-free colliding-pulse mode-locked laser with a wide operation range', *Laser Phys. Lett.*, vol. 11, no. 11, p. 115804, Nov. 2014, doi: 10.1088/1612-2011/11/11/115804.

[87] R. P. Green, M. Haji, L. Hou, G. Mezosi, R. Dylewicz, and A. E. Kelly, 'Fast saturable absorption and 10 GHz wavelength conversion in Al-quaternary multiple quantum wells', *Opt. Express*, vol. 19, no. 10, p. 9737, May 2011, doi: 10.1364/OE.19.009737.

[88] D. A. Yanson, M. W. Street, S. D. McDougall, L. G. Thayne, J. H. Marsh, and E. A. Avrutin, 'Ultrafast harmonic mode-locking of monolithic compound-cavity laser diodes incorporating photonic-bandgap reflectors', *IEEE J. Quantum Electron.*, vol. 38, no. 1, pp. 1–11, Jan. 2002, doi: 10.1109/3.973313.

[89] L. Hou, E. A. Avrutin, M. Haji, R. Dylewicz, A. C. Bryce, and J. H. Marsh, '160 GHz Passively Mode-Locked AlGaInAs 1.55 μm Strained Quantum-Well Lasers With Deeply Etched Intracavity Mirrors', *IEEE J. Sel. Top. Quantum Electron.*, vol. 19, no. 4, pp. 1100409–1100409, Jul. 2013, doi: 10.1109/JSTQE.2012.2230318.

[90] L. Hou *et al.*, '160 GHz harmonic mode-locked AlGaInAs 155μm strained quantum-well compound-cavity laser', *Opt. Lett.*, vol. 35, no. 23, p. 3991, Dec. 2010, doi: 10.1364/OL.35.003991.

[91] S. Arahira, Y. Matsui, and Y. Ogawa, 'Mode-locking at very high repetition rates more than terahertz in passively mode-locked distributed-Bragg-reflector laser diodes', *IEEE J. Quantum Electron.*, vol. 32, no. 7, pp. 1211–1224, Jul. 1996, doi: 10.1109/3.517021.

[92] L. Hou, M. Haji, and J. H. Marsh, 'Mode locking at terahertz frequencies using a distributed Bragg reflector laser with a sampled grating', *Opt. Lett.*, vol. 38, no. 7, p. 1113, Apr. 2013, doi: 10.1364/OL.38.001113.

[93] L. Hou, M. Haji, and J. H. Marsh, 'Mode-locking and frequency mixing at THz pulse repetition rates in a sampled-grating DBR mode-locked laser', *Opt. Express*, vol. 22, no. 18, p. 21690, Sep. 2014, doi: 10.1364/OE.22.021690.

[94] L. Hou, S. Tang, and J. H. Marsh, 'THz repetition frequency mode-locked laser using novel sampled gratings', in *2017 Conference on Lasers and Electro-Optics Europe & European Quantum Electronics Conference (CLEO/Europe-EQEC)*, Munich, Germany: IEEE, Jun. 2017, pp. 1–1. doi: 10.1109/CLEOE-EQEC.2017.8086379.

[95] J. A. Armstrong, 'MEASUREMENT OF PICOSECOND LASER PULSE WIDTHS', *Appl. Phys. Lett.*, vol. 10, no. 1, pp. 16–18, Jan. 1967, doi: 10.1063/1.1754787.

[96] H. P. Weber, 'Method for Pulsewidth Measurement of Ultrashort Light Pulses Generated by Phase-Locked Lasers using Nonlinear Optics', *J. Appl. Phys.*, vol. 38, no. 5, pp. 2231–2234, Apr. 1967, doi: 10.1063/1.1709859.

[97] M. Maier, W. Kaiser, and J. A. Giordmaine, 'Intense Light Bursts in the Stimulated Raman Effect', *Phys. Rev. Lett.*, vol. 17, no. 26, pp. 1275–1277, Dec. 1966, doi: 10.1103/PhysRevLett.17.1275.

[98] H. Kogelnik and C. V. Shank, 'Coupled-Wave Theory of Distributed Feedback Lasers', *J. Appl. Phys.*, vol. 43, no. 5, pp. 2327–2335, May 1972, doi: 10.1063/1.1661499.

[99] M. Yamada and K. Sakuda, ‘Analysis of almost-periodic distributed feedback slab waveguides via a fundamental matrix approach’, *Appl. Opt.*, vol. 26, no. 16, p. 3474, Aug. 1987, doi: 10.1364/AO.26.003474.

[100] J. Hong, W.-P. Huang, and T. Makino, ‘Modeling of ridge-waveguide MQW DFB lasers based on spectral index transfer matrix method’, *IEEE J. Quantum Electron.*, vol. 29, no. 6, pp. 1743–1750, Jun. 1993, doi: 10.1109/3.234430.

[101] T. Makino, ‘Transfer-matrix theory of the modulation and noise of multielement semiconductor lasers’, *IEEE J. Quantum Electron.*, vol. 29, no. 11, pp. 2762–2770, Nov. 1993, doi: 10.1109/3.248934.

[102] Jingsi Li *et al.*, ‘A Multiexposure Technology for Sampled Bragg Gratings and its Applications in Dual-Wavelength Lasing Generation and OCDMA En/Decoding’, *IEEE Photonics Technol. Lett.*, vol. 21, no. 21, pp. 1639–1641, Nov. 2009, doi: 10.1109/LPT.2009.2030877.

[103] J. Minch, S. H. Park, T. Keating, and S. L. Chuang, ‘Theory and experiment of In/sub 1-x/Ga/sub x/As/sub y/P/sub 1-y/ and In/sub 1-x-y/Ga/sub x/Al/sub y/As long-wavelength strained quantum-well lasers’, *IEEE J. Quantum Electron.*, vol. 35, no. 5, pp. 771–782, May 1999, doi: 10.1109/3.760325.

[104] W. A. Harrison, ‘Elementary theory of heterojunctions’, in *Electronic Structure of Semiconductor Heterojunctions*, vol. 1, G. Margaritondo, Ed., in Perspectives in Condensed Matter Physics, vol. 1. , Dordrecht: Springer Netherlands, 1988, pp. 208–213. doi: 10.1007/978-94-009-3073-5_20.

[105] M. Sugawara, N. Okazaki, T. Fujii, and S. Yamazaki, ‘Conduction-band and valence-band structures in strained In 1 − x Ga x As/InP quantum wells on (001) InP substrates’, *Phys. Rev. B*, vol. 48, no. 11, pp. 8102–8118, Sep. 1993, doi: 10.1103/PhysRevB.48.8102.

[106] Chih-Sheng Chang and Shun Lien Chuang, ‘Modeling of strained quantum-well lasers with spin-orbit coupling’, *IEEE J. Sel. Top. Quantum Electron.*, vol. 1, no. 2, pp. 218–229, Jun. 1995, doi: 10.1109/2944.401200.

[107] J. M. Luttinger and W. Kohn, ‘Motion of Electrons and Holes in Perturbed Periodic Fields’, *Phys. Rev.*, vol. 97, no. 4, pp. 869–883, Feb. 1955, doi: 10.1103/PhysRev.97.869.

[108] J. J. Coleman and B. I. Miller, ‘Introduction to the special issue on strained-layer optoelectronic materials and devices’, *IEEE J. Quantum Electron.*, vol. 30, no. 2, pp. 348–349, Feb. 1994, doi: 10.1109/3.283782.

[109] C. Y.-P. Chao and S. L. Chuang, ‘Spin-orbit-coupling effects on the valence-band structure of strained semiconductor quantum wells’, *Phys. Rev. B*, vol. 46, no. 7, pp. 4110–4122, Aug. 1992, doi: 10.1103/PhysRevB.46.4110.

[110] X. Li, *Optoelectronic Devices: Design, Modeling, and Simulation*, Online-Ausg. Cambridge: Cambridge University Press, 2009. doi: 10.1017/CBO9780511581144.

[111] M. Quillec, ‘Material for future InP-based optoelectronics: InGaAsP versus InGaAlAs’, presented at the Physical Concepts of Materials for Novel Optoelectronic Device Applications, M. Razeghi, Ed., Aachen, Federal Republic of Germany, Mar. 1991, p. 34. doi: 10.1117/12.24285.

[112] M. J. Mondry, D. I. Babic, J. E. Bowers, and L. A. Coldren, 'Refractive indexes of (Al,Ga,In)As epilayers on InP for optoelectronic applications', *IEEE Photonics Technol. Lett.*, vol. 4, no. 6, pp. 627–630, Jun. 1992, doi: 10.1109/68.141990.

[113] S. Adachi, 'Refractive indices of III–V compounds: Key properties of InGaAsP relevant to device design', *J. Appl. Phys.*, vol. 53, no. 8, pp. 5863–5869, Aug. 1982, doi: 10.1063/1.331425.

[114] K. Takemasa, T. Munakata, M. Kobayashi, H. Wada, and T. Kamijoh, '1.3-μm AlGaInAs-AlGaInAs strained multiple-quantum-well lasers with a p-AlInAs electron stopper layer', *IEEE Photonics Technol. Lett.*, vol. 10, no. 4, pp. 495–497, Apr. 1998, doi: 10.1109/68.662572.

[115] 'Raith EBPG 5200'. [Online]. Available: https://wiki.jwnc.gla.ac.uk/ebpg

[116] 'White paper on spinning bi-layers'. [Online]. Available: http://wiki.jwnc.gla.ac.uk/processes/pmma

[117] 'Cold development in MIBK:IPA'. [Online]. Available: http://wiki.jwnc.gla.ac.uk/processes/pmma

[118] P. Collot, T. Diallo, and J. Canteloup, 'Dry-etch monitoring of III–V heterostructures using laser reflectometry and optical emission spectroscopy', *J. Vac. Sci. Technol. B Microelectron. Nanometer Struct. Process. Meas. Phenom.*, vol. 9, no. 5, pp. 2497–2502, Sep. 1991, doi: 10.1116/1.585681.

[119] M. G. Wood, L. Chen, J. R. Burr, and R. M. Reano, 'Optimization of electron beam patterned hydrogen silsesquioxane mask edge roughness for low-loss silicon waveguides', *J. Nanophotonics*, vol. 8, no. 1, p. 083098, Jan. 2014, doi: 10.1117/1.JNP.8.083098.

[120] 'Dose tests'. [Online]. Available: https://wiki.jwnc.gla.ac.uk/doku.php/ebeam:dose_tests

[121] R. Williams, *Modern GaAs processing methods*, 2. ed. in The Artech House microwave library. Boston: Artech House, 1990.

[122] C. Cremer and M. Schienle, 'RIE etching of deep Bragg grating filters in GaInAsP/InP', *Electron. Lett.*, vol. 25, no. 17, pp. 1177–1178, Aug. 1989, doi: 10.1049/el:19890789.

[123] J. Lin *et al.*, 'Smooth and vertical-sidewall InP etching using Cl2/N2 inductively coupled plasma', *J. Vac. Sci. Technol. B Microelectron. Nanometer Struct. Process. Meas. Phenom.*, vol. 22, no. 2, pp. 510–512, Mar. 2004, doi: 10.1116/1.1648066.

[124] 'PECVD'. [Online]. Available: Available: http://wiki.jwnc.gla.ac.uk/pecvd_80_sio2

[125] J. Hong, W.-P. Huang, and T. Makino, 'Static and dynamic simulation for ridge-waveguide MQW DFB lasers', *IEEE J. Quantum Electron.*, vol. 31, no. 1, pp. 49–59, Jan. 1995, doi: 10.1109/3.341707.

[126] S. Tang, 'InP-based semiconductor lasers with novel sampled Bragg gratings and applications', 2019, doi: 10.5525/GLA.THESIS.72468.

[127] J. B. Baxter and G. W. Guglietta, 'Terahertz Spectroscopy', *Anal. Chem.*, vol. 83, no. 12, pp. 4342–4368, Jun. 2011, doi: 10.1021/ac200907z.

[128] J. Wang, J. Liu, and N. Kato, 'Networking and Communications in Autonomous Driving: A Survey', *IEEE Commun. Surv. Tutor.*, vol. 21, no. 2, pp. 1243–1274, 2019, doi: 10.1109/COMST.2018.2888904.

[129] M. J. Fice *et al.*, '146-GHz millimeter-wave radio-over-fiber photonic wireless transmission system', *Opt. Express*, vol. 20, no. 2, p. 1769, Jan. 2012, doi: 10.1364/OE.20.001769.

[130] T. R. Clark, T. P. McKenna, and J. A. Nanzer, 'Photonic millimeter wave system for high capacity wireless communications', in *2015 IEEE MTT-S International Microwave Symposium*, Phoenix, AZ, USA: IEEE, May 2015, pp. 1–4. doi: 10.1109/MWSYM.2015.7166991.

[131] B. Razavi, 'Design of Millimeter-Wave CMOS Radios: A Tutorial', *IEEE Trans. Circuits Syst. Regul. Pap.*, vol. 56, no. 1, pp. 4–16, Jan. 2009, doi: 10.1109/TCSI.2008.931648.

[132] B. Lin *et al.*, 'Inverse-Gaussian apodized fiber Bragg grating for microwave generation', in *2010 Photonics Global Conference*, Orchard, Singapore: IEEE, 2010, pp. 1–3. doi: 10.1109/PGC.2010.5705930.

[133] B. Yuan *et al.*, 'A Dual-Wavelength DFB Laser Based on Reconstruction-Equivalent-Chirp Technology for Millimeter-Wave Generation', in *2020 International Conference on UK-China Emerging Technologies (UCET)*, Glasgow, United Kingdom: IEEE, Aug. 2020, pp. 1–3. doi: 10.1109/UCET51115.2020.9205324.

[134] D. C. J. Reid, C. M. Ragdale, I. Bennion, D. J. Robbins, J. Buus, and W. J. Stewart, 'Phase-shifted moiré grating fibre resonators', *Electron. Lett.*, vol. 26, no. 1, pp. 10–12, Jan. 1990, doi: 10.1049/el:19900007.

[135] M. Chen *et al.*, 'Study on DFB Semiconductor Laser Based on Sampled Moiré Grating Integrated With Grating Reflector', *IEEE J. Quantum Electron.*, vol. 56, no. 1, pp. 1–9, Feb. 2020, doi: 10.1109/JQE.2019.2953695.

[136] S. Liu, Y. Ma, M. Chen, Y. Zhao, Y. Shi, and X. Chen, 'Study on the high-power DFB semiconductor laser based on sampled moiré grating', in *2020 International Conference on UK-China Emerging Technologies (UCET)*, Glasgow, UK: IEEE, Aug. 2020, pp. 1–4. doi: 10.1109/UCET51115.2020.9205359.

[137] W. Qi *et al.*, 'Dual Wavelength Laser Designed for Locking to Cs-133 Atomic Transitions', in *2021 Conference on Lasers and Electro-Optics Europe & European Quantum Electronics Conference (CLEO/Europe-EQEC)*, Munich, Germany: IEEE, Jun. 2021, pp. 1–1. doi: 10.1109/CLEO/Europe-EQEC52157.2021.9541624.

[138] S. Liu *et al.*, 'Planar waveguide moiré grating', *Opt. Express*, vol. 25, no. 21, p. 24960, Oct. 2017, doi: 10.1364/OE.25.024960.

[139] L. A. Coldren, S. W. Corzine, and M. L. Mašanović, *Diode Lasers and Photonic Integrated Circuits*, 1st ed. Wiley, 2012. doi: 10.1002/9781118148167.

[140] Lianping Hou *et al.*, 'Subpicosecond Pulse Generation at Quasi-40-GHz Using a Passively Mode-Locked AlGaInAs–InP 1.55-$\mu{\hbox {m}}$ Strained Quantum-Well Laser', *IEEE Photonics Technol. Lett.*, vol. 21, no. 23, pp. 1731–1733, Dec. 2009, doi: 10.1109/LPT.2009.2031088.

[141] A. Krotkus, ‘Semiconductors for terahertz photonics applications’, *J. Phys. Appl. Phys.*, vol. 43, no. 27, p. 273001, Jul. 2010, doi: 10.1088/0022-3727/43/27/273001.

[142] B. S. Williams, ‘Terahertz quantum-cascade lasers’, *Nat. Photonics*, vol. 1, no. 9, pp. 517–525, Sep. 2007, doi: 10.1038/nphoton.2007.166.

[143] M. S. Vitiello, G. Scalari, B. Williams, and P. De Natale, ‘Quantum cascade lasers: 20 years of challenges’, *Opt. Express*, vol. 23, no. 4, p. 5167, Feb. 2015, doi: 10.1364/OE.23.005167.

[144] H. Ishii, Y. Tohmori, T. Tamamura, and Y. Yoshikuni, ‘Super-structure-grating (SSG) for broadly tunable DBR lasers’, *IEEE Photonics Technol. Lett.*, vol. 5, no. 4, pp. 393–395, Apr. 1993, doi: 10.1109/68.212675.

[145] H. Ishii, Y. Tohmori, Y. Yoshikuni, T. Tamamura, and Y. Kondo, ‘Multiple-phase shift super structure grating DBR lasers for broad wavelength tuning’, *IEEE Photonics Technol. Lett.*, vol. 5, no. 6, pp. 613–615, Jun. 1993, doi: 10.1109/68.219686.

[146] Y. Nasu and S. Yamashita, ‘Densification of sampled fiber Bragg gratings using multiple-phase-shift (MPS) technique’, *J. Light. Technol.*, vol. 23, no. 4, pp. 1808–1817, Apr. 2005, doi: 10.1109/JLT.2005.844202.

[147] I. Navruz and N. Fatma Guler, ‘Optimization of reflection spectra for phase-only sampled fiber Bragg gratings’, *Opt. Commun.*, vol. 271, no. 1, pp. 119–123, Mar. 2007, doi: 10.1016/j.optcom.2006.10.015.

[148] Y. Sun *et al.*, ‘DFB laser array based on four phase-shifted sampled Bragg gratings with precise wavelength control’, *Opt. Lett.*, vol. 47, no. 23, p. 6237, Dec. 2022, doi: 10.1364/OL.475909.

[149] Y. Dai, X. Chen, D. Jiang, S. Xie, and C. Fan, ‘Equivalent Phase Shift in a Fiber Bragg Grating Achieved by Changing the Sampling Period’, *IEEE Photonics Technol. Lett.*, vol. 16, no. 10, pp. 2284–2286, Oct. 2004, doi: 10.1109/LPT.2004.834530.

[150] H. L., H. M., and M. J. H., ‘Generating terahertz pulses using mode-locked side-wall sampled-grating distributed Bragg reflector lasers’, presented at the CLEO 2013, San Jose, CA, USA, 2013, pp. 1–2.

[151] L. Hou, S. Tang, B. Hou, and J. H. Marsh, ‘Photonic integrated circuits for terahertz source generation’, *IET Optoelectron.*, vol. 14, no. 3, pp. 136–142, Jun. 2020, doi: 10.1049/iet-opt.2019.0089.

[152] H.-J. Song, K. Ajito, Y. Muramoto, A. Wakatsuki, T. Nagatsuma, and N. Kukutsu, ‘Uni-Travelling-Carrier Photodiode Module Generating 300 GHz Power Greater Than 1 mW’, *IEEE Microw. Wirel. Compon. Lett.*, vol. 22, no. 7, pp. 363–365, Jul. 2012, doi: 10.1109/lmwc.2012.2201460.

[153] Y. Wan *et al.*, ‘Generation of tunable continuous-wave THz signals using high-power multiple wavelengths DFB diode laser array’, *Opt. Commun.*, vol. 563, p. 130594, Jul. 2024, doi: 10.1016/j.optcom.2024.130594.

[154] Y. Jiang *et al.*, ‘External cavity terahertz quantum cascade laser sources based on intra-cavity frequency mixing with 1.2–5.9 THz tuning range’, *J. Opt.*, vol. 16, no. 9, p. 094002, Sep. 2014, doi: 10.1088/2040-8978/16/9/094002.

Appendix I Fabrication Workflow for Ridge Waveguide Based DFB/DBR Lasers

Step No.	Process Name	Description / Recipe
1	Sample clean	Solvent cleaning using acetone, IPA, and RO water with 3-minute ultrasonic steps each.
2	Aligned marker definition	Resist: 1. PMMA 15% 4000rpm → 180°C bake 2 min. 2. PMMA 4% 4000rpm → 180°C bake 4 min. Development: 1:2.5 MIBK 24°C for 35s. O_2 plasma clean: 110W 2 min. Metal deposition: NiCr/Au = 33/100 nm. Lift-off: Acetone 50 ℃ water bath for 1 h.
3	Electrical isolation etch	Resist: 1. PMMA 15% 4000rpm → 180°C bake 3 min. 2. PMMA 15% 4000rpm → 180°C bake 5 min. Development: 1:2.5 MIBK 24°C for 35s O_2 plasma clean: 110W 2 min. Dry etch: Cl2/CH4/H2/Ar = 8/10/15/15 sccm, 60°C. ICP/RF power = 750/100 W, 5 mTorr. Mask clean: Acetone 50 ℃ water bath for 1 h
4	Waveguide and	Pre-clean: UV-Ozone clean 5 min.

	grating definition	Resist: HSQ 2000rpm → 90°C bake 2 min 30 s. Development: 25% TMAH 24°C, 35s. Dry etch: Cl2/CH4/H2/Ar = 15/10/15/20 sccm, 60°C, ICP/RF power = 750 W/100 W, 5 mTorr. Mask clean: 1:10 HF, 1 min, rinse with RO water for 1 min.
5	PECVD and passivation	Pre-clean: UV-Ozone clean 5 min. PECVD SiO_2 200nm. HSQ spin: 4000rpm, bake 180°C in oven for 2h. PECVD SiO_2 100nm.
6	Open Window	Resist: 1. PMMA 15% 4000rpm → 180°C bake 3 min. 2. PMMA 15% 4000rpm → 180°C oven 1 h. Development: 1:2.5 MIBK 24°C for 35s O_2 plasma clean: 110W 2 min. Dry etch: CHF_3/Ar = 25/18 sccm, 200W, 30mTorr, 20 °C, about 30 min. Mask clean: O_2 = 50 sccm, 100W, 50mTorr, 20 °C, 10 min.
7	P-Contact metal	Resist: 3. PMMA 15% 4000rpm → 180°C bake 2 min. 4. PMMA 4% 4000rpm → 180°C bake 4 min.

		Development: 1:2.5 MIBK 24°C for 35s. O_2 plasma clean: 110W 2 min. Metal deposition: Ti/Pt/Au = 33/33/240 nm. Lift-off: Acetone 50 ℃ water bath for 1 h.
8	Thinning	Mount sample to glass carrier: S1818 1000rpm, sample flip and stick to the glass carrier, 90°C oven for 1 h. Mechanical Polishing: 9 μm Al_2O_3 particle solution, followed by 3 μm Al_2O_3 solution reduce ~190 μm
9	N-Contact metal	Metal deposition: Au/Ge/Au/Ni/Au = 14/14/14/11/240 nm deposition S1818 clean: Acetone 50 ℃ water bath for 1 h.
10	Annealing	Annealing at 380℃ for 60s.
11	Cleaving and mounting	Cleaving: using diamond tip to cleave along the intended line. Mounting: adhered each bar to a Cu submount using In solder.